Tree-Sliced Entropy Partial Transport

Viet-Hoang Tran[*]
Department of Mathematics
National University of Singapore
hoang.tranviet@u.nus.edu

Thanh Tran
College of Engineering & Computer Science
VinUniversity
21thanh.tq@vinuni.edu.vn

Thanh Chu
School of Computing
National University of Singapore
thanh.chu@u.nus.edu

Tam Le[†]
Department of Advanced Data Science
Institute of Statistical Mathematics
tam@ism.ac.jp

Tan M. Nguyen[†]
Department of Mathematics
National University of Singapore
tanmn@nus.edu.sg

Abstract

Optimal Transport (OT) has emerged as a fundamental tool in machine learning for comparing probability distributions in a geometrically meaningful manner. However, a key limitation of classical OT is its requirement that the source and target distributions have equal total mass, limiting its use in real-world settings involving imbalanced data, noise, outliers, or structural inconsistencies. Partial Transport (PT) addresses this limitation by allowing only a fraction of the mass to be transported, offering greater flexibility and robustness. Nonetheless, similar to OT, PT remains computationally expensive, as it typically involves solving large-scale linear programs–especially in high-dimensional spaces. To alleviate this computational burden, several emerging works have introduced the Tree-Sliced Wasserstein (TSW) distance, which projects distributions onto tree-metric spaces where OT problems admit closed-form solutions. Building on this line of research, we propose a novel framework that extends the tree-sliced approach to the PT setting, introducing the Partial Tree-Sliced Wasserstein (PartialTSW) distance. Our method is based on the key observation that, within tree-metric space, the PT problem can be equivalently reformulated as a standard balanced OT problem between suitably modified measures. This reformulation enables efficient computation while preserving the adaptability and robustness of partial transport. Our method proves effective across challenging tasks such as outlier removal and addressing class imbalance in image-to-image translation. Our code is publicly available at https://github.com/thanhqt2002/PartialTSW.

1 Introduction

Optimal Transport (OT) [87, 61] is a framework for comparing probability distributions by lifting a ground cost defined between individual points to a metric over measures. Its ability to capture the

[*]Corresponding author
[†]Co–last author

39th Conference on Neural Information Processing Systems (NeurIPS 2025).

geometric structure of distributions leads widespread adoption across numerous domains, including machine learning [56, 11, 23, 32], data valuation [35, 38], multimodal data analysis [59, 49], statistics [50, 54, 57, 63], and computer vision [55, 70, 76, 89]. Despite its theoretical appeal, OT exhibits two major limitations in applications. First, the computational cost of OT problems for discrete measures scales as $\mathcal{O}(n^3 \log n)$ [61]. Second, the framework imposes a strict mass equality constraint, which is often violated due to noise, outliers, or unbalanced distributions [72].

Sliced Optimal Transport. To mitigate the high computational cost associated with OT, the Sliced Wasserstein (SW) distance [66, 10, 67] has been introduced as an efficient approximation. SW leverages the closed-form solution of one-dimensional OT by projecting high-dimensional probability measures onto one-dimensional subspaces, computing the OT cost in each slice, and subsequently averaging these costs. This procedure reduces the computational complexity to a sequence of sort-based operations with $\mathcal{O}(n \log n)$ complexity [61], while preserving key statistical and topological properties [52, 4, 29]. The SW framework has further inspired a wide range of generalizations, including extensions based on structured projections [39, 18, 53], as well as adaptations to manifold-valued and non-Euclidean domains such as the sphere [5, 65] and hyperbolic space [8].

Tree-Sliced Optimal Transport. One-dimensional projections, while computationally efficient, often fail to capture the intricate topological features inherent in high-dimensional data. To address this shortcoming, a growing body of work has explored richer integration domains as alternatives to linear projections in OT. These efforts span a variety of metric settings, including Euclidean spaces [1, 60, 58], tree metrics [46, 81], graph-based structures [45, 43], spherical geometries [65, 5, 83], and hyperbolic spaces [6, 48]. A seminal contribution in this direction is the tree system proposed by [81], which serves as a structurally enriched substitute for traditional lines. By leveraging established results and closed-form OT solutions on tree metric spaces [46, 34, 33], this framework introduces the Tree-Sliced Wasserstein (TSW) distance—a refined analogue of the classical SW distance. TSW retains the low computational complexity of SW while enhancing its capacity to reflect underlying data geometry. Recent advancements and extensions of the TSW framework are explored in [80, 79, 84].

Partial Transport and Unbalanced Optimal Transport. In various applied settings, it is often necessary to compare positive measures with unequal total mass—for instance, in biological applications where such measures represent cell populations of varying sizes [72]. The rigid mass conservation requirement of the classical OT can be relaxed using the Unbalanced OT (UOT) framework [73, 40, 47, 15, 22, 28], which introduces penalty terms that softly enforce mass preservation rather than enforcing it strictly. A related and widely used relaxation is Partial Transport (PT) [27, 9, 2, 68, 42, 43, 44], which allows only a fraction of the mass to be transported, thereby enabling more flexible alignment between distributions. PT improves robustness to outliers and facilitates meaningful comparisons under structural or statistical mismatches. It has also shown effectiveness in robust distributional alignment and has found applications in several domains, including deep learning theory [14, 69], cellular biology [72, 17], and domain adaptation [24, 3]. Despite its advantages, PT remains computationally intensive and is susceptible to noise in high-dimensional settings [20].

To address both the computational and mass imbalance issues, several approximate and scalable variants have been introduced, including entropic OT [16, 62] and minibatch OT [25, 24]. Recent work also has extended the sliced OT framework to the unbalanced setting [7, 22, 51, 28, 9, 2, 43], resulting in Sliced UOT variants with improved scalability and robustness.

Contributions. Motivated by the expanding TSW framework and recent advances in PT on tree metric spaces [42], this paper introduces a tree-sliced approach for computing partial transport between unbalanced measures in Euclidean spaces. The paper is organized as follows:

- In Section 2, we review the foundations of Optimal Transport and Entropy Partial Transport on metric spaces with tree metrics, as well as the Tree-Sliced Wasserstein distance for probability measures in Euclidean spaces based on tree systems. These concepts collectively form the theoretical foundation upon which the proposed framework is developed

- In Section 3, we formally introduce the Tree-Sliced Entropy Partial Transport (PartialTSW) distance for comparing probability measures with unbalanced mass in Euclidean spaces. We establish its metric properties and provide an analysis of its computational complexity.

- In Section 4, we empirically evaluate PartialTSW on challenging tasks, such as enhancing noise robustness for generative models and addressing class imbalance in image-to-image translation. The results underscore its practical effectiveness and computational efficiency. We conclude our work in Section 5.

All supplemental materials—including theoretical foundations, formal proofs, experimental settings accompanied by additional tables and figures, and a table of notation—are provided in the Appendix.

2 Building Blocks of Tree-Sliced Entropy Partial Transport

This section provides the foundations of Optimal and Entropy Partial Transport, as well as the Tree-Sliced Wasserstein distance. For the remainder of the paper, we denote the dimension by d.

2.1 Optimal and Entropy Partial Transports on Metric Spaces with Tree Metrics

Tree Metric Spaces. Let $\mathcal{T} = (V, E)$ be a tree rooted at node r, with nonnegative edge lengths $\{w_e\}_{e\in E}$. We identify $\mathcal{T}$ with the set of all nodes and points along its edges. For a metric space Ω with metric $\mathtt{d}$, $\mathtt{d}$ is called a *tree metric* [75, 46] if there exists a tree $\mathcal{T}$ such that $\Omega \subset \mathcal{T}$ and $\mathtt{d}(x, y)$ equals the length of the unique path between x and y for all $x, y \in \Omega$. $\mathcal{T}$ is called a *tree metric space*. Assume $V \subset \mathbb{R}^d$ and let $d_{\mathcal{T}}$ denote the tree metric on $\mathcal{T}$; we write $[x, y]$ for the *unique path* between $x, y \in \mathcal{T}$. Let ω be the unique Borel (length) measure on $\mathcal{T}$ satisfying $\omega([x, y]) = d_{\mathcal{T}}(x, y)$ for all $x, y \in \mathcal{T}$. For any $x \in \mathcal{T}$, the *subtree rooted at* x is defined as $\Lambda(x) = \{y \in \mathcal{T} : x \in [r, y]\}$. Figure 1 (left) provides a visual representation of tree metric spaces and their associated concepts.

Optimal Transport on Tree Metric Spaces. Let $\mathcal{P}(\mathcal{T})$ be the collection of all probability measures on $\mathcal{T}$ (i.e. total mass is equal to 1). Let $\mu, \nu \in \mathcal{P}(\mathcal{T})$, and $\mathcal{P}(\mu, \nu)$ be the set of π coupling between μ and ν. The 1-Wasserstein distance (W) [87] between μ, ν is:

$$\mathrm{W}_{p,d_{\mathcal{T}}}(\mu, \nu) = \left(\inf_{\pi\in\mathcal{P}(\mu,\nu)} \int_{\mathcal{T}\times\mathcal{T}} d_{\mathcal{T}}(x, y)^p \, d\pi(x, y) \right)^{\frac{1}{p}}. \tag{1}$$

In the case of tree metrics and $p = 1$, the distance $\mathrm{W}_{1,d_{\mathcal{T}}}(\mu, \nu)$ admits a closed-form solution [46]:

$$\mathrm{W}_{1,d_{\mathcal{T}}}(\mu, \nu) = \int_{\mathcal{T}} |\mu(\Lambda(x)) - \nu(\Lambda(x))| \, \omega(dx). \tag{2}$$

For general $p > 1$, the distance $\mathrm{W}_{p,d_{\mathcal{T}}}(\mu, \nu)$ does not admit a closed-form expression. A natural generalization of Equation (2) leads to the Sobolev Transport (ST) [45], that is

$$\begin{aligned}\mathrm{ST}_p(\mu, \nu) &= \left(\int_{\mathcal{T}} |\mu(\Lambda(x)) - \nu(\Lambda(x))|^p \, \omega(dx) \right)^{\frac{1}{p}} \\ &\neq \left(\inf_{\pi\in\mathcal{P}(\mu,\nu)} \int_{\mathcal{T}\times\mathcal{T}} d_{\mathcal{T}}(x, y)^p \, d\pi(x, y) \right)^{\frac{1}{p}} = \mathrm{W}_{p,d_{\mathcal{T}}}(\mu, \nu). \end{aligned} \tag{3}$$

Although ST_p differs from $\mathrm{W}_{p,d_{\mathcal{T}}}$, it still defines a valid metric on $\mathcal{P}(\mathcal{T})$. Due to this property, and for simplicity, we focus on the case $p = 1$, as the extension to general p is analogous.

Entropy Partial Transports on Tree Metric Spaces. Let $\mathcal{M}(\mathcal{T})$ and $\mathcal{M}(\mathcal{T} \times \mathcal{T})$ denote the space of all nonnegative Borel measures on $\mathcal{T}$ and $\mathcal{T} \times \mathcal{T}$ respectively, with finite total mass. Given $\mu, \nu \in \mathcal{M}(\mathcal{T})$, define the set of admissible partial couplings as

$$\Pi_{\leq}(\mu, \nu) = \{\gamma \in \mathcal{M}(\mathcal{T} \times \mathcal{T}) : \gamma_1 \leq \mu, \ \gamma_2 \leq \nu\}, \tag{4}$$

where γ_1 and γ_2 represent the marginals of γ on the first and second marginals, respectively. For any $\gamma \in \Pi_{\leq}(\mu, \nu)$, let f_1 and f_2 be the Radon–Nikodym derivatives of γ_1 with respect to μ and γ_2 with respect to ν, respectively. Let $w : \mathcal{T} \to [0, \infty)$ defined by $w(x) = a_1 \, d_{\mathcal{T}}(x, x_0) + a_0$ where $x_0 \in \mathcal{T}$, $a_1 \in [0, b]$, and $a_0 \in [0, \infty)$. We have w is b-Lipschitz continuous. We use the entropy function $F : [0, \infty) \to (0, \infty)$ given by $F(s) = |s - 1|$. Letting $\bar{m} = \min\{\mu(\mathcal{T}), \nu(\mathcal{T})\}$, and fixing $m \in [0, \bar{m}]$, the Entropy Partial Transports (EPT) problem is formulated as

$$\mathcal{W}_m(\mu, \nu) = \inf_{\substack{\gamma\in\Pi_{\leq}(\mu,\nu) \\ \gamma(\mathcal{T}\times\mathcal{T})=m}} \left[\mathcal{F}_1(\gamma_1 \mid \mu) + \mathcal{F}_2(\gamma_2 \mid \nu) + b \int_{\mathcal{T}\times\mathcal{T}} d_{\mathcal{T}}(x, y) \, \gamma(dx, dy) \right], \tag{5}$$

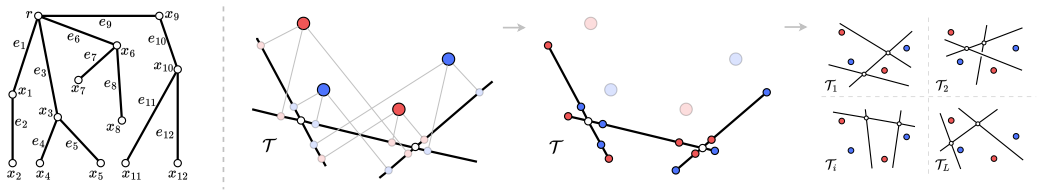

Figure 1: **An illustration of the construction of TSW.** *(Left) Tree Metric Space*. The tree is rooted at node r, with all other nodes denoted by x_i. Edges are denoted by e_i, each assigned a weight w_e. A probability distribution on the tree assigns mass to its nodes. The subtree $\Lambda(x)$ is defined as the collection of all points lying along the edges in the subtree rooted at x. For example, $\Lambda(r)$ includes the entire tree, $\Lambda(x_6)$ includes all points on edges e_7 and e_8, and $\Lambda(x_9)$ includes all points on edges e_{10}, e_{11}, and e_{12}. *(Right) An illustration of the Tree-Sliced Wasserstein computation*. Given two probability measures (depicted in red and blue), and a tree system $\mathcal{T}$, each measure is first pushed-forward onto the tree via the Radon transform, resulting in two measures supported on the tree structure. The Wasserstein distance between these tree-projected measures is then computed using Equation (2). The overall TSW distance is obtained by averaging the Wasserstein distances across a collection of such trees, typically approximated using a Monte Carlo sampling framework.

where the regularization terms are defined as the weighted relative entropies

$$\mathcal{F}_1(\gamma_1 \mid \mu) = \int_{\mathcal{T}} w(x)\, F(f_1(x))\, \mu(dx), \quad \mathcal{F}_2(\gamma_2 \mid \nu) = \int_{\mathcal{T}} w(x)\, F(f_2(x))\, \nu(dx). \tag{6}$$

To handle the mass constraint $\gamma(\mathcal{T} \times \mathcal{T}) = m$, a Lagrange multiplier $\lambda \in \mathbb{R}$ is introduced. Consider the relaxed objective

$$\mathrm{ET}_\lambda(\mu, \nu) = \inf_{\gamma \in \Pi_\leq(\mu,\nu)} \left[\mathcal{F}_1(\gamma_1 \mid \mu) + \mathcal{F}_2(\gamma_2 \mid \nu) + b \int_{\mathcal{T}\times\mathcal{T}} (d_{\mathcal{T}}(x, y) - \lambda)\, \gamma(dx, dy) \right]. \tag{7}$$

According to a construction by Caffarelli and McCann [12], the problem (7) is equivalent to a balanced OT problem. Utilizing duality and regularization techniques as in [42], the objective (7) admits a closed-form solution for the a-regularized EPT:

For $a \in [0, b\lambda/2 + w(r)]$, it is given by:

$$\begin{aligned} \widetilde{\mathrm{ET}}^a_\lambda(\mu, \nu) = \int_{\mathcal{T}} |\mu(\Lambda(x)) - \nu(\Lambda(x))|\, \omega(dx) \\ - \frac{b\lambda}{2} \left[\mu(\mathcal{T}) + \nu(\mathcal{T})\right] + \left(w(r) + \frac{b\lambda}{2} - a \right) |\mu(\mathcal{T}) - \nu(\mathcal{T})|\,. \end{aligned} \tag{8}$$

Define the corresponding regularized transport cost as

$$d_a(\mu, \nu) = \widetilde{\mathrm{ET}}^a_\lambda(\mu, \nu) + \frac{b\lambda}{2} \left[\mu(\mathcal{T}) + \nu(\mathcal{T})\right]. \tag{9}$$

The function d_a defines a *metric* on $\mathcal{M}(\mathcal{T})$, making $(\mathcal{M}(\mathcal{T}), d_a)$ a complete metric space.

2.2 Tree-Sliced Wasserstein Distance on Euclidean Spaces

We adopt the setting of Tree-Sliced Wasserstein Distance on Systems of Lines as in [81, 80]. Figure 1 (right) presents the illustration relevant to the following discussion.

Tree System. A *line* in $\mathbb{R}^d$ is an element of $\mathbb{R}^d \times \mathbb{S}^{d-1}$, and a *system of k lines* is an element of $(\mathbb{R}^d \times \mathbb{S}^{d-1})^k$. We denote a system of lines by $\mathcal{L}$, a line in $\mathcal{L}$ (also used as an index) by l, and the space of all such systems by $\mathbb{L}^d_k$. The *ground set* of $\mathcal{L}$ is defined as

$$\bar{\mathcal{L}} = \left\{ (x, l) \in \mathbb{R}^d \times \mathcal{L} :\ x = x_l + t_x \cdot \theta_l \text{ for some } t_x \in \mathbb{R} \right\},$$

where $x_l + t \cdot \theta_l$, with $t \in \mathbb{R}$, is the *parameterization of the line l*. For notational convenience, we index the lines as $l_1, \ldots, l_k$, where each line l_i is defined by a source point $x_i \in \mathbb{R}^d$ and a direction vector $\theta_i \in \mathbb{S}^{d-1}$. A *tree system* is a system of lines endowed with an additional tree structure. To

highlight the presence of this structure, we denote the system by $\mathcal{T}$ rather than $\mathcal{L}$. The *space of tree systems*—that is, the collection of tree systems sharing a common tree structure—is denoted by $\mathbb{T}_k^d$, or simply $\mathbb{T}$. This space is equipped with a probability distribution σ, which is induced by a random sampling procedure over lines.

Radon Transform on Tree Systems. For $\mathcal{T} \in \mathbb{T}_k^d$, denote the *space of Lebesgue integrable functions on* $\mathcal{T}$ as

$$L^1(\mathcal{T}) = \left\{ f \colon \bar{\mathcal{T}} \to \mathbb{R} : \ \|f\|_{\mathcal{T}} = \sum_{l \in \mathcal{T}} \int_{\mathbb{R}} |f(t_x, l)| \, dt_x < \infty \right\}.$$

Define the space $\mathcal{C}(\mathbb{R}^d \times \mathbb{T}_k^d, \Delta_{k-1})$ as the set of continuous maps from $\mathbb{R}^d \times \mathbb{T}_k^d$ to the $(k-1)$-dimensional standard simplex Δ_{k-1}, named *splitting maps*. For $f \in L^1(\mathbb{R}^d)$, we define $\mathcal{R}_{\mathcal{T}}^{\alpha} f : \bar{\mathcal{T}} \to \mathbb{R}$ such that:

$$\mathcal{R}_{\mathcal{T}}^{\alpha} f(x, l) = \int_{\mathbb{R}^d} f(y) \cdot \alpha(y, \mathcal{T})_l \cdot \delta \left(t_x - \langle y - x_l, \theta_l \rangle \right) \, dy. \tag{10}$$

The function $\mathcal{R}_{\mathcal{T}}^{\alpha} f$ is in $L^1(\mathcal{T})$. The operator

$$\mathcal{R}^{\alpha} \colon L^1(\mathbb{R}^d) \longrightarrow \prod_{\mathcal{T} \in \mathbb{T}_k^d} L^1(\mathcal{T}), \qquad f \longmapsto (\mathcal{R}_{\mathcal{T}}^{\alpha} f)_{\mathcal{T} \in \mathbb{T}_k^d}, \tag{11}$$

is called the *Radon Transform on Tree Systems*. This operator is *injective*.

Tree-Sliced Wasserstein Distance. Tran et al. [81] proposed the *Tree-Sliced Wasserstein Distance on Systems of Lines* (TSW-SL), and later Tran et al. [80] proposed the *Distance-based Tree-Sliced Wasserstein Distance* (Db-TSW) which is the generalization of the former. Throughout this paper, we refer to both variants collectively as the Tree-Sliced Wasserstein (TSW) distance for brevity. This notion is distinct from the original TSW distance proposed in [46, 42, 34, 48], which was primarily developed for applications involving static-support measures, such as classification or topological data analysis. In contrast, the TSW-SL and Db-TSW formulations—cast as OT problems over *tree systems*—are specifically designed to handle applications with dynamic-support measures, as commonly encountered in generative modeling tasks. Given $\mu, \nu \in \mathcal{P}(\mathbb{R}^d)$ and f_μ, f_ν are the probability density functions of μ, ν, respectively. The TSW distance between μ, ν is defined by

$$\text{TSW}(\mu, \nu) = \int_{\mathbb{T}} \text{W}_{d_{\mathcal{T}}, 1} \left(\mathcal{R}_{\mathcal{T}}^{\alpha} f_\mu, \mathcal{R}_{\mathcal{T}}^{\alpha} f_\nu \right) \, d\sigma(\mathcal{T}), \tag{12}$$

TSW is a metric on $\mathcal{P}(\mathbb{R}^d)$. Leveraging the closed-form solution (2) and the Monte Carlo method, TSW in Equation (12) can be efficiently approximated by a closed-form expression.

3 Tree-Sliced Entropy Partial Transport

In this section, we formally introduce the Tree-Sliced Entropy Partial Transport framework and undertake a study of its theoretical properties and associated computational complexity.

3.1 Tree-Sliced Entropy Partial Transport

Start with a density function $f \in L^1(\mathbb{R}^d)$. The Radon Transform $\mathcal{R}^{\alpha}$ maps f to a density function on a tree system while preserving its total mass, i.e.,

$$\|f\|_1 = \int_{\mathbb{R}^d} f(x) \, dx = \|\mathcal{R}_{\mathcal{T}}^{\alpha} f\|_{\mathcal{T}}, \quad \text{for all } \ \mathcal{T} \in \mathbb{T}. \tag{13}$$

A proof of this property is provided in Appendix D.6. For $\mu, \nu \in \mathcal{M}(\mathbb{R}^d)$, recall that f_μ and f_ν denote their respective density functions. Given a tree system $\mathcal{T} \in \mathbb{T}$ and a splitting map $\alpha \in \mathcal{C}(\mathbb{R}^d \times \mathbb{T}_k^d, \Delta_{k-1})$, the Radon Transform $\mathcal{R}^{\alpha}$, as defined in Equation (10), maps f_μ and f_ν to $\mathcal{R}_{\mathcal{T}}^{\alpha} f_\mu$ and $\mathcal{R}_{\mathcal{T}}^{\alpha} f_\nu$, respectively—both of which are density functions on $\mathcal{T}$. Denote the respective measures by $\mu_{\mathcal{T}}, \nu_{\mathcal{T}} \in \mathcal{M}(\mathcal{T})$. We then compute the regularized transport cost $d_a(\mu_{\mathcal{T}}, \nu_{\mathcal{T}})$ as in Equation (10). The proposed discrepancy is defined as the expectation of this quantity over the space of tree systems $\mathbb{T}$ with respect to the sampling distribution σ.

Definition 3.1 (Tree-Sliced Entropy Partial Transport)**.** The *Tree-Sliced Entropy Partial Transport*, denoted as PartialTSW, between μ and ν in $\mathcal{M}(\mathbb{R}^d)$ is defined by

$$\text{PartialTSW}(\mu,\nu) \coloneqq \int_{\mathbb{T}} d_a(\mu_{\mathcal{T}},\nu_{\mathcal{T}})d\sigma(\mathcal{T}). \tag{14}$$

Remark 3.2. It is worth noting that the value of Db-TSW is determined by a range of modeling choices, including the tree system space $\mathbb{T}$, the sampling distribution σ, the splitting map $\alpha \in \mathcal{C}(\mathbb{R}^d \times \mathbb{T}_k^d, \Delta_{k-1})$, and the regularization parameters b, λ, $w(\cdot)$, and a involved in the definition of $d_a(\cdot,\cdot)$. These dependencies are excluded from the notation for simplicity and readability.

3.2 Properties of PartialTSW

Consider the space $\mathbb{R}^d$ equipped with the Euclidean norm $\|\cdot\|_2$. For any vector $v \in \mathbb{R}^d$, the translation by v is the map $\mathbb{R}^d \to \mathbb{R}^d$ defined by $x \mapsto x + v$. The *translation group* $\mathrm{T}(d)$ consists of all such translations and is isomorphic to the additive group $\mathbb{R}^d$. The *orthogonal group* $\mathrm{O}(d)$ is the group consists of all $d \times d$ orthogonal matrices. The *Euclidean group* $\mathrm{E}(d)$ comprises all transformations of $\mathbb{R}^d$ that preserve pairwise Euclidean distances. Formally, $\mathrm{E}(d)$ is the semidirect product of $\mathrm{T}(d)$ and $\mathrm{O}(d)$. Each element $g \in \mathrm{E}(d)$ can be represented as a pair $g = (Q, v)$, where $Q \in \mathrm{O}(d)$ and $v \in \mathbb{R}^d$, and acts on $\mathbb{R}^d$ via $y \mapsto gy = Qy + v$. The canonical group action of $\mathrm{E}(d)$ on $\mathbb{R}^d$ naturally extends to the space of tree systems $\mathbb{T}_k^d$ through the rule

$$g\mathcal{T} = \{gl_i = (Qx_i + a, Q\theta_i)\}_{i=1}^k \in \mathbb{T}_k^d,$$

which preserves the underlying tree structure by construction. A splitting map $\alpha \in \mathcal{C}(\mathbb{R}^d \times \mathbb{T}_k^d, \Delta_{k-1})$ is said to be $\mathrm{E}(d)$-invariant if

$$\alpha(gx, g\mathcal{T}) = \alpha(x, \mathcal{T}), \quad \text{for all } x \in \mathbb{R}^d \text{ and } \mathcal{T} \in \mathbb{T}_k^d. \tag{15}$$

In the context of optimal transport theory, where a cost function defined on the ground space is lifted to a distance between measures, it is often desirable—particularly for measures on $\mathbb{R}^d$—that the resulting metric be equivariant under the action of the Euclidean group. Notably, both the 2-Wasserstein distance and the Sliced p-Wasserstein distance are known to exhibit $\mathrm{E}(d)$-invariance. Remarkably, in the case of PartialTSW, this invariance not only ensures that the discrepancy is $\mathrm{E}(d)$-invariant, but also guarantees that it is a valid metric on the space of measures $\mathcal{M}(\mathbb{R}^d)$.

Theorem 3.3. PartialTSW *is an* $\mathrm{E}(d)$*-invariant metric on* $\mathcal{M}(\mathbb{R}^d)$.

The proof for Theorem 3.3 is presented in Appendix §D.7.

Remark 3.4. As in [80], for the experiments in Section 4, we choose the splitting map α such that

$$\alpha(x, \mathcal{T}) = \text{softmax}\left(\left\{\inf_{t\in\mathbb{R}} \|x - (x_i + t\theta_i)\|_2\right\}_{i=1}^k\right), \quad \text{for all } x \in \mathbb{R}^d \text{ and } \mathcal{T} \in \mathbb{T}, \tag{16}$$

which is $\mathrm{E}(d)$-invariant.

3.3 Computation of Tree-Sliced Entropy Partial Transport

Similar to UOT and PT, PartialTSW compares $\mu, \nu \in \mathcal{M}(\mathbb{R}^d)$ while offering a mechanism to softly enforce the fraction of mass to be transported. This is achieved by adjusting the total masses of their respective projections onto a tree system $\mathcal{T}$, denoted $\mu(\mathcal{T})$ and $\nu(\mathcal{T})$ (as in Equation (8) and (9)). Given that the Radon Transform $\mathcal{R}_{\mathcal{T}}^{\alpha}$ is mass-preserving, modifying the masses $\mu(\mathcal{T})$ and $\nu(\mathcal{T})$ directly controls the degree of partiality in the transport between the original measures μ and ν. In practice, $\mu(\mathcal{T})$ is often normalized to a unit mass, with $\nu(\mathcal{T})$ then serving as a tunable hyperparameter to control this partiality.

A key application of PartialTSW is computing gradients of PartialTSW(μ, ν) with respect to samples from μ and ν, crucial for generative modeling and gradient flows. Here, samples typically have constant mass (e.g., $1/n$ where n is the number of supports), rendering gradients with respect to total input masses $\mu(\mathbb{R}^d)$ and $\nu(\mathbb{R}^d)$ less meaningful. This simplifies hyperparameter selection: parameters a, b and λ in Equation (9) are not necessary. The mass $\nu(\mathcal{T})$ emerges as the only parameter for controlling the degree of partiality.

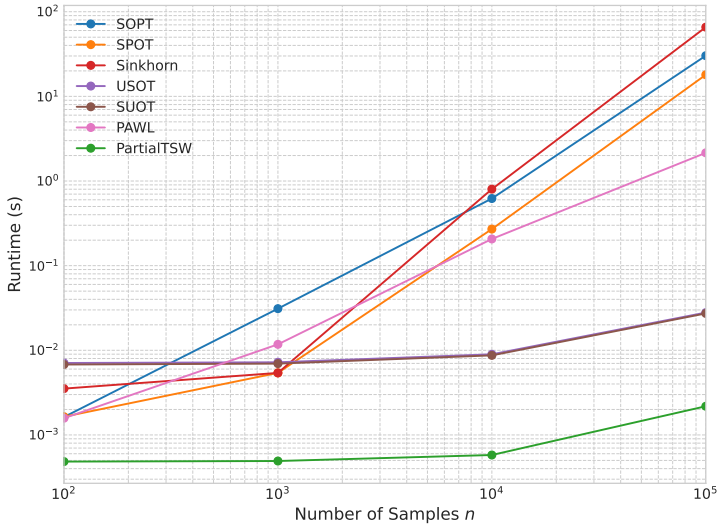

Figure 2: Runtime comparison for PartialTSW and PT/UOT solvers over n.

Computationally, the intractable integral in Equation (50) is approximated using Monte Carlo method:

$$\widehat{\text{PartialTSW}}(\mu,\nu) = \frac{1}{L}\sum_{i=1}^{L} d_a(\mu_{\mathcal{T}_i},\nu_{\mathcal{T}_i}), \tag{17}$$

where $\{\mathcal{T}_i\}_{i=1}^{L}$ are tree systems independently sampled from σ over $\mathbb{T}$. The theoretical complexity is $\mathcal{O}(Lkn\log n + Lkdn)$ (with n samples, k lines per tree, d data dimension), identical to its balanced counterpart, TSW [80]. PartialTSW adds negligible computational overhead to TSW, mainly from adjusting the masses $\nu(\mathcal{T})$. Detailed algorithms and complexity analysis are provided in Appendices §E.1 and §E.2.

The log-linear scaling of PartialTSW with respect to the number of samples n makes it significantly faster in practice than existing UOT and PT methods. Figure 2 illustrates this performance gap: for $n = 10^5$ samples, alternative approaches, such as the translation-invariant Sinkhorn [74] and PAWL [13], are approximately three orders of magnitude slower than PartialTSW. While USOT [7] and SUOT [7] exhibit similar scaling behavior due to their GPU-friendly implementations, PartialTSW maintains a speed advantage. Further details on computational efficiency are available in Appendix §E.6.

Since PartialTSW is approximated via Monte Carlo (MC) estimation, a crucial aspect is the stability and sample complexity of its estimator. Our distance is computed over L sampled trees, and its approximation error is theoretically expected to decrease at a standard $\mathcal{O}(L^{-1/2})$ rate. We provide a detailed empirical analysis in Appendix §E.4 that verifies this convergence.

4 Experimental Results

This section details the empirical evaluation of PartialTSW against other methods in tasks requiring noise robustness for point cloud alignment, outlier rejection in generative modeling, and effective handling of class imbalance in image to image translation.

4.1 Noisy Point Cloud Gradient Flow

In this experiment, we aim to evaluate the robustness of PartialTSW compared to other optimal transport (OT) variants such as SW [10] and Db-TSW [80]. The source dataset X consists of 10,000 points arranged in the shape of a dragon. The target dataset Y, also with 10,000 points, follows the shape of a bunny and is perturbed with 7% noise. Our objective is to determine whether PartialTSW can align with the target shape while ignoring noisy outliers. The clean data is taken from [2].

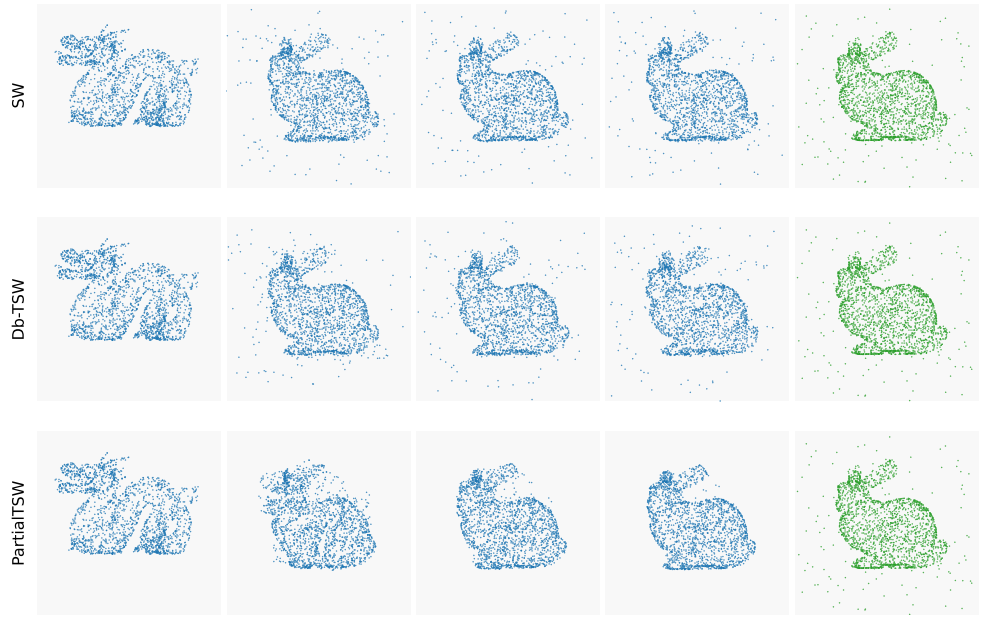

Figure 3: Visualization of point cloud gradient flows for SW, Db-TSW, and PartialTSW at steps 100, 200, and 300. The leftmost column is the source point cloud, and the rightmost column is the noise-perturbed target point cloud.

We apply gradient descent to the source points in order to minimize the distance $D(X, Y)$, where D is either PartialTSW, Db-TSW, or SW. The results are illustrated in Figure 3. It is clear that OT methods such as SW and Db-TSW are affected by noisy data. In contrast, PartialTSW demonstrates greater robustness, producing smoother interpolations. We refer to Appendix §E.7 for further details.

4.2 Robust Generative Model

To further demonstrate its outlier robustness, PartialTSW is evaluated in a generative modeling experiment. First, an Autoencoder pre-trained on MNIST digits provides 2D latent representations for digit `0` (the target class) and digit `1` (the outlier class), scaled to approximately reside within $[-1, 1]^2$. Let $\mathcal{X}_0$ and $\mathcal{X}_1$ denote the true latent distributions for digits `0` and `1`, respectively. The generator is subsequently trained using an observed dataset, X_{obs}, which is a mixture composed of 90% samples drawn from $\mathcal{X}_0$ and 10% samples (outliers) drawn from $\mathcal{X}_1$. This contaminated input data is illustrated in Figure 4a. A generator $G : \mathcal{N}(0, I_2) \to [-1, 1]^2$ is then trained by minimizing $D(G(Z), X_{\text{obs}})$, where Z is a batch of noise samples and D is the (Partial) Optimal Transport distance. The objective is for G to learn to capture the target distribution $\mathcal{X}_0$ from the contaminated X_{obs}, effectively ignoring the outliers from $\mathcal{X}_1$. Further experimental details are available in Appendix §E.8.

Figure 4 and Table 1 summarize method performances. Standard OT methods (e.g., SW [10], Db-TSW [80]; Figure 4b-c) and several UOT/PT approaches (e.g., SOPT [2], SPOT [9], SUOT [7], USOT [7]; Figure 4d-e, g-h) struggled with the 10% outliers. Despite careful hyperparameter tuning (details in Appendix §E.8.2), these methods often produced mixed `0`s and `1`s or noisy outputs.

Conversely, PartialTSW demonstrates excellent robustness, achieving a 0.00% outlier rate (Table 1) by ignoring MNIST `1` outliers and generating only high-quality `0` digits (Figure 4j). This robust performance is complemented by strong sample diversity, stemming from its notably well-distributed latent space. Sinkhorn [74] and PAWL [13] also achieve 0.00% outlier rejection (Figure 4f,i); however, they exhibit less sample diversity, as suggested by their concentrated latent clusters.

PartialTSW also provides this robust and diverse generation with high computational efficiency. Its 55s runtime matches Db-TSW and is significantly faster than Sinkhorn (358s) and PAWL (88s). While SW is the fastest overall, it lacks the necessary outlier robustness.

Table 1: Quantitative comparison for robust generative modeling on MNIST, using target digit 0 and 10% 1 outliers. PartialTSW achieves perfect outlier rejection alongside a competitive runtime.

	OT		Unbalanced OT / Partial OT						Ours
Metric	SW [10]	Db-TSW [80]	SOPT [2]	SPOT [9]	Sinkhorn [74]	SUOT [7]	USOT [7]	PAWL [13]	PartialTSW
Outliers (%) ↓	15.06	16.44	13.28	16.20	**0.00**	41.00	17.08	**0.00**	**0.00**
Runtime (s) ↓	**37**	<u>55</u>	278	278	358	275	306	88	<u>55</u>

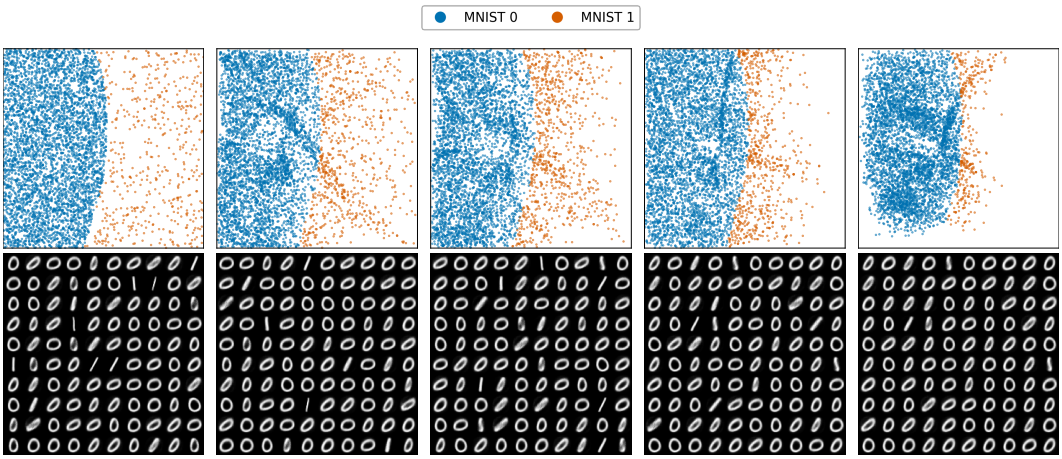

(a) Dataset (b) SW [10] (c) Db-TSW [80] (d) SOPT [2] (e) SPOT [9]

(f) Sinkhorn [74] (g) SUOT [7] (h) USOT [7] (i) PAWL [13] (j) PartialTSW

Figure 4: Qualitative comparison of outlier robustness in generative modeling. Methods learn to generate MNIST 0 (blue) from a dataset with 10% 1 outliers (orange). Subplots display generated latent distributions (top) and images (bottom). PartialTSW successfully ignores outliers and accurately learns the true latent distribution of the digit 0, leading to the diverse generated images.

Thus, PartialTSW uniquely combines strong outlier rejection, diverse sample generation, and high computational efficiency, making it highly effective for generative modeling in contaminated settings.

4.3 Imbalance Image to Image Translation

Another key attribute of PartialTSW is its ability to handle class imbalance. We demonstrate this capability in an image-to-image translation task, converting "Young" to "Adult" faces using the FFHQ dataset [37]. This dataset presents a significant imbalance, with 38K "Young" images and 10.5K "Adult" images. Our experimental setup follows the protocol from recent unbalanced optimal transport studies [22, 28]. Specifically, a pre-trained ALAE autoencoder [64] yields 512-dimensional

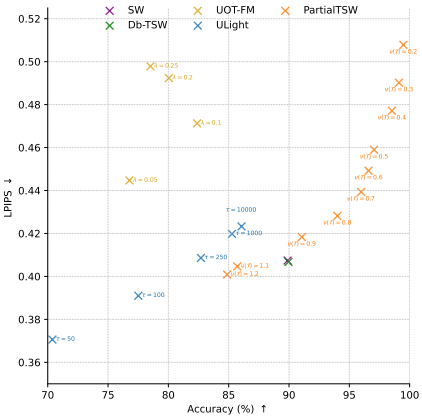

Figure 5: Visualizing the Accuracy-LPIPS trade-off in Image-to-Image translation.

Table 2: Quantitative Young-to-Adult translation results. PartialTSW (Ours) achieves a good balance of Accuracy ↑ and perceptual similarity (LPIPS ↓).

Method		Accuracy (%) ↑	LPIPS ↓
SW [10]		89.88 ± 0.01	0.4074 ± 0.0002
Db-TSW [80]		89.96 ± 0.01	0.4068 ± 0.0002
UOT-FM [22]	$\lambda = 0.05$	76.16 ± 0.08	0.4979 ± 0.0001
	$\lambda = 0.1$	82.38 ± 0.05	0.4713 ± 0.0001
	$\lambda = 0.2$	80.44 ± 0.03	0.4920 ± 0.0003
ULightOT [28]	$\tau = 50$	70.39 ± 0.09	0.3706 ± 0.0003
	$\tau = 250$	82.70 ± 0.05	0.4086 ± 0.0002
	$\tau = 1000$	85.27 ± 0.06	0.4198 ± 0.0001
	$\tau = 10000$	86.06 ± 0.04	0.4233 ± 0.0001
PartialTSW	$\nu(\mathcal{T}) = 1.1$	85.71 ± 0.03	0.4047 ± 0.0002
	$\nu(\mathcal{T}) = 0.9$	91.06 ± 0.02	0.4183 ± 0.0002
	$\nu(\mathcal{T}) = 0.5$	97.05 ± 0.03	0.4590 ± 0.0001
	$\nu(\mathcal{T}) = 0.3$	$\mathbf{99.11 \pm 0.03}$	0.4902 ± 0.0003

latent image representations, where the translation is performed. All methods are evaluated on two criteria: (1) translation accuracy (whether images reconstructed from $M(X)$ classify as "Adult") and (2) perceptual similarity (LPIPS [90]) between original and translated reconstructions.

The mapping network M is trained to translate latent samples X from the "Young" domain to align with Y from the "Adult" domain by minimizing a distance $D(M(X), Y)$, where D represents our PartialTSW, SW [10], or Db-TSW [80]. We also compare against other recent procedures for this task: UOT-FM [22] and ULightOT [28]. These methods, along with PartialTSW, feature parameters to control their degree of regularization when handling data discrepancies: PartialTSW controls the transported mass via its parameter $\nu(\mathcal{T})$; UOT-FM [22] uses its parameter λ to influence the regularization of marginal constraints; and ULightOT [28]'s parameter τ governs the extent of mass conservation. The adjustment of these parameters creates an Accuracy-LPIPS trade-off (see Figure 5).

Table 2 demonstrates the favorable balance of PartialTSW. Specifically, PartialTSW (with $\nu(\mathcal{T}) = 0.9$) achieves a higher accuracy of 91.06%, versus UOT-FM's (with $\lambda = 0.1$) 82.38% and ULightOT's (with $\tau = 10000$) 86.06%. Concurrently, it achieves a lower LPIPS of 0.4183 (indicating better perceptual similarity), compared to UOT-FM's 0.4713 and ULightOT's 0.4233. Furthermore, PartialTSW with $\nu(\mathcal{T}) = 0.3$ attains the highest translation accuracy of **99.11%**, significantly surpassing the accuracies of standard OT methods like SW (89.88%) and Db-TSW (89.96%).

These findings underscore PartialTSW's capability to handle significant class imbalances in image translation, offering a solution that effectively balances high target domain alignment with the preservation of perceptual similarity. Further experimental details are available in Appendix §E.9.

5 Conclusion

In this paper, we introduce Tree-Sliced Entropy Partial Transport (PartialTSW), a novel distance developed by integrating Entropy-Regularized Partial Transport for unbalanced measures on tree metric spaces with the Tree-Sliced Wasserstein (TSW) framework on tree systems. We investigate the theoretical properties of the proposed distance and establish that it constitutes a valid metric on the space of measures in Euclidean spaces. PartialTSW maintains the computational complexity of the balanced TSW distance, despite being tailored to handle unbalanced measures. Crucially, it is demonstrably faster than existing Unbalanced and Partial Optimal Transport approaches. Furthermore, comprehensive experiments demonstrate its effectiveness in addressing noise and imbalance in real-world data scenarios. A notable limitation of PartialTSW—and of existing TSW variants—is that it defines a distance without yielding explicit transport maps. An important direction for future work is therefore constructing optimal or partial transport plans within the tree-sliced setting.

Acknowledgments and Disclosure of Funding

We thank the area chairs and anonymous reviewers for their comments. TL gratefully acknowledges the support of JSPS KAKENHI Grant number 23K11243, and Mitsui Knowledge Industry Co., Ltd. grant. TT acknowledges support from the Application Driven Mathematics Program funded and organized by the Vingroup Innovation Fund and VinBigData.

This research / project is supported by the National Research Foundation Singapore under the AI Singapore Programme (AISG Award No: AISG2-TC-2023-012-SGIL). This research / project is supported by the Ministry of Education, Singapore, under the Academic Research Fund Tier 1 (FY2023) (A-8002040-00-00, A-8002039-00-00). This research / project is also supported by the NUS Presidential Young Professorship Award (A-0009807-01-00) and the NUS Artificial Intelligence Institute–Seed Funding (A-8003062-00-00).

References

[1] David Alvarez-Melis, Tommi Jaakkola, and Stefanie Jegelka. Structured optimal transport. In *International Conference on Artificial Intelligence and Statistics*, pages 1771–1780. PMLR, 2018.

[2] Yikun Bai, Bernhard Schmitzer, Matthew Thorpe, and Soheil Kolouri. Sliced optimal partial transport. In *Proceedings of the IEEE/CVF Conference on Computer Vision and Pattern Recognition*, pages 13681–13690, 2023.

[3] Tadas Baltrušaitis, Chaitanya Ahuja, and Louis-Philippe Morency. Multimodal machine learning: A survey and taxonomy. *IEEE transactions on pattern analysis and machine intelligence*, 41(2):423–443, 2018.

[4] Erhan Bayraktar and Gaoyue Guo. Strong equivalence between metrics of Wasserstein type. *Electronic Communications in Probability*, 26(none):1 – 13, 2021.

[5] Clément Bonet, Paul Berg, Nicolas Courty, François Septier, Lucas Drumetz, and Minh-Tan Pham. Spherical sliced-Wasserstein. *arXiv preprint arXiv:2206.08780*, 2022.

[6] Clément Bonet, Laetitia Chapel, Lucas Drumetz, and Nicolas Courty. Hyperbolic sliced-Wasserstein via geodesic and horospherical projections. In *Topological, Algebraic and Geometric Learning Workshops 2023*, pages 334–370. PMLR, 2023.

[7] Clément Bonet, Kimia Nadjahi, Thibault Sejourne, Kilian Fatras, and Nicolas Courty. Slicing unbalanced optimal transport. *Transactions on Machine Learning Research*, 2024.

[8] Clément Bonet, Laetitia Chapel, Lucas Drumetz, and Nicolas Courty. Hyperbolic sliced-Wasserstein via geodesic and horospherical projections. In *Proceedings of 2nd Annual Workshop on Topology, Algebra, and Geometry in Machine Learning (TAG-ML)*, pages 334–370. PMLR, 2023.

[9] Nicolas Bonneel and David Coeurjolly. SPOT: sliced partial optimal transport. *ACM Transactions on Graphics (TOG)*, 38(4):1–13, 2019.

[10] Nicolas Bonneel, Julien Rabin, Gabriel Peyré, and Hanspeter Pfister. Sliced and Radon Wasserstein barycenters of measures. *Journal of Mathematical Imaging and Vision*, 51:22–45, 2015.

[11] Charlotte Bunne, Laetitia Papaxanthos, Andreas Krause, and Marco Cuturi. Proximal optimal transport modeling of population dynamics. In *International Conference on Artificial Intelligence and Statistics*, pages 6511–6528. PMLR, 2022.

[12] Luis A Caffarelli and Robert J McCann. Free boundaries in optimal transport and Monge-Ampere obstacle problems. *Annals of mathematics*, pages 673–730, 2010.

[13] Laetitia Chapel and Romain Tavenard. One for all and all for one: Efficient computation of partial Wasserstein distances on the line. In *International Conference on Learning Representations*, 2025.

[14] Lenaic Chizat and Francis Bach. On the global convergence of gradient descent for over-parameterized models using optimal transport. *Advances in neural information processing systems*, 31, 2018.

[15] Lenaic Chizat, Gabriel Peyré, Bernhard Schmitzer, and François-Xavier Vialard. Unbalanced optimal transport: Dynamic and kantorovich formulations. *Journal of Functional Analysis*, 274(11):3090–3123, 2018.

[16] Marco Cuturi. Sinkhorn distances: Lightspeed computation of optimal transport. *Advances in neural information processing systems*, 26, 2013.

[17] Pinar Demetci, Rebecca Santorella, Manav Chakravarthy, Bjorn Sandstede, and Ritambhara Singh. Scotv2: Single-cell multiomic alignment with disproportionate cell-type representation. *Journal of Computational Biology*, 29(11):1213–1228, 2022.

[18] Ishan Deshpande, Yuan-Ting Hu, Ruoyu Sun, Ayis Pyrros, Nasir Siddiqui, Sanmi Koyejo, Zhizhen Zhao, David Forsyth, and Alexander G Schwing. Max-sliced Wasserstein distance and its use for GANs. In *Proceedings of the IEEE/CVF conference on computer vision and pattern recognition*, pages 10648–10656, 2019.

[19] Weitao Du, He Zhang, Yuanqi Du, Qi Meng, Wei Chen, Nanning Zheng, Bin Shao, and Tie-Yan Liu. Se (3) equivariant graph neural networks with complete local frames. In *International Conference on Machine Learning*, pages 5583–5608. PMLR, 2022.

[20] Richard Mansfield Dudley. The speed of mean Glivenko-Cantelli convergence. *The Annals of Mathematical Statistics*, 40(1):40–50, 1969.

[21] Steven N Evans and Frederick A Matsen. The phylogenetic Kantorovich–Rubinstein metric for environmental sequence samples. *Journal of the Royal Statistical Society: Series B (Statistical Methodology)*, 74(3):569–592, 2012.

[22] Luca Eyring, Dominik Klein, Théo Uscidda, Giovanni Palla, Niki Kilbertus, Zeynep Akata, and Fabian J Theis. Unbalancedness in neural Monge maps improves unpaired domain translation. In *The Twelfth International Conference on Learning Representations*, 2024.

[23] Jiaojiao Fan, Isabel Haasler, Johan Karlsson, and Yongxin Chen. On the complexity of the optimal transport problem with graph-structured cost. In *International Conference on Artificial Intelligence and Statistics*, pages 9147–9165. PMLR, 2022.

[24] Kilian Fatras, Thibault Sejourne, Rémi Flamary, and Nicolas Courty. Unbalanced minibatch optimal transport; applications to domain adaptation. In Marina Meila and Tong Zhang, editors, *Proceedings of the 38th International Conference on Machine Learning*, volume 139 of *Proceedings of Machine Learning Research*, pages 3186–3197. PMLR, 18–24 Jul 2021.

[25] Kilian Fatras, Younes Zine, Rémi Flamary, Remi Gribonval, and Nicolas Courty. Learning with minibatch Wasserstein : asymptotic and gradient properties. In Silvia Chiappa and Roberto Calandra, editors, *Proceedings of the Twenty Third International Conference on Artificial Intelligence and Statistics*, volume 108 of *Proceedings of Machine Learning Research*, pages 2131–2141, Online, 26–28 Aug 2020. PMLR.

[26] Charles Fefferman and Scott Markel. Recovering a feed-forward net from its output. *Advances in neural information processing systems*, 6, 1993.

[27] Alessio Figalli. The optimal partial transport problem. *Archive for rational mechanics and analysis*, 195(2):533–560, 2010.

[28] Milena Gazdieva, Arip Asadulaev, Evgeny Burnaev, and Alexander Korotin. Light unbalanced optimal transport. In *The Thirty-eighth Annual Conference on Neural Information Processing Systems*, 2024.

[29] Ziv Goldfeld and Kristjan Greenewald. Sliced mutual information: A scalable measure of statistical dependence. In M. Ranzato, A. Beygelzimer, Y. Dauphin, P.S. Liang, and J. Wortman Vaughan, editors, *Advances in Neural Information Processing Systems*, volume 34, pages 17567–17578. Curran Associates, Inc., 2021.

[30] Elisenda Grigsby, Kathryn Lindsey, and David Rolnick. Hidden symmetries of relu networks. In *International Conference on Machine Learning*, pages 11734–11760. PMLR, 2023.

[31] Allen Hatcher. *Algebraic topology*. Cambridge University Press, 2005.

[32] Xinru Hua, Truyen Nguyen, Tam Le, Jose Blanchet, and Viet Anh Nguyen. Dynamic flows on curved space generated by labeled data. In *Proceedings of the Thirty-Second International Joint Conference on Artificial Intelligence, IJCAI-23*, pages 3803–3811, 2023.

[33] Piotr Indyk. Algorithmic applications of low-distortion geometric embeddings. In *Proceedings 42nd IEEE Symposium on Foundations of Computer Science (FOCS)*, pages 10–33, 2001.

[34] Piotr Indyk and Nitin Thaper. Fast image retrieval via embeddings. In *International workshop on statistical and computational theories of vision*, volume 2, page 5, 2003.

[35] Hoang Anh Just, Feiyang Kang, Tianhao Wang, Yi Zeng, Myeongseob Ko, Ming Jin, and Ruoxi Jia. LAVA: Data valuation without pre-specified learning algorithms. In *The Eleventh International Conference on Learning Representations*, 2023.

[36] Ioannis Kalogeropoulos, Giorgos Bouritsas, and Yannis Panagakis. Scale equivariant graph metanetworks. *Advances in neural information processing systems*, 37:106800–106840, 2024.

[37] Tero Karras, Samuli Laine, and Timo Aila. A style-based generator architecture for generative adversarial networks. In *Proceedings of the IEEE/CVF conference on computer vision and pattern recognition*, pages 4401–4410, 2019.

[38] Samuel Kessler, Tam Le, and Vu Nguyen. SAVA: Scalable learning-agnostic data valuation. In *The Thirteenth International Conference on Learning Representations*, 2025.

[39] Soheil Kolouri, Kimia Nadjahi, Umut Simsekli, Roland Badeau, and Gustavo Rohde. Generalized sliced Wasserstein distances. *Advances in neural information processing systems*, 32, 2019.

[40] Stanislav Kondratyev, Léonard Monsaingeon, and Dmitry Vorotnikov. A fitness-driven cross-diffusion system from population dynamics as a gradient flow. *Journal of Differential Equations*, 261(5):2784–2808, 2016.

[41] Alexander Korotin, Nikita Gushchin, and Evgeny Burnaev. Light Schrödinger bridge. In *The Twelfth International Conference on Learning Representations*, 2024.

[42] Tam Le and Truyen Nguyen. Entropy partial transport with tree metrics: Theory and practice. In *International Conference on Artificial Intelligence and Statistics*, pages 3835–3843. PMLR, 2021.

[43] Tam Le, Truyen Nguyen, and Kenji Fukumizu. Scalable unbalanced Sobolev transport for measures on a graph. In *International Conference on Artificial Intelligence and Statistics*, pages 8521–8560. PMLR, 2023.

[44] Tam Le, Truyen Nguyen, Hideitsu Hino, and Kenji Fukumizu. An efficient Orlicz-Sobolev approach for transporting unbalanced measures on a graph. In *The Thirty-ninth Annual Conference on Neural Information Processing Systems*, 2025.

[45] Tam Le, Truyen Nguyen, Dinh Phung, and Viet Anh Nguyen. Sobolev transport: A scalable metric for probability measures with graph metrics. In *International Conference on Artificial Intelligence and Statistics*, pages 9844–9868. PMLR, 2022.

[46] Tam Le, Makoto Yamada, Kenji Fukumizu, and Marco Cuturi. Tree-sliced variants of Wasserstein distances. *Advances in neural information processing systems*, 32, 2019.

[47] Matthias Liero, Alexander Mielke, and Giuseppe Savaré. Optimal entropy-transport problems and a new Hellinger–Kantorovich distance between positive measures. *Inventiones mathematicae*, 211(3):969–1117, 2018.

[48] Ya-Wei Eileen Lin, Ronald R. Coifman, Gal Mishne, and Ronen Talmon. Tree-Wasserstein distance for high dimensional data with a latent feature hierarchy. In *The Thirteenth International Conference on Learning Representations*, 2025.

[49] Manh Luong, Khai Nguyen, Nhat Ho, Gholamreza Haffari, Dinh Phung, and Lizhen Qu. Revisiting deep audio-text retrieval through the lens of transportation. In *The Twelfth International Conference on Learning Representations*, 2024.

[50] Gonzalo Mena and Jonathan Niles-Weed. Statistical bounds for entropic optimal transport: sample complexity and the central limit theorem. In *Advances in Neural Information Processing Systems*, pages 4541–4551, 2019.

[51] Boris Muzellec, Julie Josse, Claire Boyer, and Marco Cuturi. Missing data imputation using optimal transport. In *International Conference on Machine Learning*, pages 7130–7140. PMLR, 2020.

[52] Kimia Nadjahi, Alain Durmus, Lénaïc Chizat, Soheil Kolouri, Shahin Shahrampour, and Umut Simsekli. Statistical and topological properties of sliced probability divergences. *Advances in Neural Information Processing Systems*, 33:20802–20812, 2020.

[53] Khai Nguyen, Shujian Zhang, Tam Le, and Nhat Ho. Sliced Wasserstein with random-path projecting directions. In *Forty-first International Conference on Machine Learning*, 2024.

[54] Tin D Nguyen, Brian L Trippe, and Tamara Broderick. Many processors, little time: MCMC for partitions via optimal transport couplings. In *International Conference on Artificial Intelligence and Statistics*, pages 3483–3514. PMLR, 2022.

[55] Trung Nguyen, Quang-Hieu Pham, Tam Le, Tung Pham, Nhat Ho, and Binh-Son Hua. Point-set distances for learning representations of 3d point clouds. In *Proceedings of the IEEE/CVF International Conference on Computer Vision (ICCV)*, pages 10478–10487, 2021.

[56] Vu Nguyen, Tam Le, Makoto Yamada, and Michael A Osborne. Optimal transport kernels for sequential and parallel neural architecture search. In *International Conference on Machine Learning*, pages 8084–8095. PMLR, 2021.

[57] Sloan Nietert, Ziv Goldfeld, and Rachel Cummings. Outlier-robust optimal transport: Duality, structure, and statistical analysis. In *International Conference on Artificial Intelligence and Statistics*, pages 11691–11719. PMLR, 2022.

[58] Jonathan Niles-Weed and Philippe Rigollet. Estimation of Wasserstein distances in the spiked transport model. *Bernoulli*, 28(4):2663–2688, 2022.

[59] Jungin Park, Jiyoung Lee, and Kwanghoon Sohn. Bridging vision and language spaces with assignment prediction. In *The Twelfth International Conference on Learning Representations*, 2024.

[60] François-Pierre Paty and Marco Cuturi. Subspace robust Wasserstein distances. In *Proceedings of the 36th International Conference on Machine Learning*, pages 5072–5081, 2019.

[61] Gabriel Peyré, Marco Cuturi, et al. Computational optimal transport: With applications to data science. *Foundations and Trends® in Machine Learning*, 11(5-6):355–607, 2019.

[62] Khiem Pham, Khang Le, Nhat Ho, Tung Pham, and Hung Bui. On unbalanced optimal transport: An analysis of Sinkhorn algorithm. In Hal Daumé III and Aarti Singh, editors, *Proceedings of the 37th International Conference on Machine Learning*, volume 119 of *Proceedings of Machine Learning Research*, pages 7673–7682. PMLR, 13–18 Jul 2020.

[63] Thong Pham, Shohei Shimizu, Hideitsu Hino, and Tam Le. Scalable counterfactual distribution estimation in multivariate causal models. In *Conference on Causal Learning and Reasoning (CLeaR)*, 2024.

[64] Stanislav Pidhorskyi, Donald A Adjeroh, and Gianfranco Doretto. Adversarial latent autoencoders. In *Proceedings of the IEEE/CVF conference on computer vision and pattern recognition*, pages 14104–14113, 2020.

[65] Michael Quellmalz, Robert Beinert, and Gabriele Steidl. Sliced optimal transport on the sphere. *Inverse Problems*, 39(10):105005, 2023.

[66] Julien Rabin, Gabriel Peyré, Julie Delon, and Marc Bernot. Wasserstein barycenter and its application to texture mixing. In *International Conference on Scale Space and Variational Methods in Computer Vision*, pages 435–446, 2011.

[67] Julien Rabin, Gabriel Peyré, Julie Delon, and Marc Bernot. Wasserstein barycenter and its application to texture mixing. In *Scale Space and Variational Methods in Computer Vision: Third International Conference, SSVM 2011, Ein-Gedi, Israel, May 29–June 2, 2011, Revised Selected Papers 3*, pages 435–446. Springer, 2012.

[68] Gathika Ratnayaka, James Nichols, and Qing Wang. Learning partial graph matching via optimal partial transport. In *The Thirteenth International Conference on Learning Representations*, 2025.

[69] Grant Rotskoff, Samy Jelassi, Joan Bruna, and Eric Vanden-Eijnden. Global convergence of neuron birth-death dynamics. In Kamalika Chaudhuri and Ruslan Salakhutdinov, editors, *Proceedings of the 36th International Conference on Machine Learning*, volume 97 of *Proceedings of Machine Learning Research*, pages 5508–5517, 2019.

[70] Mahdi Saleh, Shun-Cheng Wu, Luca Cosmo, Nassir Navab, Benjamin Busam, and Federico Tombari. Bending graphs: Hierarchical shape matching using gated optimal transport. In *Proceedings of the IEEE/CVF Conference on Computer Vision and Pattern Recognition (CVPR)*, pages 11757–11767, 2022.

[71] Vıctor Garcia Satorras, Emiel Hoogeboom, and Max Welling. E (n) equivariant graph neural networks. In *International conference on machine learning*, pages 9323–9332. PMLR, 2021.

[72] Geoffrey Schiebinger, Jian Shu, Marcin Tabaka, Brian Cleary, Vidya Subramanian, Aryeh Solomon, Joshua Gould, Siyan Liu, Stacie Lin, Peter Berube, et al. Optimal-transport analysis of single-cell gene expression identifies developmental trajectories in reprogramming. *Cell*, 176(4):928–943, 2019.

[73] Thibault Séjourné, Gabriel Peyré, and François-Xavier Vialard. Unbalanced optimal transport, from theory to numerics. *arXiv preprint arXiv:2211.08775*, 2022.

[74] Thibault Sejourne, Francois-Xavier Vialard, and Gabriel Peyré. Faster unbalanced optimal transport: Translation invariant Sinkhorn and 1-D Frank-Wolfe. In *Proceedings of The 25th International Conference on Artificial Intelligence and Statistics*, volume 151, pages 4995–5021. PMLR, 2022.

[75] Charles Semple and A Mike. Steel, phylogenetics, vol. 24. *Oxford Lecture Series in Mathematics and its Applications. Oxford University Press, Oxford*, 2003.

[76] Justin Solomon, Fernando De Goes, Gabriel Peyré, Marco Cuturi, Adrian Butscher, Andy Nguyen, Tao Du, and Leonidas Guibas. Convolutional Wasserstein distances: Efficient optimal transportation on geometric domains. *ACM Transactions on Graphics (TOG)*, 34(4):66, 2015.

[77] Ilya Tolstikhin, Olivier Bousquet, Sylvain Gelly, and Bernhard Schoelkopf. Wasserstein auto-encoders. In *International Conference on Learning Representations*, 2018.

[78] Hoang Tran, Thieu Vo, Tho Huu, Tan Nguyen, et al. Monomial matrix group equivariant neural functional networks. *Advances in Neural Information Processing Systems*, 37:48628–48665, 2025.

[79] Hoang V. Tran, Thanh Chu, Minh-Khoi Nguyen-Nhat, Huyen Trang Pham, Tam Le, and Tan Minh Nguyen. Spherical tree-sliced Wasserstein distance. In *The Thirteenth International Conference on Learning Representations*, 2025.

[80] Hoang V. Tran, Minh-Khoi Nguyen-Nhat, Huyen Trang Pham, Thanh Chu, Tam Le, and Tan Minh Nguyen. Distance-based tree-sliced Wasserstein distance. In *The Thirteenth International Conference on Learning Representations*, 2025.

[81] Hoang V. Tran, Huyen Trang Pham, Tho Tran Huu, Minh-Khoi Nguyen-Nhat, Thanh Chu, Tam Le, and Tan Minh Nguyen. Tree-sliced Wasserstein distance: A geometric perspective. In *Forty-second International Conference on Machine Learning*, 2025.

[82] Hoang-Viet Tran, Thieu N Vo, Tho Tran Huu, and Tan Minh Nguyen. A clifford algebraic approach to e (n)-equivariant high-order graph neural networks. *arXiv preprint arXiv:2410.04692*, 2024.

[83] Huy Tran, Yikun Bai, Abihith Kothapalli, Ashkan Shahbazi, Xinran Liu, Rocio P Diaz Martin, and Soheil Kolouri. Stereographic spherical sliced Wasserstein distances. In *Forty-first International Conference on Machine Learning*, 2024.

[84] Thanh Tran, Hoang V. Tran, Thanh Chu, Huyen Trang Pham, Laurent Ghaoui, Tam Le, and Tan Minh Nguyen. Tree-sliced Wasserstein distance with nonlinear projection. In *Forty-second International Conference on Machine Learning*, 2025.

[85] Viet-Hoang Tran, Van Hoan Trinh, Khanh Vinh Bui, and Tan M Nguyen. On linear mode connectivity of mixture-of-experts architectures. *arXiv preprint arXiv:2509.11348*, 2025.

[86] Viet-Hoang Tran, Thieu N Vo, An Nguyen The, Tho Tran Huu, Minh-Khoi Nguyen-Nhat, Thanh Tran, Duy-Tung Pham, and Tan Minh Nguyen. Equivariant neural functional networks for transformers. *arXiv preprint arXiv:2410.04209*, 2024.

[87] C. Villani. *Optimal Transport: Old and New*, volume 338. Springer Science & Business Media, 2008.

[88] Thieu N Vo, Viet-Hoang Tran, Tho Tran Huu, An Nguyen The, Thanh Tran, Minh-Khoi Nguyen-Nhat, Duy-Tung Pham, and Tan Minh Nguyen. Equivariant polynomial functional networks. *arXiv preprint arXiv:2410.04213*, 2024.

[89] Anh-Khoa Nguyen Vu, Thanh-Toan Do, Vinh-Tiep Nguyen, Tam Le, Minh-Triet Tran, and Tam V Nguyen. Few-shot object detection via synthetic features with optimal transport. *Computer Vision and Image Understanding*, page 104350, 2025.

[90] Richard Zhang, Phillip Isola, Alexei A Efros, Eli Shechtman, and Oliver Wang. The unreasonable effectiveness of deep features as a perceptual metric. In *CVPR*, 2018.

[91] Bo Zhao, Robert M Gower, Robin Walters, and Rose Yu. Improving convergence and generalization using parameter symmetries. *arXiv preprint arXiv:2305.13404*, 2023.

Table of Notation

$\mathbb{R}^d$	d-dimensional Euclidean space
$\|\cdot\|_2$	Euclidean norm
$\langle\cdot,\cdot\rangle$	standard dot product
$\mathbb{S}^{d-1}$	$(d-1)$-dimensional hypersphere
θ	unit vector
$\sqcup$	disjoint union
$L^1(X)$	space of Lebesgue integrable functions on X
$\mathcal{P}(X)$	space of probability measures on X
$\mathcal{M}(X)$	space of measures on X
μ, ν	measures
$\delta(\cdot)$	1-dimensional Dirac delta function
$\mathcal{U}(\mathbb{S}^{d-1})$	uniform distribution on $\mathbb{S}^{d-1}$
$\sharp$	pushforward (measure)
$\mathcal{C}(X, Y)$	space of continuous maps from X to Y
$\mathtt{d}(\cdot,\cdot)$	metric in metric space
$d_{\mathcal{T}}(\cdot,\cdot)$	tree metric
$\mathrm{T}(d)$	translation group of order d
$\mathrm{O}(d)$	orthogonal group of order d
$\mathrm{E}(d)$	Euclidean group of order d
g	element of group
W_p	p-Wasserstein distance
SW_p	Sliced p-Wasserstein distance
Λ	(rooted) subtree
e	edge in graph
w_e	weight of edge in graph
l	line, index of line
$\mathcal{L}$	system of lines, tree system
$\bar{\mathcal{L}}$	ground set of system of lines, tree system
$\mathbb{L}_k^d$	space of systems of k lines in $\mathbb{R}^d$
$\mathcal{T}$	tree structure in system of lines
L	number of tree systems
k	number of lines in a system of lines or a tree system
$\mathcal{R}^\alpha$	Radon Transform on Systems of Lines
Δ_{k-1}	$(k-1)$-dimensional standard simplex
α	splitting map
ξ	tuning parameter in splitting maps
$\mathbb{T}$	space of tree systems
σ	distribution on space of tree systems

Appendix of "Tree-Sliced Entropy Partial Transport"

Table of Contents

A Background on Optimal Transport on Metric Spaces with Tree Metrics

Let $\mathcal{T} = (V, E)$ be a tree rooted at a node r, where each edge $e \in E$ is assigned a nonnegative length w_e. Here, V denotes the set of nodes and E the set of edges. For notational convenience, we use $\mathcal{T}$ to also refer to the union of all nodes and the continuous points along the edges. We now recall the formal definition of a tree metric:

Definition A.1 (Tree metric [75, Section 7, p.145–182])**.** A metric $\mathtt{d} : \Omega \times \Omega \to [0, \infty)$ is said to be a *tree metric* on a set Ω if there exists a tree $\mathcal{T}$ such that $\Omega \subset \mathcal{T}$ and, for all $x, y \in \Omega$, the distance $\mathtt{d}(x, y)$ equals the length of the unique path in $\mathcal{T}$ connecting x and y.

Suppose V is a subset of a vector space, and let $d_{\mathcal{T}}(\cdot, \cdot)$ denote the tree metric defined on $\mathcal{T}$. We denote by $[x, y]$ the unique shortest path in $\mathcal{T}$ between any two points x and y. Let ω be the unique Borel (length) measure on $\mathcal{T}$ satisfying $\omega([x, y]) = d_{\mathcal{T}}(x, y)$ for all $x, y \in \mathcal{T}$. For any $x \in \mathcal{T}$, we define the subtree rooted at x by

$$\Lambda(x) \coloneqq \{y \in \mathcal{T} : x \in [r, y]\}. \tag{18}$$

Let $\mathcal{P}(\mathcal{T})$ denote the set of all probability measures on $\mathcal{T}$, i.e., Borel measures with total mass equal to one. The following result provides a closed-form expression for the 1-Wasserstein distance on the tree metric space $\mathcal{T}$.

Theorem A.2 (Optimal Transport on Tree Metric Spaces [46, Section 3, Proposition 1])**.** *For any $\mu, \nu \in \mathcal{P}(\mathcal{T})$, the 1-Wasserstein distance with respect to the tree metric $d_{\mathcal{T}}$ is given by*

$$\mathrm{W}_{1,d_{\mathcal{T}}}(\mu, \nu) = \int_{\mathcal{T}} |\mu(\Lambda(x)) - \nu(\Lambda(x))| \, \omega(dx). \tag{19}$$

B Background on Entropy Partial Transport on Metric Spaces with Tree Metrics

In this section, we revisit the Entropy Partial Transport (EPT) formulation introduced in [42] for completeness. All theoretical proofs are outlined in Appendix D.

We denote by $\mathcal{M}(\mathcal{T})$ the collection of all nonnegative Borel measures on $\mathcal{T}$ with finite total mass. Let $C(\mathcal{T})$ denote the space of continuous functions defined on $\mathcal{T}$, and let $L^\infty(\mathcal{T})$ denote the space of Borel measurable functions on $\mathcal{T}$ that are essentially bounded with respect to the measure ω. The space $L^\infty(\mathcal{T})$ forms a Banach space when equipped with the norm

$$\|f\|_{L^\infty(\mathcal{T})} \coloneqq \inf \left\{\bar{a} \in \mathbb{R} : |f(x)| \le \bar{a} \text{ for } \omega\text{-almost every } x \in \mathcal{T}\right\}. \tag{20}$$

Let $\mathcal{M}(\mathcal{T} \times \mathcal{T})$ denote the space of all nonnegative Borel measures on $\mathcal{T} \times \mathcal{T}$ with finite total mass. Given $\mu, \nu \in \mathcal{M}(\mathcal{T})$, define the set of admissible partial couplings as

$$\Pi_{\le}(\mu, \nu) := \left\{\gamma \in \mathcal{M}(\mathcal{T} \times \mathcal{T}) : \gamma_1 \le \mu, \ \gamma_2 \le \nu\right\}, \tag{21}$$

where γ_1 and γ_2 represent the marginals of γ on the first and second coordinates, respectively.

For any $\gamma \in \Pi_{\le}(\mu, \nu)$, let f_1 and f_2 be the Radon–Nikodym derivatives of γ_1 with respect to μ and γ_2 with respect to ν, respectively. That is, $\gamma_1 = f_1\mu$ and $\gamma_2 = f_2\nu$, with the constraints $0 \le f_1 \le 1$ μ-a.e. and $0 \le f_2 \le 1$ ν-a.e.

Let $w : \mathcal{T} \to [0, \infty)$ be a b-Lipschitz continuous and nonnegative weight function, defined by

$$w(x) = a_1 \, d_{\mathcal{T}}(x, x_0) + a_0, \tag{22}$$

where $x_0 \in \mathcal{T}$, $a_1 \in [0, b]$, and $a_0 \in [0, \infty)$. Here, $d_{\mathcal{T}}(\cdot, \cdot)$ denotes the tree metric over $\mathcal{T}$. We use the entropy function $F : [0, \infty) \to (0, \infty)$ given by

$$F(s) = |s - 1|.$$

Letting $\bar{m} := \min\{\mu(\mathcal{T}), \nu(\mathcal{T})\}$, and fixing $m \in [0, \bar{m}]$, the EPT problem is formulated as

$$\mathcal{W}_m(\mu, \nu) := \inf_{\substack{\gamma \in \Pi_{\le}(\mu,\nu) \\ \gamma(\mathcal{T}\times\mathcal{T}) = m}} \left[\mathcal{F}_1(\gamma_1 \mid \mu) + \mathcal{F}_2(\gamma_2 \mid \nu) + b \int_{\mathcal{T}\times\mathcal{T}} d_{\mathcal{T}}(x, y) \, \gamma(dx, dy)\right], \tag{23}$$

where the regularization terms are defined as the weighted relative entropies

$$\mathcal{F}_1(\gamma_1 \mid \mu) := \int_{\mathcal{T}} w(x)\, F(f_1(x))\, \mu(dx), \quad \mathcal{F}_2(\gamma_2 \mid \nu) := \int_{\mathcal{T}} w(x)\, F(f_2(x))\, \nu(dx). \tag{24}$$

To handle the mass constraint $\gamma(\mathcal{T} \times \mathcal{T}) = m$, we introduce a Lagrange multiplier $\lambda \in \mathbb{R}$ and instead consider the relaxed objective

$$\mathrm{ET}_\lambda(\mu, \nu) := \inf_{\gamma \in \Pi_\leq(\mu,\nu)} \left[\mathcal{F}_1(\gamma_1 \mid \mu) + \mathcal{F}_2(\gamma_2 \mid \nu) + b \int_{\mathcal{T}\times\mathcal{T}} (d_{\mathcal{T}}(x, y) - \lambda)\, \gamma(dx, dy) \right]. \tag{25}$$

We now expand the entropic terms and define

$$\begin{aligned} \mathcal{C}_\lambda(\gamma) := \int_{\mathcal{T}} w(x)\, \mu(dx) + \int_{\mathcal{T}} w(x)\, \nu(dx) - \int_{\mathcal{T}} w(x)\, \gamma_1(dx) - \int_{\mathcal{T}} w(x)\, \gamma_2(dx) \\ + b \int_{\mathcal{T}\times\mathcal{T}} (d_{\mathcal{T}}(x, y) - \lambda)\, \gamma(dx, dy), \end{aligned} \tag{26}$$

so that Equation (25) is equivalent to

$$\mathrm{ET}_\lambda(\mu, \nu) = \inf_{\gamma \in \Pi_\leq(\mu,\nu)} \mathcal{C}_\lambda(\gamma). \tag{27}$$

As established in [42, Theorem 3.1, part i)], the solutions to Equation (23) and Equation (27) are related via the identity

$$\mathcal{W}_m(\mu, \nu) = \mathrm{ET}_\lambda(\mu, \nu) + \lambda b\, m. \tag{28}$$

Inspired by the construction proposed by Caffarelli and McCann [12], we recast the entropy-regularized partial transport problem in Equation (27) as a classical optimal transport (OT) problem between balanced measures. To achieve this, we augment the original domain $\mathcal{T}$ by introducing an auxiliary point $\hat{s} \notin \mathcal{T}$, and define the extended space $\hat{\mathcal{T}} := \mathcal{T} \cup \{\hat{s}\}$.

We then lift the unbalanced measures $\mu, \nu \in \mathcal{M}(\mathcal{T})$ to balanced counterparts supported on $\hat{\mathcal{T}}$:

$$\hat{\mu} := \mu + \nu(\mathcal{T})\, \delta_{\hat{s}}, \quad \hat{\nu} := \nu + \mu(\mathcal{T})\, \delta_{\hat{s}}, \tag{29}$$

where $\delta_{\hat{s}}$ denotes the Dirac measure at point $\hat{s}$. Next, we define a cost function $\hat{c} : \hat{\mathcal{T}} \times \hat{\mathcal{T}} \to \mathbb{R}$ that extends the original transport cost:

$$\hat{c}(x, y) := \begin{cases} b\,[d_{\mathcal{T}}(x, y) - \lambda] & \text{if } x, y \in \mathcal{T}, \\ w(x) & \text{if } x \in \mathcal{T} \text{ and } y = \hat{s}, \\ w(y) & \text{if } y \in \mathcal{T} \text{ and } x = \hat{s}, \\ 0 & \text{if } x = y = \hat{s}. \end{cases} \tag{30}$$

Using this extended cost, we formulate the balanced OT problem over $\hat{\mu}$ and $\hat{\nu}$:

$$\mathrm{KT}(\hat{\mu}, \hat{\nu}) := \inf_{\hat{\gamma} \in \Gamma(\hat{\mu},\hat{\nu})} \int_{\hat{\mathcal{T}}\times\hat{\mathcal{T}}} \hat{c}(x, y)\, \hat{\gamma}(dx, dy), \tag{31}$$

where the set of admissible transport plans $\Gamma(\hat{\mu}, \hat{\nu})$ is given by:

$$\Gamma(\hat{\mu}, \hat{\nu}) := \left\{ \hat{\gamma} \in \mathcal{M}(\hat{\mathcal{T}} \times \hat{\mathcal{T}}) : \hat{\gamma}(U \times \hat{\mathcal{T}}) = \hat{\mu}(U),\ \hat{\gamma}(\hat{\mathcal{T}} \times U) = \hat{\nu}(U),\ \forall \text{ Borel set } U \subset \hat{\mathcal{T}} \right\}. \tag{32}$$

The connection between the entropy-regularized partial transport formulation ET_λ in Equation (27) and the balanced optimal transport problem KT in Equation (31) is established by the following result.

Proposition B.1 (Equivalence of ET_λ and KT)**.** *Let $\mu, \nu \in \mathcal{M}(\mathcal{T})$. Then the two formulations coincide:*

$$\mathrm{ET}_\lambda(\mu, \nu) = \mathrm{KT}(\hat{\mu}, \hat{\nu}). \tag{33}$$

Furthermore, the optimal plans γ for the partial transport problem and $\hat{\gamma}$ for the balanced transport problem are related by:

$$\hat{\gamma} = \gamma + (1 - f_1)\mu \otimes \delta_{\hat{s}} + \delta_{\hat{s}} \otimes (1 - f_2)\nu + \gamma(\mathcal{T} \times \mathcal{T})\, \delta_{(\hat{s},\hat{s})}, \tag{34}$$

where f_1 and f_2 are the Radon–Nikodym derivatives of the marginals of γ with respect to μ and ν, respectively.

The detailed proof is provided in Appendix §D.1. Note that KT corresponds to a classical optimal transport problem defined between two balanced measures over the extended space $\hat{\mathcal{T}}$ and governed by the cost function $\hat{c}$. This allows us to invoke standard OT duality theory, such as [12, Corollary 2.6], to obtain a variational dual formulation for ET_λ, as described below.

Theorem B.2 (Dual Representation of ET_λ)**.** *The dual problem associated with the entropy-regularized partial transport functional $\mathrm{ET}_\lambda(\mu,\nu)$ is given by:*

$$\mathrm{ET}_\lambda(\mu,\nu) = \sup\left\{\int_{\mathcal{T}} f\,(d\mu - d\nu) : f \in \mathbb{L}\right\} - \frac{b\lambda}{2}\left[\mu(\mathcal{T}) + \nu(\mathcal{T})\right], \tag{35}$$

where the admissible function class $\mathbb{L}$ is defined as

$$\mathbb{L} := \left\{ f \in C(\mathcal{T}) : -w - \frac{b\lambda}{2} \le f \le w + \frac{b\lambda}{2}, \quad |f(x) - f(y)| \le b\, d_{\mathcal{T}}(x,y) \text{ for all } x, y \in \mathcal{T} \right\}.$$

The proof of Theorem B.2 is deferred to Appendix §D.2. To obtain a tractable approximation of the dual problem, we introduce a regularization based on a restricted class of test functions. Let r denote the root of the tree $\mathcal{T}$, and let ω be the associated length measure on $\mathcal{T}$. For a fixed parameter $a \in [0, \frac{b\lambda}{2} + w(r)]$, define the function class $\mathbb{L}_a$ to consist of all functions $f : \mathcal{T} \to \mathbb{R}$ of the form:

$$f(x) = s + \int_{[r,x]} g(y)\,\omega(dy), \tag{36}$$

where s is a constant satisfying

$$s \in \left[-w(r) - \frac{b\lambda}{2} + a,\ w(r) + \frac{b\lambda}{2} - a\right], \tag{37}$$

and $g \in L^\infty(\mathcal{T})$ is a bounded function with $\|g\|_{L^\infty(\mathcal{T})} \le b$.

The a-regularized entropy partial transport is then defined as:

$$\widetilde{\mathrm{ET}}^a_\lambda(\mu,\nu) := \sup_{f \in \mathbb{L}_a}\left\{\int_{\mathcal{T}} f\,(d\mu - d\nu)\right\} - \frac{b\lambda}{2}\left[\mu(\mathcal{T}) + \nu(\mathcal{T})\right]. \tag{38}$$

This regularized formulation admits an explicit closed-form expression:

Proposition B.3 (Closed-Form Solution for $\widetilde{\mathrm{ET}}^a_\lambda$)**.** *For $\mu, \nu \in \mathcal{M}(\mathcal{T})$, we have:*

$$\begin{aligned}\widetilde{\mathrm{ET}}^a_\lambda(\mu,\nu) = &\int_{\mathcal{T}} |\mu(\Lambda(x)) - \nu(\Lambda(x))|\ \omega(dx) \\ &- \frac{b\lambda}{2}\left[\mu(\mathcal{T}) + \nu(\mathcal{T})\right] + \left(w(r) + \frac{b\lambda}{2} - a\right)|\mu(\mathcal{T}) - \nu(\mathcal{T})|.\end{aligned} \tag{39}$$

The proof is provided in Appendix §D.3. We now compare the original entropy transport value ET_λ with its regularized approximation $\widetilde{\mathrm{ET}}^a_\lambda$:

Proposition B.4 (Comparison Bounds between ET_λ and $\widetilde{\mathrm{ET}}^a_\lambda$)**.** *The following inequalities hold:*

$$\mathrm{ET}_\lambda(\mu,\nu) \le \widetilde{\mathrm{ET}}^0_\lambda(\mu,\nu), \tag{40}$$

and if the condition

$$[4L_{\mathcal{T}} - \lambda]b \le 2w(r), \quad \text{where } L_{\mathcal{T}} := \max_{x \in \mathcal{T}} \omega([r,x]), \tag{41}$$

is satisfied, then

$$\widetilde{\mathrm{ET}}^a_\lambda(\mu,\nu) \le \mathrm{ET}_\lambda(\mu,\nu) \tag{42}$$

for all a such that $2bL_{\mathcal{T}} \le a \le \frac{b\lambda}{2} + w(r)$.

The proof appears in Appendix §D.4. For $0 \le a < \frac{b\lambda}{2} + w(r)$, recall that the regularized transport cost is defined as:

$$d_a(\mu,\nu) := \widetilde{\mathrm{ET}}^a_\lambda(\mu,\nu) + \frac{b\lambda}{2}\left[\mu(\mathcal{T}) + \nu(\mathcal{T})\right]. \tag{43}$$

This cost function defines a genuine metric, as shown below:

Proposition B.5 (Metric Structure of d_a)**.** *$(\mathcal{M}(\mathcal{T}), d_a)$ is a complete metric space.*

The proof is presented in Appendix §D.5.

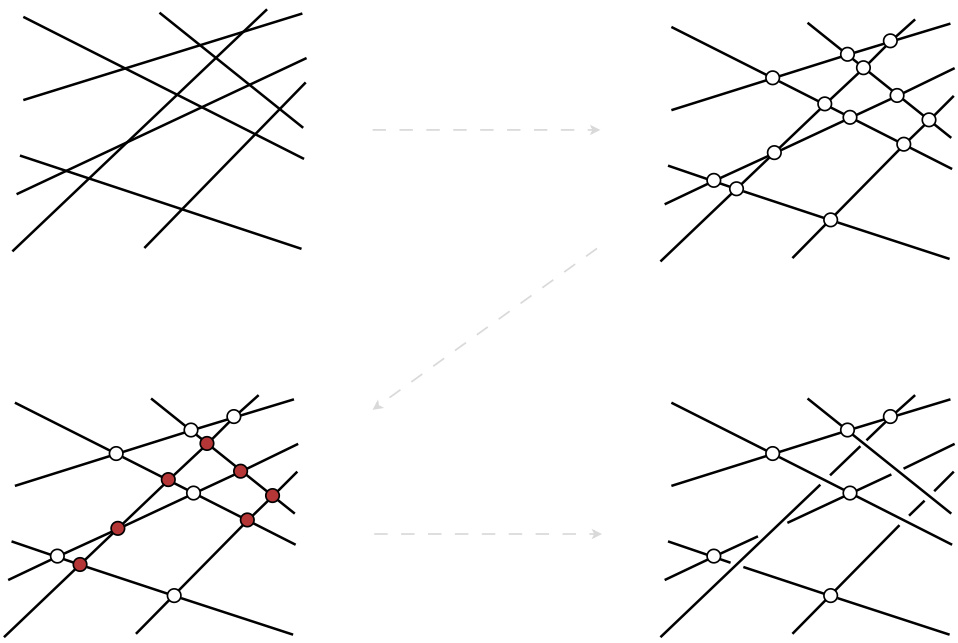

Figure 6: An illustration of the tree system construction is presented in the two-dimensional space $\mathbb{R}^2$, though the method readily generalizes to higher dimensions. The process starts with a collection of infinite lines arranged without any inherent structure. All pairwise intersections among these lines are identified (some of which may not be visible in the figure due to the lines' unbounded nature). A subset of intersections is selected and marked in red to indicate those to be discarded. The remaining intersections are retained to enforce a tree structure on the system—ensuring that any two points lying on the lines are connected by a unique path that passes only through the preserved intersections. These remaining intersections act as the essential nodes that define the tree topology. Once the red (discarded) intersections are removed, the resulting configuration forms the desired tree system.

C Background on Tree-Sliced Wasserstein Distance on Euclidean Spaces

This section reviews foundational concepts underlying the Tree-Sliced Wasserstein distance defined over Tree Systems. To ensure completeness, we revisit key definitions and theoretical formulations; detailed proofs and additional exposition are available in [81, 80].

C.1 Tree System

Line. A *line* in the Euclidean space $\mathbb{R}^d$ is specified by a tuple $(x, \theta) \in \mathbb{R}^d \times \mathbb{S}^{d-1}$ and is expressed parametrically as $x + t \cdot \theta$ for $t \in \mathbb{R}$. Throughout, we use $l = (x_l, \theta_l) \in \mathbb{R}^d \times \mathbb{S}^{d-1}$ to denote a line, where x_l denotes the *source* point and θ_l the *direction* vector.

System of lines. Given an integer $k \geq 1$, a *system of k lines in $\mathbb{R}^d$* refers to a collection of k such lines. The notation $(\mathbb{R}^d \times \mathbb{S}^{d-1})^k$ is abbreviated as $\mathbb{L}_k^d$, representing the *space of systems of k lines in $\mathbb{R}^d$*. An element in this space, commonly denoted by $\mathcal{L}$, corresponds to a specific system of lines.

Tree System. A system $\mathcal{L}$ is said to be *connected* if the union of all points lying on the constituent lines forms a connected subset of $\mathbb{R}^d$. By selectively *removing* certain intersection points between the lines, one can enforce a tree structure on $\mathcal{L}$—yielding a *tree system*—in which any two points are connected by a unique path. An illustration of this construction is provided in Figure 6.

Remark C.1. The term *tree system* is used because there is a unique path between any two points, analogous to the definition of trees in graph theory.

Beginning with the remaining intersections, we employ the concepts of disjoint union and quotient topology [31] to construct a tree system by coherently gluing together multiple copies of $\mathbb{R}$. This

topological framework induces a natural metric, under which the resulting space satisfies the properties of a tree metric space.

Sampling Procedure for Chain-Structured Tree Systems. The space of tree systems is inherently rich and diverse, primarily due to the wide range of possible underlying tree topologies. [81] presents a general framework that accommodates arbitrary tree structures, while placing particular emphasis on a subclass of chain-like trees. The following describes the sampling procedure for generating tree systems with this chain-based architecture:

Step 1. Draw an initial point $x_1 \sim \mu_1$ and a direction $\theta_1 \sim \nu_1$, where μ_1 is a probability measure on $\mathbb{R}^d$ and ν_1 is a measure on the unit sphere $\mathbb{S}^{d-1}$.

Step i. For each subsequent node, sample $t_i \sim \mu_i$ and $\theta_i \sim \nu_i$, then compute $x_i = x_{i-1} + t_i \cdot \theta_{i-1}$. Here, μ_i is a distribution over $\mathbb{R}$ and ν_i over $\mathbb{S}^{d-1}$.

All distributions μ_i and ν_i are assumed to be mutually independent. Specifically, we consider the following choices: The initial position distribution μ_1 is supported on a bounded subset of $\mathbb{R}^d$, such as the uniform distribution over the cube $[-1, 1]^d$, i.e., $\mathcal{U}([-1, 1]^d)$; For $i > 1$, each μ_i is defined on a bounded interval of $\mathbb{R}$—for example, $\mathcal{U}([-1, 1])$; Finally, each direction θ_i is drawn from a distribution over the unit sphere, e.g., the uniform distribution $\mathcal{U}(\mathbb{S}^{d-1})$. An example of such a tree system is illustrated in Figure 6.

Remark C.2. This generative process induces a probability measure σ on the space $\mathbb{T}$ of all chain-structured tree systems produced via this construction.

C.2 A Variant of Radon Transform for Systems of Lines

Let $L^1(\mathbb{R}^d)$ denote the space of Lebesgue integrable functions on $\mathbb{R}^d$, equipped with the standard L^1 norm $\|\cdot\|_1$. Consider a configuration of k lines $\mathcal{L} \in \mathbb{L}_k^d$. A real-valued function f defined on the domain $\bar{\mathcal{L}}$ consists of all points of $\mathcal{L}$, is said to be *integrable over the line system* if the following condition holds:

$$\|f\|_{\mathcal{L}} \coloneqq \sum_{l \in \mathcal{L}} \int_{\mathbb{R}} |f(t_x, l)| \, dt_x < \infty. \tag{44}$$

The set of such functions is denoted by $L^1(\mathcal{L})$, representing the space of Lebesgue integrable functions over the line system $\mathcal{L}$. Recall the standard $(k-1)$-simplex:

$$\Delta_{k-1} = \left\{ (a_l)_{l \in \mathcal{L}} \in \mathbb{R}^k \mid a_l \geq 0, \sum_{l \in \mathcal{L}} a_l = 1 \right\}. \tag{45}$$

Define the space $\mathcal{C}(\mathbb{R}^d \times \mathbb{L}_k^d, \Delta_{k-1})$ as the set of continuous maps from $\mathbb{R}^d \times \mathbb{L}_k^d$ to Δ_{k-1}, referred to as *splitting maps*. Given a line system $\mathcal{L} \in \mathbb{L}_k^d$ and a splitting map $\alpha \in \mathcal{C}(\mathbb{R}^d \times \mathbb{L}_k^d, \Delta_{k-1})$, we define a linear operator that projects a function $f \in L^1(\mathbb{R}^d)$ to the line system $\mathcal{L}$ as follows:

$$\mathcal{R}_{\mathcal{L}}^{\alpha} f \colon \bar{\mathcal{L}} \longrightarrow \mathbb{R} \tag{46}$$

$$(x, l) \longmapsto \int_{\mathbb{R}^d} f(y) \cdot \alpha(y, \mathcal{L})_l \cdot \delta\left(t_x - \langle y - x_l, \theta_l \rangle\right) \, dy, \tag{47}$$

where δ denotes the Dirac delta function in one dimension, and (x_l, θ_l) encodes the location and direction of line l. It can be shown that $\mathcal{R}_{\mathcal{L}}^{\alpha} f$ belongs to $L^1(\mathcal{L})$ for any $f \in L^1(\mathbb{R}^d)$, and furthermore satisfies the inequality

$$\|\mathcal{R}_{\mathcal{L}}^{\alpha} f\|_{\mathcal{L}} \leq \|f\|_1.$$

Hence, the operator $\mathcal{R}_{\mathcal{L}}^{\alpha} \colon L^1(\mathbb{R}^d) \to L^1(\mathcal{L})$ is well-defined. These properties are proven in [80]. Extending this to all line systems, we define the *Radon transform on Systems of Lines* as follows. For a fixed splitting map $\alpha \in \mathcal{C}(\mathbb{R}^d \times \mathbb{L}_k^d, \Delta_{k-1})$, define:

$$\mathcal{R}^{\alpha} \colon L^1(\mathbb{R}^d) \longrightarrow \prod_{\mathcal{L} \in \mathbb{L}_k^d} L^1(\mathcal{L}) \tag{48}$$

$$f \longmapsto \left(\mathcal{R}_{\mathcal{L}}^{\alpha} f\right)_{\mathcal{L} \in \mathbb{L}_k^d}. \tag{49}$$

If the splitting map α is invariant under the Euclidean group $\mathrm{E}(d)$—the group of all isometries of $\mathbb{R}^d$—then the operator $\mathcal{R}^{\alpha}$ is injective.

C.3 Tree-Sliced Wasserstein Distance for Probability Measures on Euclidean Spaces

Let $\mu, \nu \in \mathcal{P}(\mathbb{R}^d)$ be probability measures. For a tree-structured system of lines $\mathcal{L} \in \mathbb{T}$ and an $\mathrm{E}(d)$-invariant splitting map $\alpha \in \mathcal{C}(\mathbb{R}^d \times \mathbb{L}_k^d, \Delta_{k-1})$, the transform $\mathcal{R}_{\mathcal{L}}^{\alpha}$ pushes forward μ and ν to corresponding measures $\mathcal{R}_{\mathcal{L}}^{\alpha}\mu$ and $\mathcal{R}_{\mathcal{L}}^{\alpha}\nu$ on $\mathcal{L}$. Since each $\mathcal{L} \in \mathbb{T}$ is equipped with a tree metric $d_{\mathcal{L}}$, the 1-Wasserstein distance $\mathrm{W}_{d_{\mathcal{L}},1}$ between the transformed measures can be computed. This leads to the following definition of the *Distance-based Tree-Sliced Wasserstein* (Db-TSW) [80] distance:

$$\text{Db-TSW}(\mu, \nu) \coloneqq \int_{\mathbb{T}} \mathrm{W}_{d_{\mathcal{L}},1} \left(\mathcal{R}_{\mathcal{L}}^{\alpha}\mu, \mathcal{R}_{\mathcal{L}}^{\alpha}\nu\right) \, d\sigma(\mathcal{L}), \tag{50}$$

where σ is a probability measure over the space of tree systems $\mathbb{T}$. It is important to note that the value of Db-TSW depends on the choice of the tree system space $\mathbb{T}$, the sampling distribution σ, and the specific $\mathrm{E}(d)$-invariant splitting map α, although these dependencies are omitted from the notation for brevity. The resulting Db-TSW defines an $\mathrm{E}(d)$-invariant metric on $\mathcal{P}(\mathbb{R}^d)$.

Remark C.3. As established in [80], if the tree systems consist solely of a single line, the Db-TSW distance reduces exactly to the classical Sliced Wasserstein (SW) distance on $\mathbb{R}^d$.

Constructing $\mathrm{E}(d)$-Invariant Splitting Maps. The Euclidean group $\mathrm{E}(d)$ consists of all transformations of $\mathbb{R}^d$ that preserve pairwise Euclidean distances. As such, this invariance extends not only to distances between points but also to the shortest distance from a point to a line. Given a point $x \in \mathbb{R}^d$ and a system of lines $\mathcal{L} \in \mathbb{L}_k^d$, define the distance from x to a line $l \in \mathcal{L}$ by:

$$d(x, \mathcal{L})_l = \inf_{y \in l} \|x - y\|_2. \tag{51}$$

This quantity is preserved under the action of $\mathrm{E}(d)$, meaning that any function constructed solely from the collection $\{d(x, \mathcal{L})_l\}_{l \in \mathcal{L}}$ will inherit $\mathrm{E}(d)$-invariance.

Based on this observation, invariant splitting maps is constructed by applying a post-processing function $\beta \colon \mathbb{R}^k \to \Delta_{k-1}$ to the vector of distances. The resulting splitting map,

$$\alpha(x, \mathcal{L})_l = \beta\left(\{d(x, \mathcal{L})_l\}_{l \in \mathcal{L}}\right), \tag{52}$$

is guaranteed to be $\mathrm{E}(d)$-invariant for any choice of continuous β. Empirically, effective performance in applications is achieved when β is taken to be the softmax function with a tunable scaling parameter $\xi > 0$. This yields the practical definition:

$$\alpha(x, \mathcal{L})_l = \text{softmax}\left(\{\xi \cdot d(x, \mathcal{L})_l\}_{l \in \mathcal{L}}\right), \tag{53}$$

which distributes weights across lines in $\mathcal{L}$ according to their proximity to x, while respecting the geometric symmetries of the Euclidean space.

Remark C.4. The concepts of equivariance and invariance are widely employed in machine learning to ensure model robustness under transformations that preserve the semantic or structural properties of the input. Such principles are foundational in the design of architectures that respect inherent symmetries within data. Applications of equivariant models span various domains, including equivariant graph neural networks [71, 19, 82], equivariant metanetworks [86, 78, 88, 36], parameter symmetry [30, 26, 85], and optimization [91], among others.

D Theoretical Proofs

To ensure completeness, we provide full derivations of the result, closely following the methodology of [42].

D.1 Proof for Proposition B.1

To ensure completeness, we provide full derivations of the result, closely following the methodology of [42].

Proof. We begin by proving the inequality $\mathrm{KT}(\hat{\mu}, \hat{\nu}) \leq \mathrm{ET}_{\lambda}(\mu, \nu)$. Let $\gamma \in \Pi_{\leq}(\mu, \nu)$ be any admissible partial transport plan, and define $\hat{\gamma}$ according to the expression in Equation (34). By

construction, $\hat{\gamma} \in \Gamma(\hat{\mu}, \hat{\nu})$. Then, evaluating the cost of $\hat{\gamma}$ under the extended transport objective yields:

$$\begin{aligned}\mathrm{KT}(\hat{\mu}, \hat{\nu}) &\leq \int_{\hat{\mathcal{T}} \times \hat{\mathcal{T}}} \hat{c}(x, y)\, \hat{\gamma}(dx, dy) \\ &= b \int_{\mathcal{T} \times \mathcal{T}} \left[d_{\mathcal{T}}(x, y) - \lambda \right] \gamma(dx, dy) \\ &\qquad + \int_{\mathcal{T}} w(x) \left[1 - f_1(x) \right] \mu(dx) + \int_{\mathcal{T}} w(x) \left[1 - f_2(x) \right] \nu(dx). \end{aligned} \tag{54}$$

Taking the infimum over all $\gamma \in \Pi_{\leq}(\mu, \nu)$ on the right-hand side implies:

$$\mathrm{KT}(\hat{\mu}, \hat{\nu}) \leq \mathrm{ET}_{\lambda}(\mu, \nu). \tag{55}$$

We now establish the reverse inequality, i.e., $\mathrm{KT}(\hat{\mu}, \hat{\nu}) \geq \mathrm{ET}_{\lambda}(\mu, \nu)$. Let $\hat{\gamma} \in \Gamma(\hat{\mu}, \hat{\nu})$ be any feasible coupling in the balanced OT problem, and let γ be its restriction to $\mathcal{T} \times \mathcal{T}$. Then, by [42, Lemma 3.2], we have $\gamma \in \Pi_{\leq}(\mu, \nu)$ and the decomposition in Equation (34) holds. We now compute the total cost of $\hat{\gamma}$ under $\hat{c}$:

$$\begin{aligned}\int_{\hat{\mathcal{T}} \times \hat{\mathcal{T}}} \hat{c}(x, y)\, \hat{\gamma}(dx, dy) &= b \int_{\mathcal{T} \times \mathcal{T}} \left[d_{\mathcal{T}}(x, y) - \lambda \right] \gamma(dx, dy) \\ &\qquad + \int_{\mathcal{T}} w(x) \left[1 - f_1(x) \right] \mu(dx) + \int_{\mathcal{T}} w(x) \left[1 - f_2(x) \right] \nu(dx) \\ &\geq \mathrm{ET}_{\lambda}(\mu, \nu). \end{aligned} \tag{56}$$

Taking the infimum over all admissible $\hat{\gamma} \in \Gamma(\hat{\mu}, \hat{\nu})$ yields the desired inequality:

$$\mathrm{KT}(\hat{\mu}, \hat{\nu}) \geq \mathrm{ET}_{\lambda}(\mu, \nu). \tag{57}$$

Combining both bounds, we conclude the equivalence:

$$\mathrm{KT}(\hat{\mu}, \hat{\nu}) = \mathrm{ET}_{\lambda}(\mu, \nu). \tag{58}$$

The correspondence between optimal couplings γ and $\hat{\gamma}$ follows directly from the construction and identities established above. □

D.2 Proof for Theorem B.2

To ensure completeness, we provide full derivations of the result, closely following the methodology of [42].

Proof. We begin by establishing the intermediate result:

$$\mathrm{ET}_{\lambda}(\mu, \nu) = \sup_{(u, v) \in \mathcal{K}} \left[\int_{\mathcal{T}} u(x)\, \mu(dx) + \int_{\mathcal{T}} v(x)\, \nu(dx) \right], \tag{59}$$

where the admissible set $\mathcal{K}$ is defined as

$$\begin{aligned}\mathcal{K} := \Bigg\{ (u, v) \in L^1(\mu) \times L^1(\nu) \;\Bigg|\; & u(x) \leq w(x), \quad \forall x \in \mathcal{T}, \\ & -b\lambda + \inf_{x \in \mathcal{T}} \left[b\, d_{\mathcal{T}}(x, y) - w(x) \right] \leq v(y) \leq w(y), \quad \forall y \in \mathcal{T}, \\ & u(x) + v(y) \leq b[d_{\mathcal{T}}(x, y) - \lambda], \quad \forall x, y \in \mathcal{T} \Bigg\}. \end{aligned}$$

This identity follows from the dual representation of $\mathrm{KT}(\hat{\mu}, \hat{\nu})$ via Proposition B.1 and [12, Corollary 2.6], which yields:

$$\begin{aligned}\mathrm{ET}_{\lambda}(\mu, \nu) &= \sup_{\substack{\hat{u} \in L^1(\hat{\mu}),\, \hat{v} \in L^1(\hat{\nu}) \\ \hat{u}(x) + \hat{v}(y) \leq \hat{c}(x, y)}} \left[\int_{\hat{\mathcal{T}}} \hat{u}(x)\, \hat{\mu}(dx) + \int_{\hat{\mathcal{T}}} \hat{v}(y)\, \hat{\nu}(dy) \right] \\ &=: I. \end{aligned} \tag{60}$$

We aim to show that this supremum I coincides with

$$J := \sup_{(u,v)\in\mathcal{K}} \left[\int_{\mathcal{T}} u(x)\,\mu(dx) + \int_{\mathcal{T}} v(x)\,\nu(dx) \right]. \tag{61}$$

To show $I \geq J$, let $(u, v) \in \mathcal{K}$. Extend these functions to $\hat{\mathcal{T}}$ by setting:

$$\hat{u}(x) := \begin{cases} u(x) & \text{if } x \in \mathcal{T}, \\ 0 & \text{if } x = \hat{s}, \end{cases} \quad \hat{v}(x) := \begin{cases} v(x) & \text{if } x \in \mathcal{T}, \\ 0 & \text{if } x = \hat{s}. \end{cases}$$

Since $(u, v) \in \mathcal{K}$, it follows directly from the definition of $\hat{c}$ that $\hat{u}(x) + \hat{v}(y) \leq \hat{c}(x, y)$ for all $x, y \in \hat{\mathcal{T}}$. Consequently:

$$\begin{aligned} I &\geq \int_{\hat{\mathcal{T}}} \hat{u}(x)\,\hat{\mu}(dx) + \int_{\hat{\mathcal{T}}} \hat{v}(x)\,\hat{\nu}(dx) \\ &= \int_{\mathcal{T}} u(x)\,\mu(dx) + \int_{\mathcal{T}} v(x)\,\nu(dx), \end{aligned} \tag{62}$$

which implies $I \geq J$.

To prove the reverse inequality $I \leq J$, let $(\hat{u}, \hat{v})$ be a maximizer for I. Without loss of generality, we can normalize $\hat{u}(\hat{s}) = 0$ by observing that replacing $(\hat{u}, \hat{v})$ with $(\hat{u} - \hat{u}(\hat{s}), \hat{v} + \hat{u}(\hat{s}))$ preserves admissibility and the objective value. Moreover, define:

$$v(y) := \inf_{x\in\hat{\mathcal{T}}} [\hat{c}(x, y) - \hat{u}(x)] \quad \forall y \in \hat{\mathcal{T}}. \tag{63}$$

Then $\hat{v}(y) \leq v(y)$, and $(\hat{u}, v)$ remains admissible and achieves the same supremum, so we may further assume $\hat{v}(y) = \inf_x[\hat{c}(x, y) - \hat{u}(x)]$ and $\hat{u}(\hat{s}) = 0$. In particular,

$$\hat{v}(\hat{s}) = \inf_{x\in\hat{\mathcal{T}}} [\hat{c}(x, \hat{s}) - \hat{u}(x)]\,. \tag{64}$$

To proceed, we define $w(\hat{s}) := 0$ and consider two cases based on the structure of $\hat{u}$ and $\hat{v}$.

Case 1. Suppose that

$$\inf_{x\in\hat{\mathcal{T}}} [w(x) - \hat{u}(x)] \geq 0. \tag{65}$$

In this case, observe that $\hat{u}(\hat{s}) = 0$ by assumption. Since

$$\hat{c}(\hat{s}, \hat{s}) - \hat{u}(\hat{s}) = 0 \quad \text{and} \quad \inf_{x\in\mathcal{T}} [\hat{c}(x, \hat{s}) - \hat{u}(x)] = \inf_{x\in\mathcal{T}} [w(x) - \hat{u}(x)] \geq 0,$$

we conclude that

$$\hat{v}(\hat{s}) = \inf_{x\in\hat{\mathcal{T}}} [\hat{c}(x, \hat{s}) - \hat{u}(x)] = 0. \tag{66}$$

Next, for all $y \in \hat{\mathcal{T}}$, we bound $\hat{v}(y)$ from above:

$$\hat{v}(y) = \inf_{x\in\hat{\mathcal{T}}} [\hat{c}(x, y) - \hat{u}(x)] \leq \hat{c}(\hat{s}, y) - \hat{u}(\hat{s}) = w(y), \tag{67}$$

where we have used $\hat{u}(\hat{s}) = 0$.

To lower-bound $\hat{v}(y)$ for $y \in \mathcal{T}$, note that $\hat{u}(x) \leq w(x)$ for all $x \in \mathcal{T}$, and $w(\hat{s}) = 0$. Therefore,

$$\begin{aligned} \hat{v}(y) &= \inf_{x\in\hat{\mathcal{T}}} [\hat{c}(x, y) - \hat{u}(x)] \\ &\geq \inf_{x\in\hat{\mathcal{T}}} [\hat{c}(x, y) - w(x)] \\ &= \inf_{x\in\mathcal{T}} [b(d_{\mathcal{T}}(x, y) - \lambda) - w(x)] \\ &= -b\lambda + \inf_{x\in\mathcal{T}} [b\,d_{\mathcal{T}}(x, y) - w(x)]\,. \end{aligned} \tag{68}$$

Combining both bounds, we find that $\hat{v}(y)$ satisfies all constraints in the definition of $\mathcal{K}$, and $\hat{u} \leq w$ holds by assumption. Hence, $(\hat{u}, \hat{v}) \in \mathcal{K}$. We now compute the dual objective:

$$\begin{aligned} I &= \int_{\hat{\mathcal{T}}} \hat{u}(x)\, \hat{\mu}(dx) + \int_{\hat{\mathcal{T}}} \hat{v}(x)\, \hat{\nu}(dx) \\ &= \int_{\mathcal{T}} \hat{u}(x)\, \mu(dx) + \int_{\mathcal{T}} \hat{v}(x)\, \nu(dx) + \hat{v}(\hat{s})\, \mu(\mathcal{T}) \\ &= \int_{\mathcal{T}} \hat{u}(x)\, \mu(dx) + \int_{\mathcal{T}} \hat{v}(x)\, \nu(dx) \qquad (69) \\ &\leq J. \qquad (70) \end{aligned}$$

Thus, under this case, the supremum I is bounded above by J, completing the proof for Case 1.

Case 2. Suppose now that

$$\inf_{x \in \hat{\mathcal{T}}} [w(x) - \hat{u}(x)] < 0. \qquad (71)$$

As in Case 1, we deduce that

$$\hat{v}(\hat{s}) = \inf_{x \in \mathcal{T}} [w(x) - \hat{u}(x)] < 0, \qquad (72)$$

and the dual objective becomes

$$I = \int_{\mathcal{T}} \hat{u}(x)\, \mu(dx) + \int_{\mathcal{T}} \hat{v}(x)\, \nu(dx) + \mu(\mathcal{T}) \cdot \inf_{\mathcal{T}} [w - \hat{u}]\,. \qquad (73)$$

Define a truncated version of $\hat{u}$ by setting:

$$\tilde{u}(x) := \min\{\hat{u}(x), w(x)\}. \qquad (74)$$

This ensures that $\tilde{u}(x) \leq w(x)$ and, since $\hat{u}(\hat{s}) = 0$, we also have $\tilde{u}(\hat{s}) = 0$. Furthermore, for all $x, y \in \hat{\mathcal{T}}$,

$$\tilde{u}(x) + \hat{v}(y) \leq \hat{c}(x, y), \qquad (75)$$

due to the pointwise minimum structure of $\tilde{u}$ and the feasibility of $(\hat{u}, \hat{v})$.

Since $\inf_{x \in \mathcal{T}} [w(x) - \hat{u}(x)] < 0$, there exists $x_0 \in \mathcal{T}$ such that $\hat{u}(x_0) > w(x_0)$. Thus, at x_0, we have $\tilde{u}(x_0) = w(x_0)$ and therefore

$$\inf_{\mathcal{T}} [w - \tilde{u}] \leq 0. \qquad (76)$$

On the other hand, since $\tilde{u}(x) \leq w(x)$ everywhere, it follows that

$$\inf_{\mathcal{T}} [w - \tilde{u}] = 0. \qquad (77)$$

We now rewrite the first two terms in Equation (73) as:

$$\begin{aligned} \int_{\mathcal{T}} \hat{u}(x)\, \mu(dx) + \mu(\mathcal{T}) \cdot \inf_{\mathcal{T}} [w - \hat{u}] &= \int_{\mathcal{T}} \tilde{u}(x)\, \mu(dx) + \int_{\{x : \hat{u}(x) > w(x)\}} [\hat{u}(x) - w(x)]\, \mu(dx) \\ &\quad + \mu(\mathcal{T}) \cdot \inf_{\mathcal{T}} [w - \hat{u}] \\ &\leq \int_{\mathcal{T}} \tilde{u}(x)\, \mu(dx). \qquad (78) \end{aligned}$$

Substituting this into Equation (73), we obtain the upper bound:

$$I \leq \int_{\mathcal{T}} \tilde{u}(x)\, \mu(dx) + \int_{\mathcal{T}} \hat{v}(x)\, \nu(dx). \qquad (79)$$

We now define a new function $\tilde{v} : \mathcal{T} \to \mathbb{R}$ by

$$\tilde{v}(y) := \inf_{x \in \hat{\mathcal{T}}} [\hat{c}(x, y) - \tilde{u}(x)]\,. \qquad (80)$$

By construction, $\tilde{v}(y) \geq \hat{v}(y)$ and for all $y \in \mathcal{T}$,

$$\tilde{v}(y) \leq \hat{c}(\hat{s}, y) - \tilde{u}(\hat{s}) = w(y). \tag{81}$$

Furthermore, using $\tilde{u}(x) \leq w(x)$ and the form of $\hat{c}$, we obtain a lower bound:

$$\begin{aligned}\tilde{v}(y) &= \inf_{x \in \hat{\mathcal{T}}} [\hat{c}(x, y) - \tilde{u}(x)] \\ &\geq \inf_{x \in \mathcal{T}} [b(d_{\mathcal{T}}(x, y) - \lambda) - w(x)] \\ &= -b\lambda + \inf_{x \in \mathcal{T}} [b\, d_{\mathcal{T}}(x, y) - w(x)]\,. \end{aligned} \tag{82}$$

Combining these, we find that $(\tilde{u}, \tilde{v}) \in \mathcal{K}$. Hence,

$$I \leq \int_{\mathcal{T}} \tilde{u}(x)\, \mu(dx) + \int_{\mathcal{T}} \tilde{v}(x)\, \nu(dx) \leq J. \tag{83}$$

This completes the analysis for Case 2 and thus confirms the desired equality:

$$\mathrm{ET}_\lambda(\mu, \nu) = \sup_{(u,v) \in \mathcal{K}} \left[\int_{\mathcal{T}} u(x)\, \mu(dx) + \int_{\mathcal{T}} v(x)\, \nu(dx) \right], \tag{84}$$

where

$$\mathcal{K} := \Big\{ (u, v) : u \leq w, \quad -b\lambda + \inf_{x \in \mathcal{T}} [b\, d_{\mathcal{T}}(x, y) - w(x)] \leq v(y) \leq w(y), \\ u(x) + v(y) \leq b(d_{\mathcal{T}}(x, y) - \lambda) \Big\}. \tag{85}$$

We are now ready to complete the proof of the theorem. Since the weight function w is b-Lipschitz, it satisfies the following inequality for all $x \in \mathcal{T}$:

$$-w(x) \leq \inf_{y \in \mathcal{T}} [b\, d_{\mathcal{T}}(x, y) - w(y)]\,. \tag{86}$$

Let $(u, v) \in \mathcal{K}$ be arbitrary. Define the following sequence of dual potentials via infimal convolutions:

$$v^*(x) := \inf_{y \in \mathcal{T}} \{b[d_{\mathcal{T}}(x, y) - \lambda] - v(y)\} = -b\lambda + \inf_{y \in \mathcal{T}} [b\, d_{\mathcal{T}}(x, y) - v(y)] \geq u(x), \tag{87}$$

$$v^{**}(y) := \inf_{x \in \mathcal{T}} \{b[d_{\mathcal{T}}(x, y) - \lambda] - v^*(x)\} = -b\lambda + \inf_{x \in \mathcal{T}} [b\, d_{\mathcal{T}}(x, y) - v^*(x)] \geq v(y). \tag{88}$$

Now, observe that the lower and upper bounds for v imply that

$$-b\lambda + \inf_{x \in \mathcal{T}} [b\, d_{\mathcal{T}}(x, y) - w(x)] \leq v(y) \leq w(y).$$

Using this together with Equation (86), we can derive pointwise bounds on v^* for any $x \in \mathcal{T}$:

$$v^*(x) \leq -b\lambda - v(x) \leq -\inf_{y \in \mathcal{T}} [b\, d_{\mathcal{T}}(x, y) - w(y)] \leq w(x), \tag{89}$$

$$v^*(x) \geq -b\lambda + \inf_{y \in \mathcal{T}} [b\, d_{\mathcal{T}}(x, y) - w(y)] \geq -b\lambda - w(x). \tag{90}$$

We now show that v^* is b-Lipschitz. Let $x_1, x_2 \in \mathcal{T}$ and fix an arbitrary $\varepsilon > 0$. By the definition of infimum, there exists $y_1 \in \mathcal{T}$ such that

$$b\, d_{\mathcal{T}}(x_1, y_1) - v(y_1) < v^*(x_1) + b\lambda + \varepsilon.$$

Then,

$$\begin{aligned} v^*(x_2) - v^*(x_1) &\leq b\, d_{\mathcal{T}}(x_2, y_1) - v(y_1) - [b\, d_{\mathcal{T}}(x_1, y_1) - v(y_1)] + \varepsilon \\ &= b\, [d_{\mathcal{T}}(x_2, y_1) - d_{\mathcal{T}}(x_1, y_1)] + \varepsilon \leq b\, d_{\mathcal{T}}(x_1, x_2) + \varepsilon. \end{aligned} \tag{91}$$

Since this holds for all $\varepsilon > 0$, we conclude that

$$v^*(x_2) - v^*(x_1) \leq b\, d_{\mathcal{T}}(x_1, x_2). \tag{92}$$

By symmetry, the reverse inequality also holds, so

$$|v^*(x_1) - v^*(x_2)| \leq b\, d_{\mathcal{T}}(x_1, x_2), \tag{93}$$

which confirms that v^* is b-Lipschitz.

Thus, v^* belongs to the following class of functions:

$$\mathbb{L}' := \{f \in C(\mathcal{T}) : -b\lambda - w(x) \leq f(x) \leq w(x), \quad |f(x) - f(y)| \leq b\, d_{\mathcal{T}}(x, y)\}\,. \tag{94}$$

This concludes the key regularity properties needed for the dual formulation.

We now establish the identity $v^{**} = -b\lambda - v^*$. To begin, note from the definition that:

$$v^{**}(y) = \inf_{x \in \mathcal{T}} [b(d_{\mathcal{T}}(x, y) - \lambda) - v^*(x)] \leq -b\lambda - v^*(y). \tag{95}$$

On the other hand, since v^* is b-Lipschitz, we have for all $x \in \mathcal{T}$:

$$-v^*(y) \leq b\, d_{\mathcal{T}}(x, y) - v^*(x),$$

which implies

$$-b\lambda - v^*(y) \leq \inf_{x \in \mathcal{T}} [b(d_{\mathcal{T}}(x, y) - \lambda) - v^*(x)] = v^{**}(y). \tag{96}$$

Combining both bounds, we conclude that

$$v^{**}(y) = -b\lambda - v^*(y). \tag{97}$$

Using this identity, we now bound the dual objective for any $(u, v) \in \mathcal{K}$:

$$\begin{aligned}\int_{\mathcal{T}} u(x)\, \mu(dx) + \int_{\mathcal{T}} v(x)\, \nu(dx) &\leq \int_{\mathcal{T}} v^*(x)\, \mu(dx) + \int_{\mathcal{T}} v^{**}(x)\, \nu(dx) \\ &= \int_{\mathcal{T}} v^*(x)\, \mu(dx) - \int_{\mathcal{T}} v^*(x)\, \nu(dx) - b\lambda\, \nu(\mathcal{T}) \\ &= -b\lambda\, \nu(\mathcal{T}) + \int_{\mathcal{T}} v^*(x)\, (d\mu - d\nu). \end{aligned} \tag{98}$$

Since $v^* \in \mathbb{L}'$ as shown earlier, we conclude:

$$\int_{\mathcal{T}} u(x)\, \mu(dx) + \int_{\mathcal{T}} v(x)\, \nu(dx) \leq -b\lambda\, \nu(\mathcal{T}) + \sup_{f \in \mathbb{L}'} \int_{\mathcal{T}} f(x)\, (d\mu - d\nu). \tag{99}$$

Using the variational characterization of $\mathrm{ET}_\lambda(\mu, \nu)$ (proved earlier), we deduce the upper bound:

$$\mathrm{ET}_\lambda(\mu, \nu) \leq -b\lambda\, \nu(\mathcal{T}) + \sup_{f \in \mathbb{L}'} \int_{\mathcal{T}} f(x)\, (d\mu - d\nu). \tag{100}$$

To prove the reverse inequality, let $f \in \mathbb{L}'$ and define:

$$u := f, \qquad v := -b\lambda - f.$$

Then:

$$u(x) \leq w(x), \quad v(x) \leq -b\lambda - (-b\lambda - w(x)) = w(x),$$

and

$$\begin{aligned} v(x) &= -b\lambda - f(x) \geq -b\lambda - w(x) \\ &\geq -b\lambda + \inf_{y \in \mathcal{T}} [b\, d_{\mathcal{T}}(x, y) - w(y)]\,. \end{aligned} \tag{101}$$

Moreover, the b-Lipschitz property of f yields:

$$u(x) + v(y) = f(x) - f(y) - b\lambda \leq b\, (d_{\mathcal{T}}(x, y) - \lambda), \tag{102}$$

which confirms that $(u, v) \in \mathcal{K}$. Applying the variational formula for ET_λ, we obtain:

$$-b\lambda\, \nu(\mathcal{T}) + \int_{\mathcal{T}} f(x)\, (d\mu - d\nu) = \int_{\mathcal{T}} u(x)\, \mu(dx) + \int_{\mathcal{T}} v(x)\, \nu(dx) \leq \mathrm{ET}_\lambda(\mu, \nu). \tag{103}$$

Since this holds for all $f \in \mathbb{L}'$, we deduce:

$$-b\lambda\,\nu(\mathcal{T}) + \sup_{f\in\mathbb{L}'} \int_{\mathcal{T}} f(x)\,(d\mu - d\nu) \le \mathrm{ET}_\lambda(\mu,\nu). \tag{104}$$

Putting both directions together, we conclude:

$$\mathrm{ET}_\lambda(\mu,\nu) = -b\lambda\,\nu(\mathcal{T}) + \sup_{f\in\mathbb{L}'} \int_{\mathcal{T}} f(x)\,(d\mu - d\nu). \tag{105}$$

To recover the symmetric form in Theorem B.2, let $f = \tilde{f} - \frac{b\lambda}{2}$. Then, $f \in \mathbb{L}'$ if and only if $\tilde{f} \in \mathbb{L}$. Furthermore:

$$\int_{\mathcal{T}} f(x)\,(d\mu - d\nu) = \int_{\mathcal{T}} \left(\tilde{f}(x) - \frac{b\lambda}{2}\right)\,(d\mu - d\nu) = \int_{\mathcal{T}} \tilde{f}(x)\,(d\mu - d\nu) - \frac{b\lambda}{2}\left[\mu(\mathcal{T}) - \nu(\mathcal{T})\right]. \tag{106}$$

Substituting into Equation (105), we obtain the final expression:

$$\mathrm{ET}_\lambda(\mu,\nu) = \sup_{f\in\mathbb{L}} \int_{\mathcal{T}} f(x)\,(d\mu - d\nu) - \frac{b\lambda}{2}\left[\mu(\mathcal{T}) + \nu(\mathcal{T})\right], \tag{107}$$

which completes the proof. □

D.3 Proof for Proposition B.3

To ensure completeness, we provide full derivations of the result, closely following the methodology of [42].

Proof. We begin by expanding the definition of the regularized entropy transport:

$$\begin{aligned}\widetilde{\mathrm{ET}}^{a}_{\lambda}(\mu,\nu) = &-\frac{b\lambda}{2}\left[\mu(\mathcal{T}) + \nu(\mathcal{T})\right] \\ &+ \sup\left\{ s\cdot\left[\mu(\mathcal{T}) - \nu(\mathcal{T})\right] :\, s \in \left[-\frac{b\lambda}{2} - w(r) + a,\; w(r) + \frac{b\lambda}{2} - a\right]\right\} \\ &+ \sup\left\{ \int_{\mathcal{T}} \left(\int_{[r,x]} g(y)\,\omega(dy)\right)(\mu-\nu)(dx) :\, \|g\|_{L^\infty(\mathcal{T})} \le b\right\}.\end{aligned} \tag{108}$$

We now evaluate each supremum separately:

- The first supremum corresponds to maximizing a linear function over a symmetric interval. Therefore, it evaluates to

$$\left[w(r) + \frac{b\lambda}{2} - a\right]\cdot|\mu(\mathcal{T}) - \nu(\mathcal{T})|. \tag{109}$$

- The second supremum is equivalent to the dual representation of a Lipschitz-type transport energy over tree-structured domains. As established in [21, pp. 575–576], we have:

$$\sup\left\{ \int_{\mathcal{T}} \left(\int_{[r,x]} g(y)\,\omega(dy)\right)(\mu-\nu)(dx) :\, \|g\|_{L^\infty(\mathcal{T})} \le b\right\} = \int_{\mathcal{T}} |\mu(\Lambda(x)) - \nu(\Lambda(x))|\,\omega(dx). \tag{110}$$

Combining both components, we obtain the closed-form expression:

$$\begin{aligned}\widetilde{\mathrm{ET}}^{a}_{\lambda}(\mu,\nu) = &\int_{\mathcal{T}} |\mu(\Lambda(x)) - \nu(\Lambda(x))|\,\omega(dx) - \frac{b\lambda}{2}\left[\mu(\mathcal{T}) + \nu(\mathcal{T})\right] \\ &+ \left[w(r) + \frac{b\lambda}{2} - a\right]\cdot|\mu(\mathcal{T}) - \nu(\mathcal{T})|.\end{aligned} \tag{111}$$

This concludes the proof. □

D.4 Proof for Proposition B.4

To ensure completeness, we provide full derivations of the result, closely following the methodology of [42].

Proof. We begin with the upper bound $\mathrm{ET}_\lambda(\mu,\nu) \le \widetilde{\mathrm{ET}}^0_\lambda(\mu,\nu)$. This follows directly from the inclusion $\mathbb{L} \subset \mathbb{L}_0$ and the dual representation of ET_λ established in Theorem B.2.

Next, consider a satisfying

$$2bL(\mathcal{T}) \le a \le \frac{b\lambda}{2} + w(r). \tag{112}$$

We will show that under this condition, the inclusion $\mathbb{L}_a \subset \mathbb{L}$ holds. Then, by Theorem B.2, it follows that

$$\widetilde{\mathrm{ET}}^a_\lambda(\mu,\nu) \le \mathrm{ET}_\lambda(\mu,\nu). \tag{113}$$

To prove $\mathbb{L}_a \subset \mathbb{L}$, we need to show that any function $f \in \mathbb{L}_a$ satisfies

$$-w(x) - \frac{b\lambda}{2} \le f(x) \le w(x) + \frac{b\lambda}{2}, \quad \forall x \in \mathcal{T}. \tag{114}$$

Let $f \in \mathbb{L}_a$. Then by definition,

$$f(x) = s + \int_{[r,x]} g(y)\,\omega(dy), \tag{115}$$

where $s \in \left[-w(r) - \frac{b\lambda}{2} + a,\ w(r) + \frac{b\lambda}{2} - a\right]$ and $\|g\|_{L^\infty(\mathcal{T})} \le b$. Using this, we bound $f(x)$ from above:

$$\begin{aligned} f(x) &\le s + \|g\|_{L^\infty(\mathcal{T})} \cdot \omega([r,x]) \\ &\le w(r) + \frac{b\lambda}{2} - a + bL(\mathcal{T}) \\ &\le w(x) + \frac{b\lambda}{2} - a + 2bL(\mathcal{T}) \\ &\le w(x) + \frac{b\lambda}{2}. \end{aligned} \tag{116}$$

For the lower bound, we have:

$$\begin{aligned} f(x) &\ge s - \|g\|_{L^\infty(\mathcal{T})} \cdot \omega([r,x]) \\ &\ge -w(r) - \frac{b\lambda}{2} + a - bL(\mathcal{T}) \\ &\ge -w(x) - \frac{b\lambda}{2} + a - 2bL(\mathcal{T}) \\ &\ge -w(x) - \frac{b\lambda}{2}. \end{aligned} \tag{117}$$

Hence, f satisfies the defining constraints of $\mathbb{L}$ and we conclude that $f \in \mathbb{L}$. Therefore, $\mathbb{L}_a \subset \mathbb{L}$ for all $a \ge 2bL(\mathcal{T})$.

It follows from Theorem B.2 and the definition of $\widetilde{\mathrm{ET}}^a_\lambda$ that

$$\widetilde{\mathrm{ET}}^a_\lambda(\mu,\nu) \le \mathrm{ET}_\lambda(\mu,\nu). \tag{118}$$

This concludes the proof. □

D.5 Proof for Proposition B.5

To ensure completeness, we provide full derivations of the result, closely following the methodology of [42].

Proof. We first observe that the metric d_a depends solely on the value of the weight function at the root r of the tree $\mathcal{T}$. This follows directly from the definition of $\mathbb{L}_a$, where only $w(r)$ appears explicitly.

By construction, we have the variational characterization:

$$d_a(\mu,\nu) = \sup\left\{\int_{\mathcal{T}} f\,(d\mu - d\nu) : f \in \mathbb{L}_a\right\}. \tag{119}$$

Let us now verify the metric properties:

(Non-negativity) Clearly, $d_a(\mu,\nu) \geq 0$ from the supremum structure. Moreover, $d_a(\mu,\mu) = 0$ for all μ by linearity of the integral. Now suppose that $d_a(\mu,\nu) = 0$. Using the closed-form expression for $\widetilde{\mathrm{ET}}^a_\lambda$ in Proposition B.3, this implies:

$$\left[w(r) + \frac{b\lambda}{2} - a\right] \cdot |\mu(\mathcal{T}) - \nu(\mathcal{T})| + \int_{\mathcal{T}} |\mu(\Lambda(x)) - \nu(\Lambda(x))|\ \omega(dx) = 0. \tag{120}$$

Since the first term has a strictly positive coefficient by assumption ($a < w(r) + \frac{b\lambda}{2}$), we must have $\mu(\mathcal{T}) = \nu(\mathcal{T})$ and

$$\mu(\Lambda(x)) = \nu(\Lambda(x)) \quad \text{for all } x \in \mathcal{T}. \tag{121}$$

By [42, Lemma A.2], this implies that $\mu = \nu$, establishing identity of indiscernibles.

(Symmetry) Note that if $f \in \mathbb{L}_a$, then $-f \in \mathbb{L}_a$ by the symmetric definition of the function class. Therefore, from Equation (119), we obtain

$$d_a(\mu,\nu) = d_a(\nu,\mu). \tag{122}$$

(Triangle Inequality) The triangle inequality holds immediately from the supremum definition over a convex, symmetric function class:

$$d_a(\mu,\sigma) + d_a(\sigma,\nu) \geq \int_{\mathcal{T}} f\,(d\mu - d\sigma) + \int_{\mathcal{T}} f\,(d\sigma - d\nu) = \int_{\mathcal{T}} f\,(d\mu - d\nu), \tag{123}$$

for all $f \in \mathbb{L}_a$, and taking the supremum yields the inequality.

Hence, d_a satisfies all properties of a metric on $\mathcal{M}(\mathcal{T})$, and the proof is complete. □

D.6 Proof for Equation (13)

Proof. We recall Equation (13). Let $f \in L^1(\mathbb{R}^d)$ be a non-negative density function. The Radon Transform $\mathcal{R}^\alpha$ maps f to a density defined on a tree system $\mathcal{T}$, while preserving the total mass:

$$\|f\|_1 = \int_{\mathbb{R}^d} f(x)\,dx = \|\mathcal{R}^\alpha_{\mathcal{T}} f\|_{\mathcal{T}}, \quad \text{for all} \quad \mathcal{T} \in \mathbb{T}. \tag{124}$$

To establish this property, we first observe that the non-negativity of α ensures that the transform preserves non-negativity: if $f \geq 0$, then $\mathcal{R}^\alpha_{\mathcal{T}} f \geq 0$, implying that the transformed function is a valid density. The preservation of total mass then follows directly from the definition of $\mathcal{R}^\alpha$, which integrates over linearly parameterized subsets aligned with the structure of $\mathcal{T}$.

$$\begin{aligned}
\|\mathcal{R}^\alpha_{\mathcal{T}} f\|_{\mathcal{T}} &= \sum_{l\in\mathcal{T}} \int_{\mathbb{R}} |\mathcal{R}^\alpha_{\mathcal{T}} f(t_x, l)|\ dt_x \\
&= \sum_{l\in\mathcal{L}} \int_{\mathbb{R}} \left| \int_{\mathbb{R}^d} f(y)\cdot \alpha(y,\mathcal{L})_l \cdot \delta\left(t_x - \langle y - x_l, \theta_l\rangle\right)\ dy \right| dt_x \\
&= \sum_{l\in\mathcal{L}} \int_{\mathbb{R}} \left(\int_{\mathbb{R}^d} f(y)\cdot \alpha(y,\mathcal{L})_l \cdot \delta\left(t_x - \langle y - x_l, \theta_l\rangle\right)\ dy \right) dt_x \\
&= \sum_{l\in\mathcal{L}} \int_{\mathbb{R}^d} \left(\int_{\mathbb{R}} f(y)\cdot \alpha(y,\mathcal{L})_l \cdot \delta\left(t_x - \langle y - x_l, \theta_l\rangle\right)\ dt_x \right) dy
\end{aligned}$$

$$
\begin{aligned}
&= \sum_{l\in\mathcal{L}} \int_{\mathbb{R}^d} f(y)\cdot\alpha(y,\mathcal{L})_l \cdot \left(\int_{\mathbb{R}} \delta\left(t_x - \langle y - x_l, \theta_l\rangle\right)\, dt_x\right) dy \\
&= \sum_{l\in\mathcal{L}} \int_{\mathbb{R}^d} f(y)\cdot\alpha(y,\mathcal{L})_l \, dy \\
&= \int_{\mathbb{R}^d} f(y)\cdot \sum_{l\in\mathcal{L}} \alpha(y,\mathcal{L})_l \, dy \\
&= \int_{\mathbb{R}^d} f(y)\, dy \\
&= \|f\|_1. \qquad (125)
\end{aligned}
$$

The proof is completed. □

D.7 Proof for Theorem 3.3

Proof. We consider the expression

$$
\text{PartialTSW}(\mu,\nu) = \int_{\mathbb{T}} d_a(\mu_{\mathcal{T}},\nu_{\mathcal{T}})\, d\sigma(\mathcal{T}), \qquad (126)
$$

and show that it defines a metric on $\mathcal{M}(\mathbb{R}^d)$. Since the splitting map α is $\mathrm{E}(d)$-invariant, the Radon Transform $\mathcal{R}^\alpha$ is injective; that is, for any $f \in L^1(\mathbb{R}^d)$, if $\mathcal{R}^\alpha_{\mathcal{T}} f = 0$ for all $\mathcal{T} \in \mathbb{T}$, then $f = 0$ (see [80]). We now verify the three properties required for PartialTSW to be a metric on $\mathcal{M}(\mathbb{R}^d)$.

Positive definiteness. For $\mu,\nu \in \mathcal{P}(\mathbb{R}^n)$, it is clear that $\text{PartialTSW}(\mu,\mu) = 0$ and $\text{PartialTSW}(\mu,\nu) \geq 0$. Moreover, if $\text{PartialTSW}(\mu,\nu) = 0$, then $d_a(\mu_{\mathcal{T}},\nu_{\mathcal{T}}) = 0$ for all $\mathcal{T} \in \mathbb{T}$. Since d_a is a metric on $\mathcal{M}(\mathcal{T})$, it follows that $\mu_{\mathcal{T}} = \nu_{\mathcal{T}}$ for all $\mathcal{T}$. Hence, $\mathcal{R}^\alpha_{\mathcal{T}} f_\mu = \mathcal{R}^\alpha_{\mathcal{T}} f_\nu$ for all $\mathcal{T} \in \mathbb{T}$. By the injectivity of $\mathcal{R}^\alpha$, we conclude that $f_\mu = f_\nu$, and thus $\mu = \nu$.

Symmetry. For any $\mu,\nu \in \mathcal{M}(\mathbb{R}^n)$, we have:

$$
\begin{aligned}
\text{PartialTSW}(\mu,\nu) &= \int_{\mathbb{T}} d_a(\mu_{\mathcal{T}},\nu_{\mathcal{T}})\, d\sigma(\mathcal{T}) \\
&= \int_{\mathbb{T}} d_a(\nu_{\mathcal{T}},\mu_{\mathcal{T}})\, d\sigma(\mathcal{T}) \qquad (127) \\
&= \text{PartialTSW}(\nu,\mu). \qquad (128)
\end{aligned}
$$

Therefore, $\text{PartialTSW}(\mu,\nu) = \text{PartialTSW}(\nu,\mu)$.

Triangle inequality. For $\mu_1,\mu_2,\mu_3 \in \mathcal{M}(\mathbb{R}^n)$, we compute:

$$
\begin{aligned}
&\text{PartialTSW}(\mu_1,\mu_2) + \text{PartialTSW}(\mu_2,\mu_3) \\
&= \int_{\mathbb{T}} d_a(\mu_{1,\mathcal{T}},\mu_{2,\mathcal{T}})\, d\sigma(\mathcal{T}) + \int_{\mathbb{T}} d_a(\mu_{2,\mathcal{T}},\mu_{3,\mathcal{T}})\, d\sigma(\mathcal{T}) \\
&= \int_{\mathbb{T}} \left(d_a(\mu_{1,\mathcal{T}},\mu_{2,\mathcal{T}}) + d_a(\mu_{2,\mathcal{T}},\mu_{3,\mathcal{T}})\right)\, d\sigma(\mathcal{T}) \\
&\geq \int_{\mathbb{T}} d_a(\mu_{1,\mathcal{T}},\mu_{3,\mathcal{T}})\, d\sigma(\mathcal{T}) \\
&= \text{PartialTSW}(\mu_1,\mu_3), \qquad (129)
\end{aligned}
$$

where the inequality follows from the triangle inequality satisfied by d_a on each tree $\mathcal{T}$.

In conclusion, PartialTSW satisfies all properties of a metric on the space $\mathcal{M}(\mathbb{R}^d)$.

We aim to show that PartialTSW is $\mathrm{E}(d)$-invariant, meaning that for any $g \in \mathrm{E}(d)$, the following holds:

$$
\text{PartialTSW}(\mu,\nu) = \text{PartialTSW}(g\sharp\mu, g\sharp\nu), \qquad (130)
$$

where $g\sharp\mu$ and $g\sharp\nu$ denote the pushforwards of μ and ν, respectively, under the Euclidean transformation $g\colon \mathbb{R}^d \to \mathbb{R}^d$.

Let $\mathcal{T} \in \mathbb{T}$ be a tree system given by $\mathcal{T} = \{l_i = (x_i, \theta_i)\}_{i=1}^k$. Then, under the action of $g = (Q, a)$, we have

$$g\mathcal{T} = \{gl_i = (Qx_i + a, Q\theta_i)\}_{i=1}^k. \tag{131}$$

We also note that $g\sharp f_\mu = f_{g\sharp\mu}$ and $g\sharp f_\nu = f_{g\sharp\nu}$. Since $|\det(Q)| = 1$, we compute:

$$\begin{aligned}
\mathcal{R}^\alpha_{g\mathcal{L}}(g\sharp f_\mu)(gx, gl) &= \int_{\mathbb{R}^d} (g\sharp f_\mu)(y) \cdot \alpha(y, g\mathcal{L})_l \cdot \delta\left(t_{gx} - \langle y - x_{gl}, \theta_{gl}\rangle\right)\, dy \\
&= \int_{\mathbb{R}^d} f_\mu(g^{-1}y) \cdot \alpha(y, g\mathcal{L})_l \cdot \delta\left(t_x - \langle y - x_{gl}, \theta_{gl}\rangle\right)\, dy \\
&= \int_{\mathbb{R}^d} f_\mu(g^{-1}gy) \cdot \alpha(gy, g\mathcal{L})_l \cdot \delta\left(t_x - \langle gy - x_{gl}, \theta_{gl}\rangle\right)\, d(gy) \\
&= \int_{\mathbb{R}^d} f_\mu(y) \cdot \alpha(y, \mathcal{L})_l \cdot \delta\left(t_x - \langle gy - x_{gl}, \theta_{gl}\rangle\right)\, dy \\
&= \int_{\mathbb{R}^d} f_\mu(y) \cdot \alpha(y, \mathcal{L})_l \cdot \delta\left(t_x - \langle Qy + a - Qx_l - a, Q\theta_l\rangle\right)\, dy \\
&= \int_{\mathbb{R}^d} f_\mu(y) \cdot \alpha(y, \mathcal{L})_l \cdot \delta\left(t_x - \langle Q(y - x_l), Q\theta_l\rangle\right)\, dy \\
&= \int_{\mathbb{R}^d} f_\mu(y) \cdot \alpha(y, \mathcal{L})_l \cdot \delta\left(t_x - \langle y - x_l, \theta_l\rangle\right)\, dy \\
&= \mathcal{R}^\alpha_{\mathcal{L}} f_\mu(x, l).
\end{aligned} \tag{132}$$

A similar computation gives:

$$\mathcal{R}^\alpha_{g\mathcal{L}}(g\sharp f_\nu)(gx, gl) = \mathcal{R}^\alpha_{\mathcal{L}} f_\nu(x, l). \tag{133}$$

Moreover, since g acts isometrically on tree systems, the induced measures satisfy:

$$d_a(\mu_\mathcal{T}, \nu_\mathcal{T}) = d_a((g\sharp\mu)_{g\mathcal{T}}, (g\sharp\nu)_{g\mathcal{T}}). \tag{134}$$

Thus, we compute:

$$\begin{aligned}
\text{PartialTSW}(g\sharp\mu, g\sharp\nu) &= \int_{\mathbb{T}} d_a((g\sharp\mu)_\mathcal{T}, (g\sharp\nu)_\mathcal{T})\, d\sigma(\mathcal{T}) \\
&= \int_{\mathbb{T}} d_a((g\sharp\mu)_{g\mathcal{T}}, (g\sharp\nu)_{g\mathcal{T}})\, d\sigma(g\mathcal{T}) \\
&= \int_{\mathbb{T}} d_a(\mu_\mathcal{T}, \nu_\mathcal{T})\, d\sigma(g\mathcal{T}) \\
&= \int_{\mathbb{T}} d_a(\mu_\mathcal{T}, \nu_\mathcal{T})\, d\sigma(\mathcal{T}) \\
&= \text{PartialTSW}(\mu, \nu).
\end{aligned} \tag{135}$$

We conclude that PartialTSW is $\mathrm{E}(d)$-invariant. □

Remark D.1. We omit almost-sure conditions in the above proof, as they are straightforward to verify and would otherwise obscure the main argument.

E Experimental Details

E.1 Algorithm for Partial Tree-Sliced Wasserstein Distance

The computation of the Partial Tree-Sliced Wasserstein (PartialTSW) distance is outlined in Algorithm 1. This procedure estimates the distance by averaging costs derived from multiple tree-based projections of the input measures.

Algorithm 1 Partial Tree-Sliced Wasserstein distance.

Input: Measures μ and ν in $\mathcal{M}(\mathbb{R}^d)$, number of tree systems L, number of lines in tree system k, space of tree systems $\mathbb{T}$, splitting maps α, parameters a, b, λ, total mass $\mu(\mathcal{T})$, $\nu(\mathcal{T})$.
Scale total mass of μ and ν such that $\mu(\mathbb{R}^d) = \mu(\mathcal{T})$, $\nu(\mathbb{R}^d) = \nu(\mathcal{T})$.
for $i = 1$ to L **do**
  Sampling $x \in \mathbb{R}^d$ and $\theta_1, \ldots, \theta_k \overset{i.i.d}{\sim} \mathcal{U}(\mathbb{S}^{d_\theta - 1})$.
  Contruct tree system $\mathcal{L}_i = \{(x, \theta_1), \ldots, (x, \theta_k)\}$.
  Projecting μ and ν onto $\mathcal{T}_i$ to get $\mathcal{R}^\alpha_{\mathcal{L}_i}\mu$ and $\mathcal{R}^\alpha_{\mathcal{L}_i}\nu$.
  Compute $\widehat{\text{PartialTSW}}(\mu, \nu) = (1/L) \cdot d_a(\mathcal{R}^\alpha_{\mathcal{L}_i}\mu, \mathcal{R}^\alpha_{\mathcal{L}_i}\nu)$.
end for
Return: $\widehat{\text{PartialTSW}}(\mu, \nu)$.

E.2 Computational and Memory Complexity Analysis

This section details the computational and memory demands of our proposed PartialTSW distance. We consider input measures μ and ν represented by N samples in a d-dimensional space, with L tree constructions and k lines per tree.

Table 3 outlines the complexity of key operations. The dominant factors are the distance-based weight splitting ($\mathcal{O}(LkNd)$) for projecting samples and the sorting of these projected 1D coordinates ($\mathcal{O}(LkN \log N)$). Consequently, the total computational complexity is $\mathcal{O}(LkNd + LkN \log N)$. The primary memory consumers are the storage of split weights, tree/line parameters, and the original data, leading to an overall memory requirement of $\mathcal{O}(LkN + Lkd + Nd)$.

Table 3: Detailed complexity analysis for PartialTSW. (N = number of samples, d = dimension, L = number of trees, k = lines per tree).

Operation Category	**Specific Steps Involved**	**Computational Cost**	**Memory Cost**
Initial Mass Scaling	Adjusting sample weights for μ and ν to meet target total masses.	$O(N)$	$O(N)$
Distance-Based Weight Splitting	Calculation of distances from N points to Lk lines, and subsequent softmax for weight distribution.	$\mathcal{O}(LkNd)$	$\mathcal{O}(LkN + Lkd + Nd)$
Sorting Projected Data	Sorting the N projected coordinates along each of the Lk lines.	$\mathcal{O}(LkN \log N)$	$\mathcal{O}(LkN)$
Overall Total		$\mathcal{O}(LkNd + LkN \log N)$	$\mathcal{O}(LkN + Lkd + Nd)$

GPU Memory Optimization for Distance-Based Splitting. The practical GPU memory footprint for the distance-based splitting step can be significantly lower than a naive theoretical estimate. As highlighted by [80], this operation involves (1) computing d-dimensional distance vectors from points to lines, (2) calculating their norms, and (3) applying a softmax function across lines within each tree to obtain split weights. While a direct implementation might suggest $\mathcal{O}(LkNd)$ memory for storing all intermediate distance vectors, modern deep learning frameworks like PyTorch, when using compilation tools (e.g., 'torch.compile'), can perform kernel fusion. This optimization merges these sequential computations into fewer GPU kernels, potentially allowing large intermediate tensors (like the full $LkN \times d$ distance vectors) to reside in faster, smaller shared memory or be recomputed on-the-fly, rather than occupying global GPU memory. Consequently, the persistent global memory primarily stores the essential data: line parameters ($\mathcal{O}(Lkd)$), sample coordinates ($\mathcal{O}(Nd)$), and the resulting split weights ($\mathcal{O}(LkN)$), aligning with the $\mathcal{O}(LkN + Lkd + Nd)$ overall memory profile.

E.3 Empirical Runtime and Memory Performance of PartialTSW

We present an empirical evaluation of the runtime and memory usage of PartialTSW. The experiments were conducted on a single NVIDIA H100 GPU. We fixed the number of tree iterations $L = 10$ and lines per tree $k = 4$. The analysis varies the number of samples $N \in \{100, 1K, 5K, 10K, 500K\}$ and the data dimension $d \in \{50, 100, 500, 1000\}$.

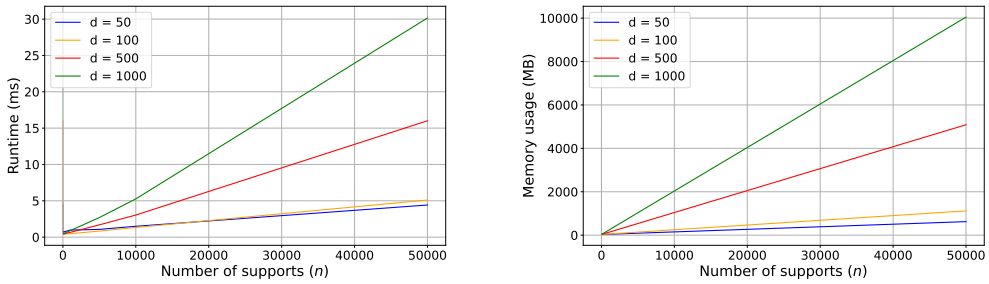

Figure 7: Empirical runtime (left) and peak memory usage (right) for PartialTSW, varying the number of samples (N) and data dimension (d). ($L = 10, k = 4$).

Runtime Scalability. The empirical results, depicted in Figure 7 (left), illustrate how the runtime of PartialTSW scales with the number of samples N and the data dimension d. The runtime exhibits a near-linear increase with N. For instance, processing $N = 50,000$ samples takes approximately five times longer than $N = 10,000$ samples (when d, L, k are fixed), which is consistent with the $\mathcal{O}(Nd + N \log N)$ dependency on N from our theoretical analysis (Section E.2). Regarding dimensionality, the runtime also demonstrates a linear dependency on d. For example, increasing d from 10000 to 50000 (a 5x increase) results in a correspondingly proportional increase in runtime for a fixed N. This aligns with the $\mathcal{O}(d)$ factor in the $LkNd$ term of the complexity. These empirical observations support the theoretical computational complexity.

Memory Scalability. Figure 7 (right) showcases the memory consumption characteristics of PartialTSW. The peak memory usage scales linearly with both the number of samples N and the dimension d. This behavior is predictable and directly corresponds to our theoretical memory complexity of $\mathcal{O}(LkN + Lkd + Nd)$, indicating efficient memory utilization that grows manageably with data size and dimensionality.

E.4 Sample Complexity and Estimator Stability

We first clarify the roles of the two key parameters in our method.

- Lines per Tree (k): This is a *structural parameter* that defines the ground-truth distance $\text{PartialTSW}_k(\mu, \nu)$. As discussed in the TSW literature, using $k > 1$ enhances the method's capacity to capture complex topological and structural features of the data.
- Number of Trees (L): This is the *Monte Carlo (MC) estimation parameter*. Our method approximates the ground-truth distance by averaging over L independently sampled random trees.

As discussed in the computational complexity analysis in Section 3.3, the total computational cost is proportional to the total number of 1D projections, which is $N = Lk$. For a fixed computational budget N, this creates a natural trade-off: increasing k improves topological expressiveness, but requires decreasing L, which in turn affects the stability of the MC estimate.

In our experiments, we tune the structural parameter k for empirical performance and then set $L = N/k$ to ensure the total number of projections N remains fixed, allowing for a fair comparison against baselines under the same computational budget.

This approach raises a valid concern about the stability of the estimator, as the MC approximation error for a fixed k decreases at a rate of $\mathcal{O}(L^{-1/2})$. We therefore provide an empirical analysis of the estimator's convergence. We measure stability using the Coefficient of Variation (CoV = σ/μ), a normalized metric where σ is the standard deviation and μ is the mean of the distance estimate over multiple runs.

Table 4 shows the CoV as a function of both the MC parameter L and the structural parameter k. The results empirically verify the expected convergence. For any fixed k, the estimator's stability improves (i.e., CoV decreases) as the number of MC samples L increases, aligning with the theoretical $\mathcal{O}(L^{-1/2})$ rate. For instance, at $k = 5$, increasing L from 10 to 1000 reduces the CoV by over 14×.

Table 4: Estimator stability analysis. The table shows the Coefficient of Variation (CoV = σ/μ) for the PartialTSW distance as a function of the number of tree slices (L) and the number of lines per tree (k).

Number of Trees (L)	$k = 5$	$k = 10$	$k = 100$
10	0.1098	0.1016	0.0456
50	0.0526	0.0252	0.0183
100	0.0263	0.0239	0.0091
500	0.0105	0.0133	0.0070
1000	0.0076	0.0070	0.0041
10000	0.0029	0.0018	0.0023
20000	0.0016	0.0024	0.0010

This analysis confirms that in our large-scale experiments, where we use a high number of projections (e.g., $L \geq 1000$), the resulting distance estimate is stable and reliable.

E.5 Discussion on Hyperparameters of Evaluated Methods

This section briefly outlines the key hyper-parameters for each evaluated Unbalanced Optimal Transport (UOT) and Partial Optimal Transport (POT) method and their respective roles.

SPOT [9]. The hyperparameter k specifies the number of points to be transported, thereby defining the partial nature of the matching between distributions.

SOPT [2]. The regularization parameter λ controls the "partialness" of the transport by influencing the total amount of mass that is optimally transported between distributions.

Sinkhorn [74]. The hyperparameter reg is the entropic regularization coefficient that smooths the optimal transport plan. The hyperparameter reg_m is the marginal regularization coefficient that penalizes deviations from the prescribed marginal constraints, thus allowing for mass variation.

SUOT and USOT [7]. The hyper-parameters ρ_1 and ρ_2 are regularization parameters. They respectively control the cost of deviating from the source and target marginals in the sliced domain, enabling unbalanced transport by permitting mass creation or destruction.

PAWL [13]. The hyperparameter k the number of points to be transported, effectively determining the extent of partiality in this unbalanced optimal transport formulation.

UOT-FM [22]. The hyperparameter λ influences the regularization of marginal constraints, thereby controlling the degree to which the masses of the coupled distributions must be preserved during transport.

ULightOT [28]. The hyperparameter τ governs the extent of mass conservation, adjusting how strictly the total mass of the transported distribution must adhere to the original or target masses.

Partial-TSW (Ours). The mass parameter $\nu(\mathcal{T})$ specifies the proportion of the target distribution's mass to be matched by the transport plan. The source distribution's mass proportion, $\mu(\mathcal{T})$, is typically fixed at 1, so adjusting $\nu(\mathcal{T})$ controls the partiality of the matching against the target.

E.6 Comparing Computational Efficiency

To ensure consistent and fair results, two warm-up runs were performed for each method and each sample size n before conducting 10 timed repetitions. The average runtime and peak memory usage (for GPU methods) were then recorded. Unless otherwise specified (as in the discussion on varying d below), these experiments were conducted with data of dimension $d = 2$ and for sample sizes n ranging from 10^2 to 10^5.

Since hyperparameter choices can significantly affect algorithmic runtime, the specific settings used for each method in this runtime comparison are detailed below. For a general description of these hyperparameters and their roles, please refer to Appendix §E.5.

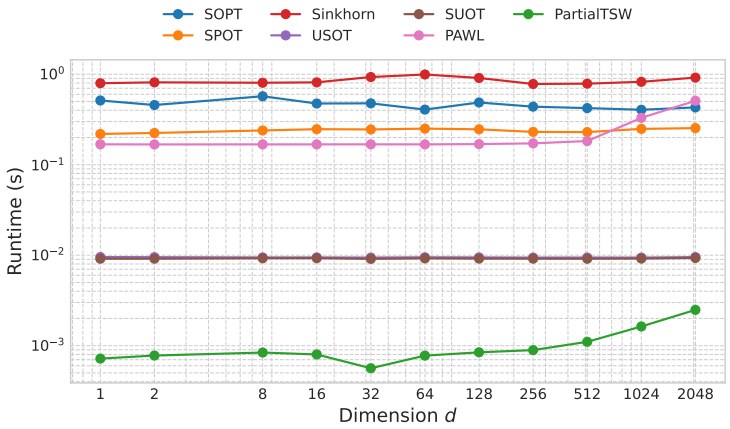

Figure 8: Runtime comparison for PartialTSW and POT/UOT solvers over data dimension d.

Common settings for the compared sliced-based methods (SOPT, SPOT, USOT, SUOT, PAWL) included $L = 10$ projections. For PartialTSW (Ours), we used `num_trees` $= 5$ and `num_lines` $= 2$. This configuration for PartialTSW, where the product of `num_trees` $\times$ `num_lines` $= 10$, offers a comparable number of one-dimensional sorting operations to the $L = 10$ setting in other sliced methods, aiming for a fair comparison. Specific hyperparameters for each method were then set as follows:

- **SOPT**: Regularization parameter $\lambda = 1.0$.
- **SPOT**: The number of transported points k was set to n (the input sample size for each distribution), implying a full matching was performed. (Number of projections $L = 10$, as stated above).
- **Sinkhorn**: Entropic regularization $reg = 0.1$, marginal KL regularization $reg_m = 1.0$, maximum number of Sinkhorn iterations 'numItermax' = 100, and stopping threshold 'stopThr' = 10^{-5}.
- **USOT and SUOT**: Regularization parameters $\rho_1 = 0.01$ and $\rho_2 = 1.0$.
- **PAWL**: The number of transported points k was set to n (implying a full matching).
- **PartialTSW (Ours)**: The target mass proportion $\nu(\mathcal{T})$ was set to 1.0 (with the source mass proportion $\mu(\mathcal{T})$ typically assumed to be 1.0). This choice was made because $\nu(\mathcal{T})$ does not affect the computational runtime of the PartialTSW implementation used in this benchmark.

Furthermore, we present a runtime comparison for varying data dimensions d in Figure 8. The results indicate that the runtime is not significantly affected when d increases.

The runtime comparisons for all methods were conducted with an Intel Xeon Platinum 8580 CPU and an NVIDIA H100 GPU.

E.7 Noisy Point Cloud Gradient Flow

We used clean point cloud data obtained from [2] for the dragon and bunny shapes. Each clean dataset contains 10k data points. We randomly select and add 7% noise points to the target point cloud (bunny). Inspired by [2], the noise is sampled from the region $[-0.6M, 0.6M]^3$ where $M = \max_{i\in\{1,n\}}(||x_i||)$, where x_i is the point in the target. In total, the target point cloud consists of 10k clean points and an additional 700 noise points. We use $L = 10$ projections for SW, and $L = 5$ trees, $k = 2$ lines for TSW and PartialTSW. All methods are trained using Adam optimizer with a learning rate of 10^{-3} over 300 epochs. The results are shown in Figure 3.

All experiments were conducted with an Intel Xeon Platinum 8580 CPU and an NVIDIA H100 GPU.

E.8 Robust Generative Model

E.8.1 Implementation detail

Pre-training an Autoencoder (AE). An Autoencoder (AE) is pre-trained to provide 2D latent representations $z \in \mathbb{R}^2$ for MNIST digits. We employ a Wasserstein Autoencoder with MMD regularization (WAE-MMD) [77] architecture. The AE is trained for 50 epochs using the Adam optimizer with a learning rate of 3×10^{-5} and a batch size of 256. The WAE-MMD loss uses a λ hyperparameter of 500.0 to balance reconstruction and MMD regularization terms. For the MMD term, we match the aggregated posterior $q(z)$ to a uniform prior distribution $p(z) \sim \mathcal{U}[-1, 1]^2$. This encourages the learned latent space to reside approximately within $[-1, 1]^2$. The training data for the AE consists of MNIST digits `0` and `1`, balanced and augmented as described below. The latent dimension is set to $d = 2$.

The Autoencoder, $AE : [0, 1]^{1\times28\times28} \to [0, 1]^{1\times28\times28}$, architecture is as follows:

- **Encoder:**
  - Input: $1 \times 28 \times 28$ (MNIST image)
  - $\texttt{Conv2d}(\text{in\_channels} = 1, \text{out\_channels} = 32, \text{kernel\_size} = 4, \text{stride} = 2, \text{padding} = 1) \to \texttt{ReLU}$ $(32 \times 14 \times 14)$
  - $\texttt{Conv2d}(32, 64, \text{kernel\_size} = 4, \text{stride} = 2, \text{padding} = 1) \to \texttt{ReLU}$ $(64 \times 7 \times 7)$
  - Flatten: $64 \times 7 \times 7 = 3136$ features
  - $\texttt{Linear}(\text{in\_features} = 3136, \text{out\_features} = 512) \to \texttt{ReLU}$
  - $\texttt{Linear}(512, \text{latent\_dim} = 2)$ (for mean μ)
  - $\texttt{Linear}(512, \text{latent\_dim} = 2)$ (for log-variance $\log \sigma^2$)
  - Latent vector $z = \mu + \epsilon \odot \sigma$ (Reparameterization trick)
- **Decoder:**
  - Input: $z \in \mathbb{R}^{\text{latent\_dim}=2}$
  - $\texttt{Linear}(\text{latent\_dim} = 2, 512) \to \texttt{ReLU}$
  - $\texttt{Linear}(512, 3136) \to \texttt{ReLU}$
  - Reshape to $64 \times 7 \times 7$
  - $\texttt{ConvTranspose2d}(64, 32, \text{kernel\_size} = 4, \text{stride} = 2, \text{padding} = 1) \to \texttt{ReLU}$ $(32 \times 14 \times 14)$
  - $\texttt{ConvTranspose2d}(32, 1, \text{kernel\_size} = 4, \text{stride} = 2, \text{padding} = 1) \to \texttt{Sigmoid}$ $(1 \times 28 \times 28)$

Dataset Augmentation for Auxiliary Models. To ensure robust training of the AE and the digit classifier, we prepare a balanced and augmented training set from MNIST digits `0` and `1`. The original MNIST training set contains an unequal number of samples for these digits. We balance these classes by applying data augmentation to the minority class until its sample count matches the majority class. Augmentations include random affine transformations (degrees: $\pm15^\circ$, translation: ±0.15 of image dimension, scale: $0.85 - 1.15\times$) and random rotations ($\pm15^\circ$). This balanced and augmented dataset is used exclusively for training the AE and the binary (`0` vs. `1`) digit classifier. We found that having a balanced dataset for training AE would lead to a balanced latent space for MNIST Digit `0` and `1`.

Pre-training an MNIST Digit Classifier. A convolutional neural network classifier is pre-trained to distinguish between MNIST digits `0` and `1`. It is trained for 20 epochs on the balanced and augmented dataset of these two digits, using the Adam optimizer with a learning rate of 1×10^{-3} and a Cross-Entropy loss function. This classifier achieves approximately 99.99% accuracy on a test set of unseen MNIST `0`s and `1`s and is subsequently used (with frozen weights) to evaluate the class labels of images generated by the main generative model.

The Classifier, $C : [0, 1]^{1\times28\times28} \to \mathbb{R}^2$, architecture is as follows:

- Input: $1 \times 28 \times 28$ (decoded image)
- $\texttt{Conv2d}(1, 32, \text{kernel\_size} = 3, \text{stride} = 1, \text{padding} = 1) \to \texttt{ReLU}$ $(32 \times 28 \times 28)$
- $\texttt{MaxPool2d}(\text{kernel\_size} = 2, \text{stride} = 2)$ $(32 \times 14 \times 14)$
- $\texttt{Conv2d}(32, 64, \text{kernel\_size} = 3, \text{stride} = 1, \text{padding} = 1) \to \texttt{ReLU}$ $(64 \times 14 \times 14)$

- `MaxPool2d`(kernel_size $= 2$, stride $= 2$) $\quad (64 \times 7 \times 7)$
- Flatten: $64 \times 7 \times 7 = 3136$ features
- `Linear`$(3136, 128) \rightarrow$ `ReLU`
- `Linear`$(128,$ num_classes $= 2)$ (Logits for classes `0` and `1`)

Constructing the Observed (Contaminated) Dataset X_{obs} The observed dataset X_{obs} for training the generator G consists of latent representations. These are obtained by encoding MNIST images of digits `0` (target class) and `1` (outlier class) using the pre-trained AE's encoder. Specifically, X_{obs} is a mixture comprising 90% samples from the true latent distribution of digit `0` ($\mathcal{X}_0$) and 10% samples (outliers) from the true latent distribution of digit `1` ($\mathcal{X}_1$). To construct this, we sample latent vectors z' from the prior $\mathcal{U}[-1, 1]^2$, decode them to images $x' = AE_{\text{dec}}(z')$, and classify x' using the pre-trained `0/1` classifier. If x' is classified as `0` (or `1`), z' is added to a pool for $\mathcal{X}_0$ (or $\mathcal{X}_1$). We collect samples until we can form a dataset of $N_{\text{obs}} = 50,000$ latent points, with the 90/10 proportion. These latent points constitute X_{obs} and are scaled to approximately reside within $[-1, 1]^2$.

Training the Generator G. The generator $G : \mathcal{N}(0, I_2) \rightarrow [-1, 1]^2$ is a multi-layer perceptron (MLP) designed to map 2D Gaussian noise $Z \sim \mathcal{N}(0, I_2)$ to the target latent space. The generator is trained by minimizing a (Partial) Optimal Transport distance $D(G(Z), X_{\text{obs}})$, where Z is a batch of noise samples. Training is performed for 30 epochs using the Adam optimizer with a learning rate of 2×10^{-4} and a batch size of 256. Specific (P)OT-based distances D used for PartialTSW and baseline methods are detailed in the main paper.

The generator architecture is:

- Input: $Z \in \mathbb{R}^2 \sim \mathcal{N}(0, I_2)$
- `Linear`$(2, 4) \rightarrow$ `BatchNorm1d`$(4) \rightarrow$ `LeakyReLU`(0.2)
- `Linear`$(4, 8) \rightarrow$ `BatchNorm1d`$(8) \rightarrow$ `LeakyReLU`(0.2)
- `Linear`$(8, 2) \rightarrow$ `Tanh` (Output $z_{\text{gen}} \in [-1, 1]^2$)

Evaluation. To evaluate the generator's ability to learn the target distribution $\mathcal{X}_0$ while ignoring outliers from $\mathcal{X}_1$, we employ two main criteria:

1. **Outlier Rate:** We generate $N_{\text{eval}} = 5,000$ latent samples $z_{\text{gen}} = G(Z)$. These latent samples are decoded into images $\hat{x} = AE_{\text{dec}}(z_{\text{gen}})$ using the pre-trained AE's decoder. The resulting images are then classified by the pre-trained `0/1` digit classifier. The outlier rate is the percentage of generated images classified as digit `1`. A lower rate indicates better robustness.
2. **Sample Quality and Diversity:** We qualitatively assess the generated samples by visualizing the decoded images $\hat{x}$ and their corresponding latent representations z_{gen}. We look for high-fidelity generation of digit `0` and good coverage of its variations, as indicated by a well-distributed latent space for the generated samples classified as `0`.

Performance summaries, including outlier rates and visual comparisons, are provided in Figure 4 and Table 1 in the main text.

Hardware Settings. The experiments for all methods were conducted on a system equipped with an Intel Xeon Platinum 8580 CPU and one NVIDIA H100 GPU.

E.8.2 Ablation result for baselines

We evaluate the impact of hyperparameter settings on each method's ability to isolate the target MNIST `0` distribution from the 10% MNIST `1` outliers present in the training data. The following summarizes these ablation results (Figures 9–15), focusing on the percentage of generated MNIST `1` outliers and, where applicable, qualitative aspects of the learned distributions and generated samples.

SPOT [9]. Figure 9 demonstrates SPOT's varying success in isolating the target MNIST `0` data from the 10% `1` outliers, contingent on its hyperparameter k. While very small k values (e.g., $k = 10$, yielding 45.62% MNIST `1` outliers) or very large k values (e.g., $k = 256$, yielding 16.20% outliers) result in poor outlier rejection, an optimal range for k around $200 - 210$ reduces the MNIST `1` outlier rate to $6 - 7\%$. This indicates substantial but incomplete removal of the 10% outliers.

SOPT [2]. SOPT's effectiveness in discarding the 10% MNIST `1` outliers is modulated by its regularization parameter λ, as shown in Figure 10. The lowest outlier percentage achieved by SOPT is 13.28% (at $\lambda = 0.01$), which still exceeds the initial 10% contamination level. Larger values of λ lead to even higher and relatively stable outlier rates (around $15 - 16.42\%$), indicating a persistent difficulty for SOPT in cleanly separating the target distribution in this setup.

Sinkhorn [74]. Sinkhorn shows the potential for complete removal of the 10% MNIST `1` outliers when its entropic regularization reg and marginal regularization reg_m are appropriately co-tuned (Figure 11). Specifically, setting $reg = reg_m$ at values of $0.5, 0.7$, or 0.9 results in 0% MNIST `1` outlier generation, successfully achieving the task's objective. However, imbalanced or overly small regularization values lead to substantial outlier contamination (e.g., 52.48% for $reg = reg_m = 0.3$, or 70.56% for $reg = 0.9, reg_m = 0.1$). Moreover, qualitative inspection of the results (Figure 11, particularly for $reg = reg_m \in \{0.5, 0.7, 0.9\}$) reveals that while Sinkhorn effectively removes outliers, the generated latent distribution for MNIST `0` digits appears clustered, and the corresponding decoded images may lack diversity compared to the true distribution. This suggests a potential trade-off between perfect outlier rejection and capturing the full diversity of the target class for this method under these settings.

SUOT [7]. The performance of SUOT in the task of removing 10% MNIST `1` outliers is consistently poor across the explored range of its marginal regularization parameters ρ_1 and ρ_2, as detailed in Figure 12. The method yields a high MNIST `1` outlier rate of approximately 41% regardless of the hyperparameter settings tested, indicating a failure to distinguish the target MNIST `0` distribution from the contaminants.

USOT [7]. USOT, while performing better than SUOT, still struggles to fully reject the 10% MNIST `1` outliers (Figure 13). Across the tested range of its ρ_1 and ρ_2 hyperparameters, USOT yields a consistent MNIST `1` outlier rate of approximately 17.08%. This suggests that while it mitigates some contamination, it does not fully isolate the target MNIST `0` distribution in this scenario.

PAWL [13]. PAWL demonstrates exceptional success in the goal of removing 10% MNIST `1` outliers, as shown in its ablation study (Figure 14). It consistently achieves a 0% MNIST `1` outlier rate across all tested values of its hyperparameter k (from 10 to 256). This indicates PAWL's strong capability to identify and learn the target MNIST `0` distribution while completely ignoring outliers, exhibiting robust performance across a wide range of k. However, as noted in the main text and suggested by qualitative inspection of Figure 14, this strong outlier rejection by PAWL may be accompanied by less sample diversity, with its learned latent space showing heavily concentrated clusters.

PartialTSW (Ours). Our PartialTSW method shows strong capabilities in removing the 10% MNIST `1` outliers, with performance critically depending on its mass parameter $\nu(\mathcal{T})$ (Figure 15). Complete outlier rejection (0% MNIST `1` outliers) is achieved for $\nu(\mathcal{T})$ values between 0.3 and 0.6. Setting $\nu(\mathcal{T})$ closer to the true inlier fraction of 0.9 (which yields 9.72% MNIST `1` outliers) leads to the model fitting the outliers. This highlights that optimal robustness for PartialTSW is achieved when $\nu(\mathcal{T})$ is chosen to be somewhat less than the actual inlier data proportion in the contaminated dataset. Qualitatively, as seen in Figure 15 and highlighted in our main findings, the settings achieving complete outlier rejection (e.g., $\nu(\mathcal{T}) \in [0.3, 0.6]$) also yield a well-distributed latent space and diverse image samples for the MNIST `0` class, effectively capturing the target distribution.

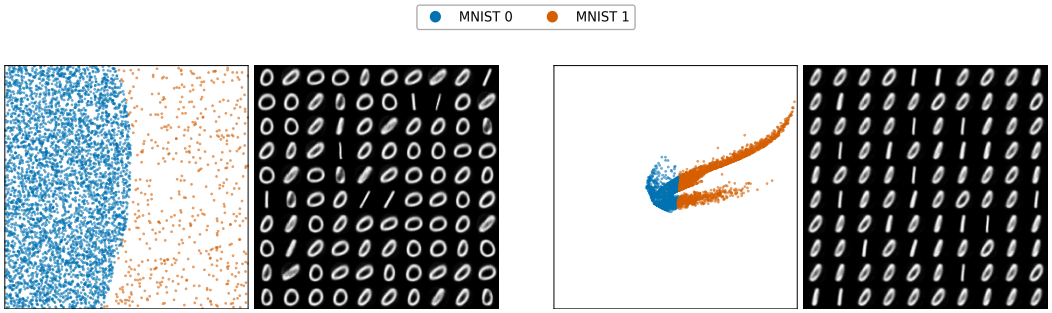

(a) Dataset with 90% MNIST 0 and 10% MNIST 1

(b) $k = 10 \rightarrow 45.62\%$ MNIST 1

(c) $k = 25 \rightarrow 46.36\%$ MNIST 1

(d) $k = 50 \rightarrow 27.58\%$ MNIST 1

(e) $k = 75 \rightarrow 18.14\%$ MNIST 1

(f) $k = 100 \rightarrow 14.86\%$ MNIST 1

(g) $k = 200 \rightarrow 6.32\%$ MNIST 1

(h) $k = 200 \rightarrow 7.12\%$ MNIST 1

(i) $k = 210 \rightarrow 7.06\%$ MNIST 1

(j) $k = 256 \rightarrow 16.20\%$ MNIST 1

Figure 9: Ablation study of SPOT [9] for robust image generation. The figure illustrates the percentage of generated MNIST 1 digits (outliers), along with the corresponding learned latent distributions (left) and decoded image samples (right).

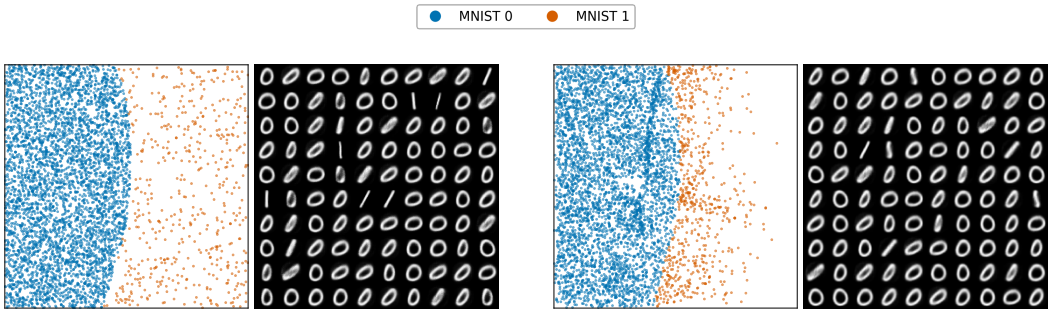

(a) Dataset with 90% MNIST 0 and 10% MNIST 1

(b) $\lambda = 0.01 \rightarrow$ 13.28% MNIST 1

(c) $\lambda = 0.05 \rightarrow$ 15.02% MNIST 1

(d) $\lambda = 0.1 \rightarrow$ 16.20% MNIST 1

(e) $\lambda = 0.5 \rightarrow$ 16.42% MNIST 1

(f) $\lambda = 1 \rightarrow$ 16.20% MNIST 1

(g) $\lambda = 10 \rightarrow$ 16.20% MNIST 1

(h) $\lambda = 100 \rightarrow$ 16.20% MNIST 1

Figure 10: Ablation study of SOPT [2] for robust image generation. The figure illustrates the percentage of generated MNIST 1 digits (outliers), along with the corresponding learned latent distributions (left) and decoded image samples (right).

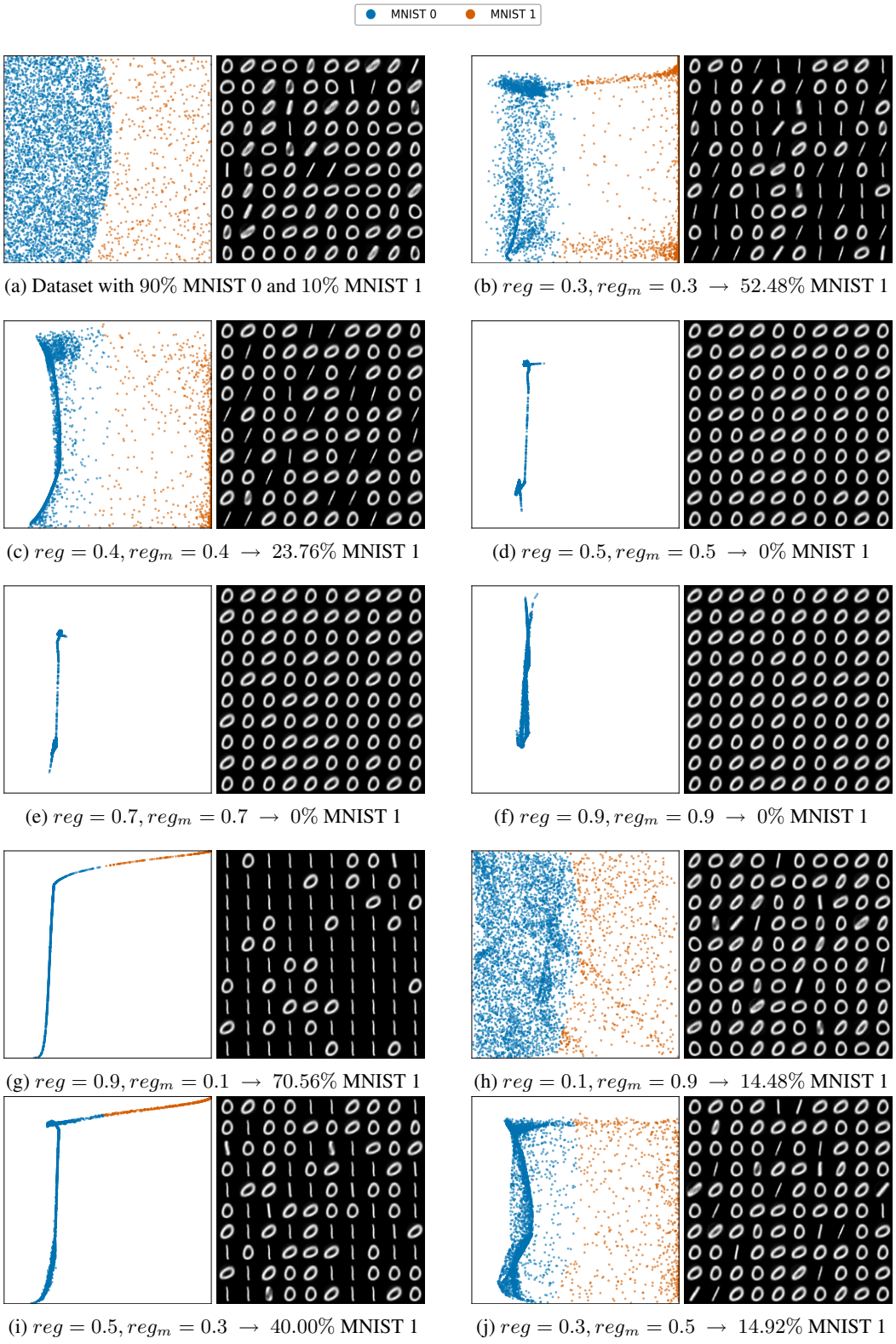

(a) Dataset with 90% MNIST 0 and 10% MNIST 1

(b) $reg = 0.3, reg_m = 0.3 \rightarrow$ 52.48% MNIST 1

(c) $reg = 0.4, reg_m = 0.4 \rightarrow$ 23.76% MNIST 1

(d) $reg = 0.5, reg_m = 0.5 \rightarrow$ 0% MNIST 1

(e) $reg = 0.7, reg_m = 0.7 \rightarrow$ 0% MNIST 1

(f) $reg = 0.9, reg_m = 0.9 \rightarrow$ 0% MNIST 1

(g) $reg = 0.9, reg_m = 0.1 \rightarrow$ 70.56% MNIST 1

(h) $reg = 0.1, reg_m = 0.9 \rightarrow$ 14.48% MNIST 1

(i) $reg = 0.5, reg_m = 0.3 \rightarrow$ 40.00% MNIST 1

(j) $reg = 0.3, reg_m = 0.5 \rightarrow$ 14.92% MNIST 1

Figure 11: Ablation study of Sinkhorn [74] for robust image generation. The figure illustrates the percentage of generated MNIST 1 digits (outliers), along with the corresponding learned latent distributions (left) and decoded image samples (right).

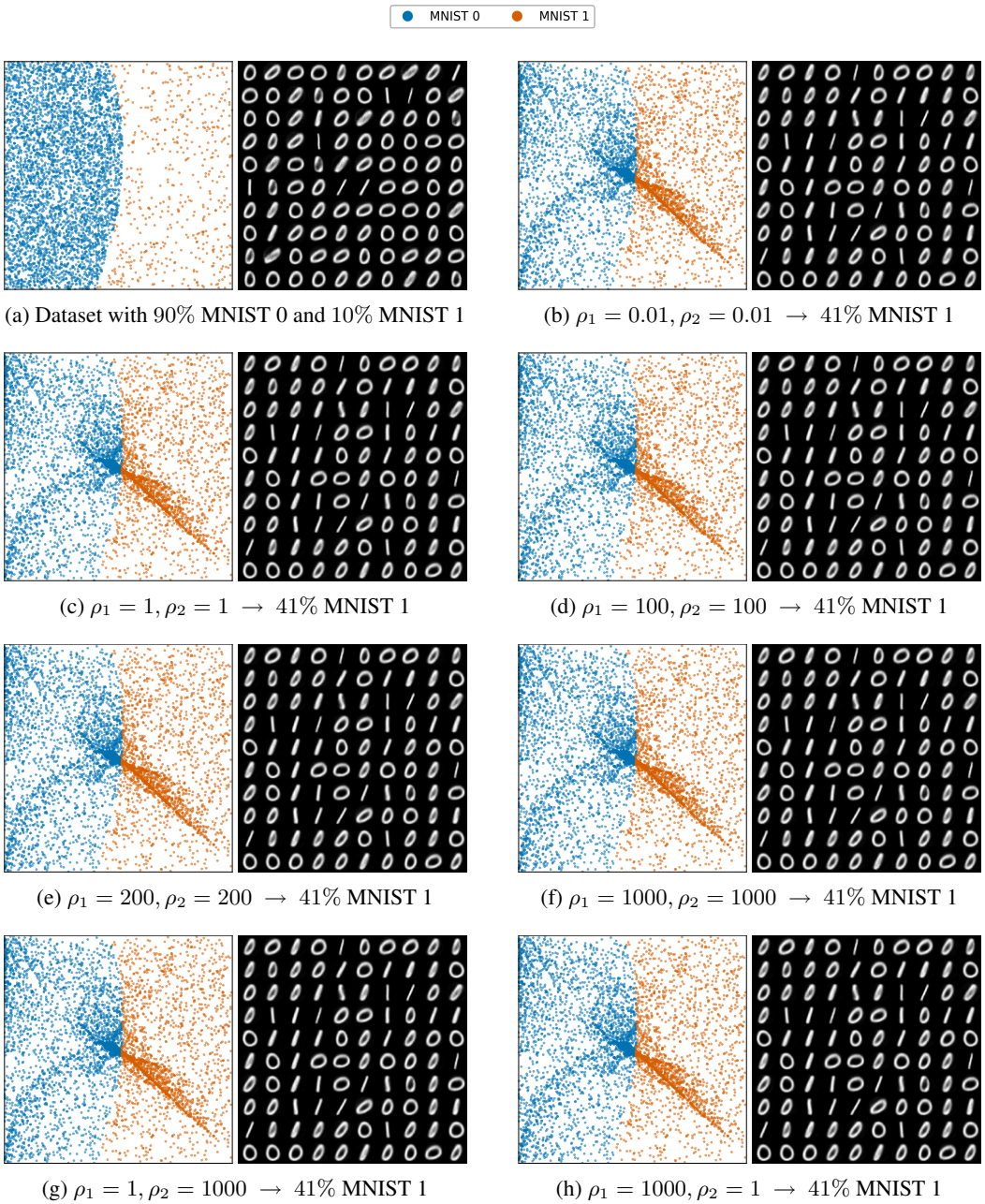

(a) Dataset with 90% MNIST 0 and 10% MNIST 1

(b) $\rho_1 = 0.01, \rho_2 = 0.01 \rightarrow$ 41% MNIST 1

(c) $\rho_1 = 1, \rho_2 = 1 \rightarrow$ 41% MNIST 1

(d) $\rho_1 = 100, \rho_2 = 100 \rightarrow$ 41% MNIST 1

(e) $\rho_1 = 200, \rho_2 = 200 \rightarrow$ 41% MNIST 1

(f) $\rho_1 = 1000, \rho_2 = 1000 \rightarrow$ 41% MNIST 1

(g) $\rho_1 = 1, \rho_2 = 1000 \rightarrow$ 41% MNIST 1

(h) $\rho_1 = 1000, \rho_2 = 1 \rightarrow$ 41% MNIST 1

Figure 12: Ablation study of SUOT [7] for robust image generation. The figure illustrates the percentage of generated MNIST 1 digits (outliers), along with the corresponding learned latent distributions (left) and decoded image samples (right).

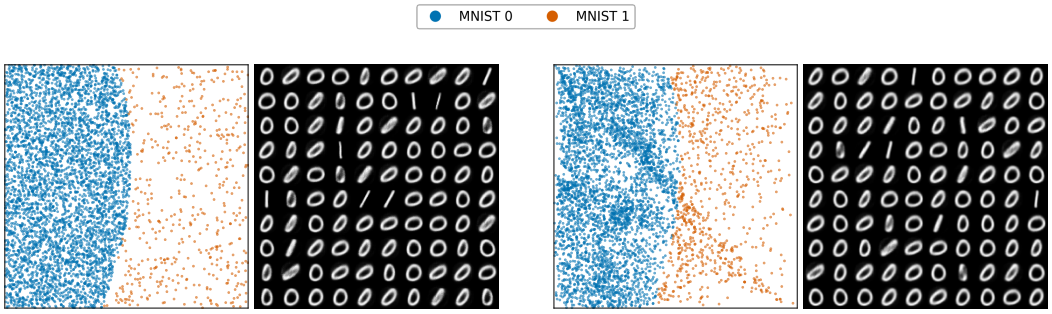

(a) Dataset with 90% MNIST 0 and 10% MNIST 1

(b) $\rho_1 = 0.01, \rho_2 = 0.01 \rightarrow$ 17.08% MNIST 1

(c) $\rho_1 = 1, \rho_2 = 1 \rightarrow$ 17.08% MNIST 1

(d) $\rho_1 = 100, \rho_2 = 100 \rightarrow$ 17.08% MNIST 1

(e) $\rho_1 = 200, \rho_2 = 200 \rightarrow$ 17.08% MNIST 1

(f) $\rho_1 = 1000, \rho_2 = 1000 \rightarrow$ 17.08% MNIST 1

(g) $\rho_1 = 1, \rho_2 = 1000 \rightarrow$ 17.08% MNIST 1

(h) $\rho_1 = 1000, \rho_2 = 1 \rightarrow$ 17.08% MNIST 1

Figure 13: Ablation study of USOT [7] for robust image generation. The figure illustrates the percentage of generated MNIST 1 digits (outliers), along with the corresponding learned latent distributions (left) and decoded image samples (right).

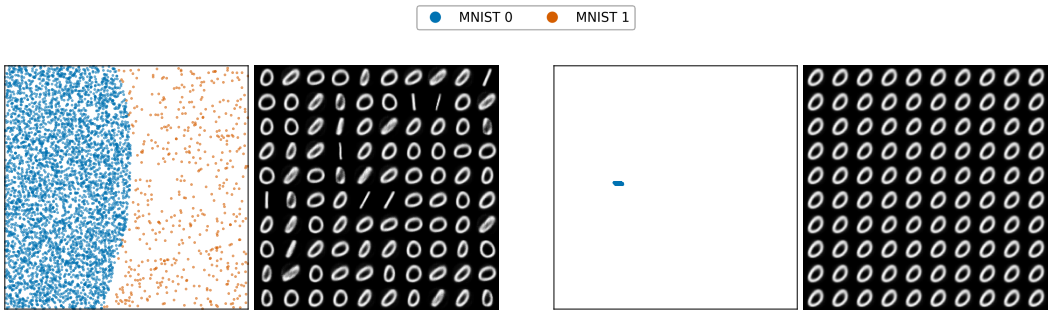

(a) Dataset with 90% MNIST 0 and 10% MNIST 1

(b) $k = 10 \rightarrow 0\%$ MNIST 1

(c) $k = 25 \rightarrow 0\%$ MNIST 1

(d) $k = 50 \rightarrow 0\%$ MNIST 1

(e) $k = 75 \rightarrow 0\%$ MNIST 1

(f) $k = 100 \rightarrow 0\%$ MNIST 1

(g) $k = 200 \rightarrow 0\%$ MNIST 1

(h) $k = 256 \rightarrow 0\%$ MNIST 1

Figure 14: Ablation study of PAWL [13] for robust image generation. The figure illustrates the percentage of generated MNIST 1 digits (outliers), along with the corresponding learned latent distributions (left) and decoded image samples (right).

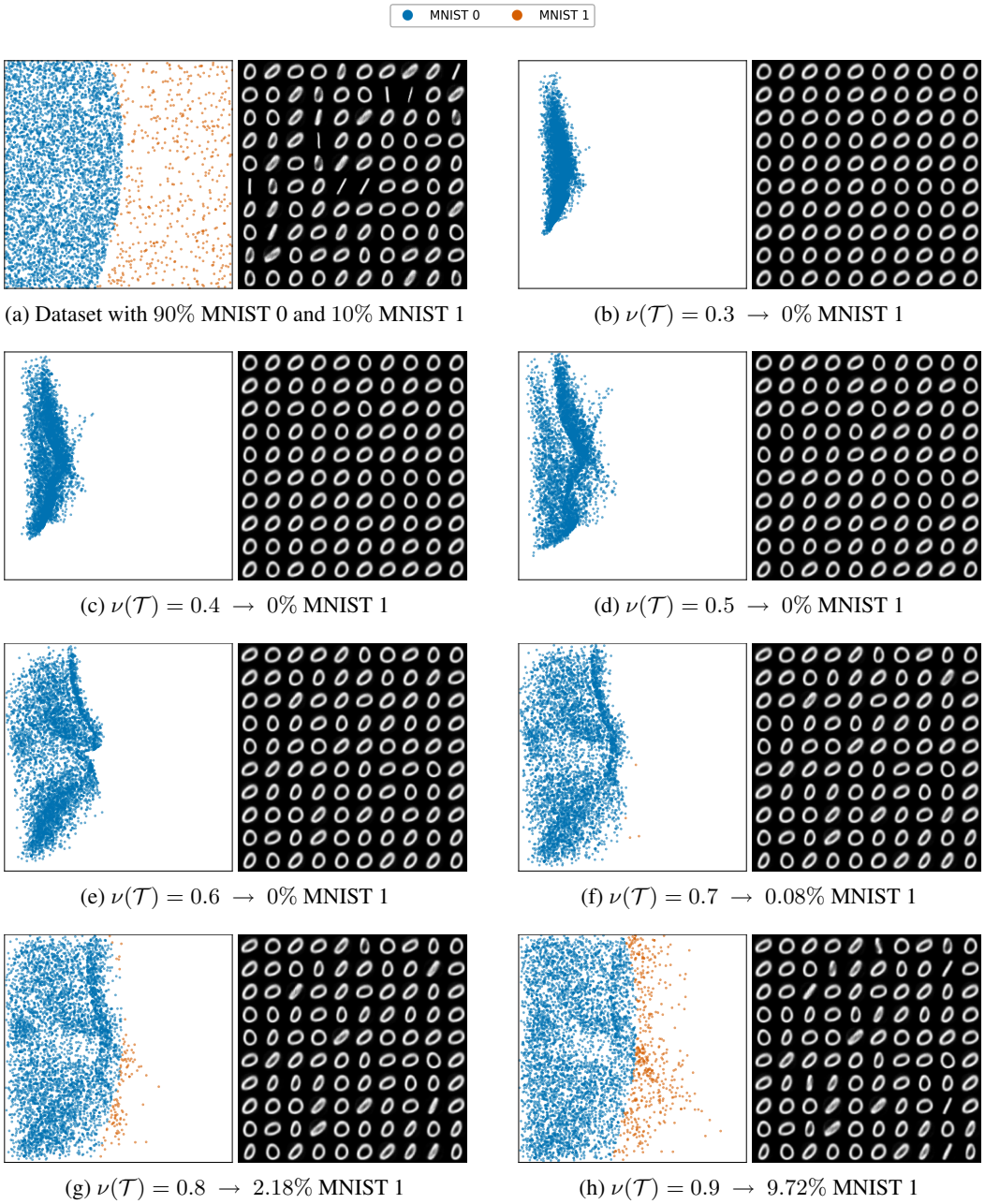

(a) Dataset with 90% MNIST 0 and 10% MNIST 1

(b) $\nu(\mathcal{T}) = 0.3 \rightarrow 0\%$ MNIST 1

(c) $\nu(\mathcal{T}) = 0.4 \rightarrow 0\%$ MNIST 1

(d) $\nu(\mathcal{T}) = 0.5 \rightarrow 0\%$ MNIST 1

(e) $\nu(\mathcal{T}) = 0.6 \rightarrow 0\%$ MNIST 1

(f) $\nu(\mathcal{T}) = 0.7 \rightarrow 0.08\%$ MNIST 1

(g) $\nu(\mathcal{T}) = 0.8 \rightarrow 2.18\%$ MNIST 1

(h) $\nu(\mathcal{T}) = 0.9 \rightarrow 9.72\%$ MNIST 1

Figure 15: Ablation study of Partial-TSW (Ours) for robust image generation. The figure illustrates the percentage of generated MNIST 1 digits (outliers), along with the corresponding learned latent distributions (left) and decoded image samples (right).

E.9 Imbalance Image to Image Translation

E.9.1 Implementation detail

This section outlines the experimental setup for the imbalanced image-to-image translation task, specifically converting "Young" faces to "Adult" faces.

Dataset. Our experimental dataset and preprocessing follow [41]. We utilize the FFHQ dataset [37] of 1024×1024 images. These images are encoded into a 512-dimensional latent space using a pre-trained ALAE autoencoder [64]. The resulting latent representations are categorized into two classes: "Young" and "Adult", based on a cutoff age of 45 years. This process yields an imbalanced dataset comprising approximately 38,000 "Young" latent vectors and 10,500 "Adult" latent vectors. The translation is performed within this 512-dimensional latent space.

Translation Accuracy. To evaluate the accuracy of the translation from the "Young" to the "Adult" domain, we adapt the procedure from [28]. A classifier is pre-trained on the 512-dimensional latent vectors to distinguish between "Young" and "Adult" images. This pre-trained classifier, which achieves 99% accuracy on a held-out test set of latent vectors, is then used to assess whether the translated latent vectors $M(X)$ (where X are latents from the "Young" domain) are correctly classified as "Adult".

Perceptual Similarity. We measure the perceptual similarity between the original images (reconstructed from X) and the translated images (reconstructed from $M(X)$) using the Learned Perceptual Image Patch Similarity (LPIPS) metric [90]. For LPIPS calculations, we use the AlexNet backbone with pre-trained weights. While some prior work, such as [28], employed attribute-specific metrics like "Keep Accuracy" (e.g., for preserving gender), we selected LPIPS to offer a more comprehensive assessment of overall visual fidelity post-translation, rather than focusing on a single attribute.

UOT-FM Baseline. We compare against Unbalanced Optimal Transport Flow Matching (UOT-FM) [22]. Following [28], we parameterize vector field v_θ using a 2-layer feed-forward network with 512 hidden neurons and ReLU activation. We apply their default configuration for Flow Matching. Consistent with the approach in [28], we perform an ablation study over the regularization parameter λ, which controls the penalization of deviations from marginal constraints.

ULightOT Baseline. We also include ULightOT [28] as a baseline. We adapted the publicly available code and default models for our experiments. Following the methodology in [28], we ablate the parameter τ, which governs the degree of mass conservation in the transport plan. Our empirical observations indicate that the performance of ULightOT saturates for $\tau > 1000$. For instance, increasing τ to 10000 yielded negligible changes in the Accuracy-LPIPS trade-off compared to $\tau = 1000$, as shown by the results (e.g., in Figure 5 of the main text).

Mapping Network Architecture.

For methods such as SW, Db-TSW, and our PartialTSW, the mapping network M is implemented using a `ResidualMLP`. The input to this network is a latent vector $z \in \mathbb{R}^{512}$. The specific `ResidualMLP` configuration used has an input/output dimension of 512, with `num_hidden_blocks=0` and `hidden_dim_multiplier=1`.

The core of this network, denoted as MLP_{core}, processes the input z through the following sequence of operations:

- Apply an initial linear transformation: $\texttt{Linear}(512, 512)$
- Followed by layer normalization: $\texttt{LayerNorm}(512)$
- Then, apply the GELU activation function: $\texttt{GELU}()$
- Apply dropout with a rate of 0.1: $\texttt{Dropout}(0.1)$
- Finally, apply an output linear projection: $\texttt{Linear}(512, 512)$

Let the output of this sequential MLP_{core} block be $\text{MLP}_{\text{core}}(z)$.

The final output of the mapping network $M(z)$ is obtained by adding a scaled residual connection to the original input:

$$M(z) = z + \alpha \cdot \text{MLP}_{\text{core}}(z)$$

where α is a learnable scalar parameter (analogous to LayerScale) that is initialized to 0.1.

Table 5: Comparison of model size and training time per epoch for the Young-to-Adult translation.

Method	Number of Parameters	Time (s/epoch)
SW	526,337	6
Db-TSW	526,337	25
PartialTSW (Ours)	**526,337**	**25**
UOT-FM	788,224	35
ULightOT	5,263,380	60

Table 6: Full image-to-image translation results, averaged over 5 runs. Our method, PartialTSW, consistently demonstrates a superior trade-off between Accuracy (↑) and LPIPS (↓) across all translation directions.

Method	Parameter	W→M		M→W		A→Y	
		Acc (%) ↑	LPIPS ↓	Acc (%) ↑	LPIPS ↓	Acc (%) ↑	LPIPS ↓
SW	–	93.95	0.4418	91.68	0.4546	89.82	0.4041
Db-TSW	–	94.13	0.4436	92.07	0.4546	89.58	0.4022
UOT-FM	$\epsilon = 0.0005$	49.21	0.3914	85.52	0.4269	79.77	0.3836
	$\epsilon = 0.005$	70.69	0.4531	94.19	0.4749	92.91	0.4129
	$\epsilon = 0.05$	80.28	0.4899	95.40	0.5106	97.40	0.4693
	$\epsilon = 0.1$	81.50	0.5198	97.91	0.5369	98.43	0.4828
ULightOT	$\tau = 50.0$	76.36	0.4102	85.91	0.4086	84.31	0.3452
	$\tau = 250.0$	86.36	0.4466	92.81	0.4516	90.49	0.3906
	$\tau = 1000.0$	88.07	0.4557	93.91	0.4626	92.00	0.4060
	$\tau = 10000.0$	88.75	0.4589	94.37	0.4663	92.49	0.4112
PartialTSW (Ours)	$\nu(\mathcal{T}) = 0.3$	99.66	0.6058	99.13	0.6088	97.64	0.5595
	$\nu(\mathcal{T}) = 0.5$	98.04	0.5377	95.36	0.5493	93.76	0.4928
	$\nu(\mathcal{T}) = 0.9$	95.67	0.4515	94.39	0.4682	91.16	0.4024
	$\nu(\mathcal{T}) = 1.1$	92.03	0.4408	90.62	0.4533	89.34	0.4011

E.9.2 Additional Experimental Results

This section provides further details on model parameterization and presents a complete set of results for all image-to-image translation directions.

Parameterization and Efficiency. As detailed in the implementation section, we adhered to the official configurations for the baseline methods. We utilized a Gaussian Mixture Model (GMM) for ULightOT [28] and a flow-matching network for UOT-FM [22], ensuring a faithful and robust comparison.

For our method (PartialTSW) and the other standard OT baselines (SW [10], Db-TSW [80]), we employed the `ResidualMLP` architecture described in Appendix E.9. While a GMM parameterization is theoretically feasible for our method, we chose the neural network as it represents a more common, flexible, and standard approach for generative modeling tasks in recent literature.

This choice of parameterization is not only standard but also highly efficient. As shown in Table 5, our `ResidualMLP` approach is significantly more lightweight and faster per epoch than the complex models required by UOT-FM and ULightOT. This demonstrates that PartialTSW is not only effective but also computationally efficient.

Results for All Translation Directions. In the main paper, our analysis centered on the Young-to-Adult (Y→A) translation task. This direction was chosen as it represents the most significant class imbalance within the dataset. The class distribution of the pre-processed FFHQ latent dataset is as follows: Young (approximately 15K Man, 23K Woman) and Adult (approximately 7K Man, 3.5K Woman).

To provide a comprehensive analysis, we conducted additional experiments for all other possible translation directions: Woman-to-Man (W→M), Man-to-Woman (M→W), and Adult-to-Young (A→Y). The results, averaged over 5 independent runs, are presented in Table 6.

These findings confirm that Partial-TSW consistently achieves a superior trade-off between translation accuracy and perceptual similarity (LPIPS) across all translation settings. For instance, in the W→M setting, Partial-TSW (with $\nu(\mathcal{T}) = 0.9$) achieves a high accuracy of 95.67% while maintaining a strong LPIPS of 0.4515. In contrast, for UOT-FM to reach a competitive accuracy (e.g., 81.50% with $\epsilon = 0.1$), it incurs a significantly worse LPIPS of 0.5198. This pattern, visible across the tasks, highlights our method's ability to find a more effective and stable balance between the two competing objectives.

F Boarder Impacts

The introduction of the PartialTSW in this paper has a substantial societal impact by enhancing the precision and adaptability of optimal transport methods in various practical applications. This method can drive progress in numerous fields, such as healthcare, where better image processing techniques can aid in more accurate medical imaging diagnostics, or in the arts and entertainment industry, where enhanced generative models can lead to more sophisticated and creative outputs. Furthermore, the ability to handle dynamic settings efficiently opens new possibilities for real-time data analysis and decision-making in various sectors, including finance, logistics, and environmental monitoring. Ultimately, the method contributes to making advanced computational techniques more versatile and applicable to a broader range of real-world problems, thereby fostering innovation and improving societal well-being.

NeurIPS Paper Checklist

1. **Claims**

   Question: Do the main claims made in the abstract and introduction accurately reflect the paper's contributions and scope?

   Answer: [Yes]

   Justification: The main claims made in the abstract and introduction accurately reflect the paper's contributions and scope.

   Guidelines:

   - The answer NA means that the abstract and introduction do not include the claims made in the paper.
   - The abstract and/or introduction should clearly state the claims made, including the contributions made in the paper and important assumptions and limitations. A No or NA answer to this question will not be perceived well by the reviewers.
   - The claims made should match theoretical and experimental results, and reflect how much the results can be expected to generalize to other settings.
   - It is fine to include aspirational goals as motivation as long as it is clear that these goals are not attained by the paper.

2. **Limitations**

   Question: Does the paper discuss the limitations of the work performed by the authors?

   Answer: [Yes]

   Justification: We have discussed the limitations of the work in the Conclusion.

   Guidelines:

   - The answer NA means that the paper has no limitation while the answer No means that the paper has limitations, but those are not discussed in the paper.
   - The authors are encouraged to create a separate "Limitations" section in their paper.
   - The paper should point out any strong assumptions and how robust the results are to violations of these assumptions (e.g., independence assumptions, noiseless settings, model well-specification, asymptotic approximations only holding locally). The authors should reflect on how these assumptions might be violated in practice and what the implications would be.
   - The authors should reflect on the scope of the claims made, e.g., if the approach was only tested on a few datasets or with a few runs. In general, empirical results often depend on implicit assumptions, which should be articulated.
   - The authors should reflect on the factors that influence the performance of the approach. For example, a facial recognition algorithm may perform poorly when image resolution is low or images are taken in low lighting. Or a speech-to-text system might not be used reliably to provide closed captions for online lectures because it fails to handle technical jargon.
   - The authors should discuss the computational efficiency of the proposed algorithms and how they scale with dataset size.
   - If applicable, the authors should discuss possible limitations of their approach to address problems of privacy and fairness.
   - While the authors might fear that complete honesty about limitations might be used by reviewers as grounds for rejection, a worse outcome might be that reviewers discover limitations that aren't acknowledged in the paper. The authors should use their best judgment and recognize that individual actions in favor of transparency play an important role in developing norms that preserve the integrity of the community. Reviewers will be specifically instructed to not penalize honesty concerning limitations.

3. **Theory assumptions and proofs**

   Question: For each theoretical result, does the paper provide the full set of assumptions and a complete (and correct) proof?

   Answer: [Yes] .

Justification: We have provided full set of assumptions and complete proof for all theoretical results in Appendix.

Guidelines:

- The answer NA means that the paper does not include theoretical results.
- All the theorems, formulas, and proofs in the paper should be numbered and cross-referenced.
- All assumptions should be clearly stated or referenced in the statement of any theorems.
- The proofs can either appear in the main paper or the supplemental material, but if they appear in the supplemental material, the authors are encouraged to provide a short proof sketch to provide intuition.
- Inversely, any informal proof provided in the core of the paper should be complemented by formal proofs provided in appendix or supplemental material.
- Theorems and Lemmas that the proof relies upon should be properly referenced.

4. **Experimental result reproducibility**

Question: Does the paper fully disclose all the information needed to reproduce the main experimental results of the paper to the extent that it affects the main claims and/or conclusions of the paper (regardless of whether the code and data are provided or not)?

Answer: [Yes]

Justification: We have mentioned all information to reproduce the main experimental results in Appendix E. All necessary details for reproducing the main experimental results are documented. This includes comprehensive descriptions of network architectures, training procedures, and specific hyperparameters. Task-specific configurations are outlined in their respective subsections. The code is also included as supplementary material to further support reproducibility.

Guidelines:

- The answer NA means that the paper does not include experiments.
- If the paper includes experiments, a No answer to this question will not be perceived well by the reviewers: Making the paper reproducible is important, regardless of whether the code and data are provided or not.
- If the contribution is a dataset and/or model, the authors should describe the steps taken to make their results reproducible or verifiable.
- Depending on the contribution, reproducibility can be accomplished in various ways. For example, if the contribution is a novel architecture, describing the architecture fully might suffice, or if the contribution is a specific model and empirical evaluation, it may be necessary to either make it possible for others to replicate the model with the same dataset, or provide access to the model. In general. releasing code and data is often one good way to accomplish this, but reproducibility can also be provided via detailed instructions for how to replicate the results, access to a hosted model (e.g., in the case of a large language model), releasing of a model checkpoint, or other means that are appropriate to the research performed.
- While NeurIPS does not require releasing code, the conference does require all submissions to provide some reasonable avenue for reproducibility, which may depend on the nature of the contribution. For example
  (a) If the contribution is primarily a new algorithm, the paper should make it clear how to reproduce that algorithm.
  (b) If the contribution is primarily a new model architecture, the paper should describe the architecture clearly and fully.
  (c) If the contribution is a new model (e.g., a large language model), then there should either be a way to access this model for reproducing the results or a way to reproduce the model (e.g., with an open-source dataset or instructions for how to construct the dataset).
  (d) We recognize that reproducibility may be tricky in some cases, in which case authors are welcome to describe the particular way they provide for reproducibility. In the case of closed-source models, it may be that access to the model is limited in

some way (e.g., to registered users), but it should be possible for other researchers to have some path to reproducing or verifying the results.

5. **Open access to data and code**

   Question: Does the paper provide open access to the data and code, with sufficient instructions to faithfully reproduce the main experimental results, as described in supplemental material?

   Answer: [Yes]

   Justification: We have provided data and code in the supplemental material, with detailed instructions to reproduce the results.

   Guidelines:

   - The answer NA means that paper does not include experiments requiring code.
   - Please see the NeurIPS code and data submission guidelines (`https://nips.cc/public/guides/CodeSubmissionPolicy`) for more details.
   - While we encourage the release of code and data, we understand that this might not be possible, so "No" is an acceptable answer. Papers cannot be rejected simply for not including code, unless this is central to the contribution (e.g., for a new open-source benchmark).
   - The instructions should contain the exact command and environment needed to run to reproduce the results. See the NeurIPS code and data submission guidelines (`https://nips.cc/public/guides/CodeSubmissionPolicy`) for more details.
   - The authors should provide instructions on data access and preparation, including how to access the raw data, preprocessed data, intermediate data, and generated data, etc.
   - The authors should provide scripts to reproduce all experimental results for the new proposed method and baselines. If only a subset of experiments are reproducible, they should state which ones are omitted from the script and why.
   - At submission time, to preserve anonymity, the authors should release anonymized versions (if applicable).
   - Providing as much information as possible in supplemental material (appended to the paper) is recommended, but including URLs to data and code is permitted.

6. **Experimental setting/details**

   Question: Does the paper specify all the training and test details (e.g., data splits, hyperparameters, how they were chosen, type of optimizer, etc.) necessary to understand the results?

   Answer: [Yes]

   Justification: We have provided all information about training and test details in Appendix E. We have included information on network architectures, optimizer types, batch sizes, number of training iterations, and the specific hyperparameters used in each experiment. In particular, Section E.7 describes the experimental setup for the point cloud experiments. Section E.8 focuses on the robust generative model, and Section E.9 outlines the details for the image translation task.

   Guidelines:

   - The answer NA means that the paper does not include experiments.
   - The experimental setting should be presented in the core of the paper to a level of detail that is necessary to appreciate the results and make sense of them.
   - The full details can be provided either with the code, in appendix, or as supplemental material.

7. **Experiment statistical significance**

   Question: Does the paper report error bars suitably and correctly defined or other appropriate information about the statistical significance of the experiments?

   Answer: [Yes]

   Justification: Our experimental results are provided with error bars. We report statistical significance by including the mean and standard deviation over multiple runs in Table 2.

Guidelines:

- The answer NA means that the paper does not include experiments.
- The authors should answer "Yes" if the results are accompanied by error bars, confidence intervals, or statistical significance tests, at least for the experiments that support the main claims of the paper.
- The factors of variability that the error bars are capturing should be clearly stated (for example, train/test split, initialization, random drawing of some parameter, or overall run with given experimental conditions).
- The method for calculating the error bars should be explained (closed form formula, call to a library function, bootstrap, etc.)
- The assumptions made should be given (e.g., Normally distributed errors).
- It should be clear whether the error bar is the standard deviation or the standard error of the mean.
- It is OK to report 1-sigma error bars, but one should state it. The authors should preferably report a 2-sigma error bar than state that they have a 96% CI, if the hypothesis of Normality of errors is not verified.
- For asymmetric distributions, the authors should be careful not to show in tables or figures symmetric error bars that would yield results that are out of range (e.g. negative error rates).
- If error bars are reported in tables or plots, The authors should explain in the text how they were calculated and reference the corresponding figures or tables in the text.

8. **Experiments compute resources**

   Question: For each experiment, does the paper provide sufficient information on the computer resources (type of compute workers, memory, time of execution) needed to reproduce the experiments?

   Answer: [Yes]

   Justification: We have provided sufficient information about computing resources needed to reproduce the experiments in Appendix.

   Guidelines:

   - The answer NA means that the paper does not include experiments.
   - The paper should indicate the type of compute workers CPU or GPU, internal cluster, or cloud provider, including relevant memory and storage.
   - The paper should provide the amount of compute required for each of the individual experimental runs as well as estimate the total compute.
   - The paper should disclose whether the full research project required more compute than the experiments reported in the paper (e.g., preliminary or failed experiments that didn't make it into the paper).

9. **Code of ethics**

   Question: Does the research conducted in the paper conform, in every respect, with the NeurIPS Code of Ethics `https://neurips.cc/public/EthicsGuidelines`?

   Answer: [Yes]

   Justification: The research conducted in the paper conforms, in every respect, with the NeurIPS Code of Ethics.

   Guidelines:

   - The answer NA means that the authors have not reviewed the NeurIPS Code of Ethics.
   - If the authors answer No, they should explain the special circumstances that require a deviation from the Code of Ethics.
   - The authors should make sure to preserve anonymity (e.g., if there is a special consideration due to laws or regulations in their jurisdiction).

10. **Broader impacts**

    Question: Does the paper discuss both potential positive societal impacts and negative societal impacts of the work performed?

Answer: [Yes]

Justification: We have discussed Broader impacts in Appendix.

Guidelines:

- The answer NA means that there is no societal impact of the work performed.
- If the authors answer NA or No, they should explain why their work has no societal impact or why the paper does not address societal impact.
- Examples of negative societal impacts include potential malicious or unintended uses (e.g., disinformation, generating fake profiles, surveillance), fairness considerations (e.g., deployment of technologies that could make decisions that unfairly impact specific groups), privacy considerations, and security considerations.
- The conference expects that many papers will be foundational research and not tied to particular applications, let alone deployments. However, if there is a direct path to any negative applications, the authors should point it out. For example, it is legitimate to point out that an improvement in the quality of generative models could be used to generate deepfakes for disinformation. On the other hand, it is not needed to point out that a generic algorithm for optimizing neural networks could enable people to train models that generate Deepfakes faster.
- The authors should consider possible harms that could arise when the technology is being used as intended and functioning correctly, harms that could arise when the technology is being used as intended but gives incorrect results, and harms following from (intentional or unintentional) misuse of the technology.
- If there are negative societal impacts, the authors could also discuss possible mitigation strategies (e.g., gated release of models, providing defenses in addition to attacks, mechanisms for monitoring misuse, mechanisms to monitor how a system learns from feedback over time, improving the efficiency and accessibility of ML).

11. **Safeguards**

Question: Does the paper describe safeguards that have been put in place for responsible release of data or models that have a high risk for misuse (e.g., pretrained language models, image generators, or scraped datasets)?

Answer: [NA]

Justification: The paper poses no such risks.

Guidelines:

- The answer NA means that the paper poses no such risks.
- Released models that have a high risk for misuse or dual-use should be released with necessary safeguards to allow for controlled use of the model, for example by requiring that users adhere to usage guidelines or restrictions to access the model or implementing safety filters.
- Datasets that have been scraped from the Internet could pose safety risks. The authors should describe how they avoided releasing unsafe images.
- We recognize that providing effective safeguards is challenging, and many papers do not require this, but we encourage authors to take this into account and make a best faith effort.

12. **Licenses for existing assets**

Question: Are the creators or original owners of assets (e.g., code, data, models), used in the paper, properly credited and are the license and terms of use explicitly mentioned and properly respected?

Answer: [Yes]

Justification: All the assets used in the paper are properly cited.

Guidelines:

- The answer NA means that the paper does not use existing assets.
- The authors should cite the original paper that produced the code package or dataset.
- The authors should state which version of the asset is used and, if possible, include a URL.

- The name of the license (e.g., CC-BY 4.0) should be included for each asset.
- For scraped data from a particular source (e.g., website), the copyright and terms of service of that source should be provided.
- If assets are released, the license, copyright information, and terms of use in the package should be provided. For popular datasets, `paperswithcode.com/datasets` has curated licenses for some datasets. Their licensing guide can help determine the license of a dataset.
- For existing datasets that are re-packaged, both the original license and the license of the derived asset (if it has changed) should be provided.
- If this information is not available online, the authors are encouraged to reach out to the asset's creators.

13. **New assets**

    Question: Are new assets introduced in the paper well documented and is the documentation provided alongside the assets?

    Answer: [Yes]

    Justification: The new assets provided in the paper are well documented, and the documentation is provided alongside the assets.

    Guidelines:

    - The answer NA means that the paper does not release new assets.
    - Researchers should communicate the details of the dataset/code/model as part of their submissions via structured templates. This includes details about training, license, limitations, etc.
    - The paper should discuss whether and how consent was obtained from people whose asset is used.
    - At submission time, remember to anonymize your assets (if applicable). You can either create an anonymized URL or include an anonymized zip file.

14. **Crowdsourcing and research with human subjects**

    Question: For crowdsourcing experiments and research with human subjects, does the paper include the full text of instructions given to participants and screenshots, if applicable, as well as details about compensation (if any)?

    Answer: [NA]

    Justification: The paper does not involve crowdsourcing nor research with human subjects.

    Guidelines:

    - The answer NA means that the paper does not involve crowdsourcing nor research with human subjects.
    - Including this information in the supplemental material is fine, but if the main contribution of the paper involves human subjects, then as much detail as possible should be included in the main paper.
    - According to the NeurIPS Code of Ethics, workers involved in data collection, curation, or other labor should be paid at least the minimum wage in the country of the data collector.

15. **Institutional review board (IRB) approvals or equivalent for research with human subjects**

    Question: Does the paper describe potential risks incurred by study participants, whether such risks were disclosed to the subjects, and whether Institutional Review Board (IRB) approvals (or an equivalent approval/review based on the requirements of your country or institution) were obtained?

    Answer: [NA]

    Justification: The paper does not involve crowdsourcing nor research with human subjects.

    Guidelines:

    - The answer NA means that the paper does not involve crowdsourcing nor research with human subjects.

- Depending on the country in which research is conducted, IRB approval (or equivalent) may be required for any human subjects research. If you obtained IRB approval, you should clearly state this in the paper.
- We recognize that the procedures for this may vary significantly between institutions and locations, and we expect authors to adhere to the NeurIPS Code of Ethics and the guidelines for their institution.
- For initial submissions, do not include any information that would break anonymity (if applicable), such as the institution conducting the review.

16. **Declaration of LLM usage**

    Question: Does the paper describe the usage of LLMs if it is an important, original, or non-standard component of the core methods in this research? Note that if the LLM is used only for writing, editing, or formatting purposes and does not impact the core methodology, scientific rigorousness, or originality of the research, declaration is not required.

    Answer: [NA]

    Justification: The core method development in this research does not involve LLMs as any important, original, or non-standard components.

    Guidelines:

    - The answer NA means that the core method development in this research does not involve LLMs as any important, original, or non-standard components.
    - Please refer to our LLM policy (`https://neurips.cc/Conferences/2025/LLM`) for what should or should not be described.